THE UNIVERSITY OF CHICAGO

COARSE GRAINED MODELING OF SEMIFLEXIBLE AND ANISOTROPIC MATERIALS

A DISSERTATION SUBMITTED TO
THE FACULTY OF THE PRITZKER SCHOOL OF MOLECULAR ENGINEERING
IN CANDIDACY FOR THE DEGREE OF
DOCTOR OF PHILOSOPHY

BY
ALEC STEVEN BOWEN

CHICAGO, ILLINOIS
AUGUST 2019

TABLE OF CONTENTS

LIST OF FIGURES v

LIST OF TABLES x

ACKNOWLEDGMENTS xi

ABSTRACT xii

1 INTRODUCTION 1

2 STRUCTURAL CORRELATIONS AND PERCOLATION IN TWISTED PERYLENE DIIMIDES USING A SIMPLE ANISOTROPIC COARSE-GRAINED MODEL 5
- 2.1 Abstract 5
- 2.2 Introduction 5
- 2.3 Model and Methods 8
  - 2.3.1 Bonded Potentials 9
  - 2.3.2 Non-Bonded Potential 10
  - 2.3.3 Monte Carlo and Molecular Dynamics 12
  - 2.3.4 Determination of Coarse-Grained Simulation Parameters 13
  - 2.3.5 Coarse-Grained Analysis of π-Stacking Correlations 14
- 2.4 Results 16
  - 2.4.1 Simple Conjugated Rings 16
  - 2.4.2 Perylene Diimide Derivatives 18
  - 2.4.3 Morphologies of PDI Derivatives 19
  - 2.4.4 π-Stacking and Percolation Analysis of PDI Derivatives 23
- 2.5 Discussion 25
- 2.6 Conclusion 28
- 2.7 Appendix 29
  - 2.7.1 Fits to Gay-Berne and S-Function Expansion Potentials 29
  - 2.7.2 Comparison of AA and CG RDF 29
  - 2.7.3 S-Function Expansion 31
  - 2.7.4 Dihedral Angles 34
  - 2.7.5 S-Function Force Calculations 36
  - 2.7.6 Dihedral Force and Torque Calculations 38
  - 2.7.7 Benzene Parameters 40
  - 2.7.8 Ethylbenzene Parameters 41
  - 2.7.9 PDI-based Molecule Parameters 42

3 CLUSTER FORMATION AND ALIGNMENT IN LIQUID CRYSTALLINE POLYMER BRUSHES 47
- 3.1 Abstract 47
- 3.2 Introduction 47
- 3.3 Model and Methods 51

3.3.1 Nematic Semiflexible Polymer Model . . . 51
3.3.2 Order Parameter Correlation Function Calculations . . . 53
3.4 Results . . . 54
3.4.1 Bulk Polymer - Height Dependence on Chain Length and Nematic Interaction Strength . . . 54
3.4.2 Polymer Brush - Grafting Density and Nematic Interactions . . . 55
3.4.3 Polymer Brush - Correlation Lengths and Domain Formation . . . 60
3.5 Conclusion . . . 67

4 POLYMERS GRAFTED ONTO CELLULOSE NANOCRYSTALS . . . 68
4.1 Abstract . . . 68
4.2 Introduction . . . 68
4.3 Model and Methods . . . 71
4.3.1 Thermodynamic Integration . . . 73
4.3.2 Coarse-Grained Nanocrystal Suspension Model . . . 74
4.4 Results . . . 75
4.4.1 Solvent Effects . . . 75
4.4.2 Single CNC Systems . . . 76
4.4.3 Distance Dependence - Block Copolymer Brush . . . 83
4.4.4 Distance Dependence - Mixed Brush . . . 85
4.4.5 Orientation Dependence . . . 88
4.4.6 Volume Effects at Contact . . . 95
4.4.7 Large-Scale Nanocrystal Suspension Simulations . . . 96
4.5 Conclusion . . . 102
4.6 Appendix . . . 103
4.6.1 Solvent Parameters . . . 103
4.6.2 Nanocrystal Suspension Model Parameters . . . 103

5 SELF-ASSEMBLY IN BOTTLEBRUSH POLYMERS . . . 105
5.1 Abstract . . . 105
5.2 Introduction . . . 105
5.3 Model and Methods . . . 107
5.3.1 Model Description . . . 107
5.3.2 Structure Factor Calculations . . . 110
5.4 Results . . . 111
5.4.1 Side-Chain Extension and Semiflexibility . . . 111
5.4.2 Microphase Separation in Bottlebrush Polymers . . . 116
5.5 Conclusion . . . 126

6 CONCLUSIONS . . . 128

REFERENCES . . . 130

LIST OF FIGURES

2.1 Diagrams of the coarse-graining procedure for two of the PDI-based molecules in this study. Rigid regions of the atomistic model are replaced by coarse-grained anisotropic disks (green disks), while more isotropic regions, such as alkyl side chains, are represented as coarse-grained beads (red spheres). In addition to these two objects, non-interacting rigid attachment sites (black spheres) are used to bond objects to the coarse-grained disks at locations other than their center of mass. Note that only methyl sidechains are shown in the diagram, while octyl sidechains were used in simulations. 9

2.2 Comparison between RDFs for coarse-grained and atomistic benzene and ethylbenzene at 250 K, 300 K, and 350 K. All coarse-grained simulations use parameters fitted to 300 K atomistic simulations. 17

2.3 Global nematic order parameter comparison between different PDI-based molecules. Order parameter analysis utilizes the PDI disk orientational vector **f**. 20

2.4 Intermolecular RDF for all PDI-based molecules. **a)** shows RDFs for planar molecules, while **b)** shows RDFs for the non-planar molecules. Linear molecules show sharper first peaks than propeller-like molecules, a result of the stronger excluded volume effects in propeller-like molecules. 22

2.5 Degree of connectivity (ϕ) as a function of connectivity threshold value (ζ) for all simulated molecular structures. Planar molecules show a rapid drop in ϕ compared to non-planar molecules, indicating that their morphologies are not as percolative as those of the non-planar molecules. 23

2.6 Visualized morphology networks with each color representing an independent unconnected subgraph for $\zeta = 0.075$. The morphologies are **a)** 4PDI, **b)** hPDI, **c)** Ph2b, **d)** TPH-30, **e)** TPH-90, and **f)** Ph2a. Side chains are not shown for clarity. All images shown here have unwrapped periodic boundary conditions. Note that planar molecules cluster into separate groups, while non-planar molecules form three-dimensional percolating networks. Additionally, when non-planar molecules fracture, only a few molecules break off and form unconnected subgraphs, while the unconnected subgraphs in planar molecules are larger. 26

2.7 Comparison of benzene potential energy fits using the Gay-Berne model and the S-function expansion. Three representative orientations are shown. In addition to the displayed orientations, randomly selected orientations were also used in the fitting procedure. 30

2.8 PDI potential energy fits using the S-function expansion for three representative orientations. Note that in addition to the displayed orientations, 100 other randomly selected orientations were also fit. Fitting was biased using the Boltzmann factor so that configurations with the deepest minima were fit more accurately. . 30

2.9 Comparison of all-atom (**a**) and coarse-grained morphologies (**b**) for perylene diimide. Conjugated blocks are colored yellow, while alkyl side chains are red. Coarse grained simulations were initialized by mapping from the atomistic configuration, and were then allowed to relax. 31

2.10 Comparison of all-atom and coarse-grained radial distribution functions (**a**) and nematic order parameters (**b**) for perylene diimide. Radial distribution functions were calculated between the center of mass of each molecule. 32
2.11 Dihedral angles can be defined within the model between **a)** four beads, **b)** two beads and a disk, or **c)** two disks. When a disk is present, the normal vector **f** is used to define one of the vectors necessary for specifying the two planes. 35
2.12 Schematic for coarse-grained ethylbenzene 41
2.13 Schematic for coarse-grained hPDI and 4PDI. Note that only a single methyl group is depicted in the schematic, while octyl side chains were used in simulations. 43
2.14 Schematic for coarse-grained TPH. The central blue disk is used only for bonded interactions and maintaining dihedral angles. It does not interact through the S-function potential. Ph2a and Ph2b are almost identical to this structure. The only difference is that one of the PDI components is removed (Ph2b additionally has a 180 degree angle between the PDI components as opposed to 120 degrees). Note that only a single methyl group is depicted in the schematic, while octyl side chains were used in simulations. 43

3.1 Schematic for the semiflexible polymer brushes examined in this work. The orientation of each discrete unit of the polymer is indicated by the elongated axis of the ellipse. The parameters studied in this work are the following: l_p is the persistence length of the polymer brush (4 discrete units in this work). Δ is the length of a single discrete polymer unit. L is the length of a fully extended polymer. h is the average height of the brush. σ is the grafting density of the brush. All parameters in this work describing length are in units of l_p. 50
3.2 Plot of nematic order parameter (S) as a function of Maier-Saupe parameter (μ) for different polymer lengths (L). With the exception of $L = 20$, the polymer undergoes a first order isotropic-to-nematic transition at a finite value of μ. The necessary value of μ for this transition to take place increases with L, which reflects the increased conformational entropy which can counteract μ. 54
3.3 Brush height (h) dependence on grafting density (σ). **a)** shows the dependence for a system with $\kappa = 20.0$ and $\mu = 0.0$ while **b)** shows the dependence for a system with a nematic brush with $\kappa = 20.0$ and $\mu = 20.0$ and **c)** shows the dependence for a system with a nematic solvent in addition to the brush. Dotted lines in **a)** show the expected scaling behavior for an ideal flexible chain. 56
3.4 Side view images of the semiflexible brush under three separate conditions. **a)** has only excluded volume interactions, **b)** includes nematic brush interactions, and **c)** includes both nematic brush and nematic solvent interactions. The solvent is not shown in these images for clarity. 59
3.5 Top-down images of the brush morphology at different grafting densities, σ. Each brush polymer has length $L = 4\ l_p$ with $\kappa = 20.0$ and $\mu = 20.0$. Grafting densities are **a)** 1, **b)** 3, **c)** 5, **d)** 8, and **e)** 10 l_p^{-2}. 61
3.6 Top-down and side-view images of brush morphology at different polymer lengths (L): **a)** $L = 2.0$, **b)** $L = 8.0$, **c)** $L = 16.0\ l_p$, all at $\sigma = 8.0\ l_p^{-2}$. As the polymer length increases, the behavior of the brush changes from locally aligned clusters, to a fully aligned brush, to an isotropic brush. 63

3.7 Plots of the two-dimensional alignment correlation length (λ) as a function of polymer length (L) and grafting density (σ). At low σ, the polymer forms independent clusters of locally aligned polymer strands, which is signified by the finite values of λ. At higher grafting densities, λ increases rapidly beyond the size of the simulation box for some ranges of L, indicating the sudden transition to a fully aligned phase. As the grafting density is increased further, this range of fully aligned polymer is expanded. At all grafting densities shown here, λ drops rapidly to zero at high enough L, indicating a transition to the isotropic phase due to increased chain conformation entropy. 65
3.8 An AFM-style image of the topography of the nematically collapsed brush. **a)** The explicit chain morphology of the brush. Depending on how the chains are oriented, the brush may have a diversity of heights across the substrate. **b)** Heat map depicting brush height. **c)** Height as a function of y-coordinate position from different line slices. The line colors match the lines drawn on **a)**. 66

4.1 Comparison of the two nanorod styles examined in this work. **a)** Nanorod with diameter of approximately 30 nm and grafting density of something chains per nm^2. **b)** Nanorod of diameter of approximately 5 nm and grafting density of 0.3 chains per nm^2. Note that while the shapes and sizes of the nanorods differ, the chains themselves are the same size. Block copolymer chains shown here are under solvent BO. 75
4.2 Side and end views of block copolymer brush morphologies under the different solvent conditions. 77
4.3 Side and end views of block copolymer brush morphologies under the different solvent conditions for the narrow cellulose nanocrystal. 79
4.4 Side and end views of mixed brush morphologies under the different solvent conditions. 81
4.5 Side and end views of block copolymer brush morphologies under the different solvent conditions for the narrow cellulose nanocrystal. 82
4.6 Pair potentials of block copolymer brushes under various solvent conditions along with corresponding side views of cellulose nanocrystal pairs. Interactions among polymers on the different nanocrystals dictates the shape of the free energy curve. The free energy curve shapes can be divided into roughly three types: purely repulsive (A), attractive at intermediate ranges and repulsive at short ranges (BO,CO,D), and repulsive at intermediate distances and attractive at short ranges (BI,CI). 84
4.7 Pair potentials of mixed brushes under various solvent conditions along with corresponding side views of cellulose nanocrystal pairs. While solvents A and D behave similarly to their block copolymer brush counterparts, the greater extension of the swollen block in solvents B and C on the mixed brush causes the attractive regime to be weaker relative to the block copolymer brush. 86

4.8 Free energy curves for the thinner (5 nm diameter) nanorod system for both **a)** block copolymer brush and **b)** mixed brush. Even though it contains a different nanorod radius and grafting density, this system shows similar qualitative free energy behavior to the wider nanorod free energy curves shown in Figures 4.2 and 4.4. 89
4.9 Free energies as a function of rotation angle for the different solvent conditions. **a)** displays free energies for the block copolymer brush while **b)** shows them for the mixed brush. 90
4.10 Free energy curves for the thinner (5 nm diameter) nanorod system for both **a)** block copolymer brush and **b)** mixed brush. Even though it contains a different nanorod radius and grafting density, this system shows similar qualitative free energy behavior to the wider nanorod free energy curves shown in Figures 4.9a and 4.9b 92
4.11 Free energies as a function of rotation angle at different cellulose nanocrystal separation distances for block copoymer brushes. **a)** displays free energies under solvent BO, **b)** is under solvent CO, and **c)** is under solvent D. 94
4.12 Plots of **a)** the volume occupied by the swollen component of the polymer and **b)** the number polymer components in contact with polymers of the adjacent cellulose nanocrystal as a function of the separation distance between cellulose nanocrystals. Both plots follow the same trends as the volume appears to decrease immediately as soon as the contacts between the cellulose nanocrystals begin to increase. 97
4.13 Morphologies of cellulose nanocrystal suspensions. Red denotes nanocrystals with a tendency to align parallel to one another. Blue denotes nanocrystals that are purely repulsive, and do not have any innate tendency to condense. Green denotes nanocrystals with a tendency to form a crossed "X-shaped" configuration. **a**, **c**, and **e** were cooled in a box of constant volume, allowing void regions to form. **b**, **d**, and **f** were cooled in a box of constant pressure, providing a configuration that locally minimizes the energy. 99
4.14 Clustering analysis of the aligning and repulsive cellulose nanocrystal suspensions. **a)** displays the bare morphology before clustering, while **b)** color-codes each nanocrystal by its corresponding cluster. **c)** provides a distribution showing the likelihood of a cellulose nanocrystal belonging to a cluster of a given size. In general, the aligning cellulose nanocrystals tend to form larger clusters with a distribution that is more spread out. In comparison, the repulsive cellulose nanocrystals are more concentrated toward smaller cluster sizes. These distributions reflect the average number of clusters for each type: 98 for the aligning and 184 for the repulsive. 101

5.1 Schematic for the bottlebrush polymers studied in this work. Backbone beads are depicted in black, while side chain beads are depicted in red. The parameters examined in this study are the following: N_{sc} is the number of beads making up a single side chain. N_{bb} is the number of beads making up the backbone. R_e is the root-mean-square end to end distance of the side chain. L is the root-mean-square end to end distance of the backbone. B is the distance between two adjacent backbone beads. All distances reported in this work are in units of $R_{e,0}$, the root-mean-square end to end distance of an ideal unperturbed side chain polymer. 108
5.2 Plots of various bottlebrush polymer properties as a function of polymer density: **a)** side chain root mean square end-to-end distance, **b)** backbone long length scale persistence length, **c)** magnitude of long length scale persistence length, **d)** backbone root mean square end-to-end distance. The polymers range from highly rigid and extended at low density, to heavily screened at high density. 113
5.3 Plots of various quantities as a function of backbone monomer spacing, $B/R_{e,0}$: **a)** side chain root mean square end-to-end distance, **b)** backbone long length scale persistence length, **c)** magnitude of long length scale persistence length. . . 115
5.4 Image of a diblock bottlebrush polymer. Green beads represent the backbone monomers of the polymer, while red and blue beads are side chain monomers of monomers type A and B, respectively. 116
5.5 Image of a Janus bottlebrush polymer. Green beads represent the backbone monomers of the polymer, while red and blue beads are side chain monomers of monomers type A and B, respectively. 117
5.6 Plots of calculated structure factors for a diblock bottlebrush polymer at varying N_{bb} and B. Unless being varied, parameters for all plots shown here were held constant at $\chi N_{sc} = 6.0$, $N_{bb} = 30$, $\rho_0/N_{sc} = 10.0$, and $B/R_{e,0} = 0.16$. 119
5.7 Plots of calculated structure factors for a diblock bottlebrush polymer. Unless being varied, parameters for all plots shown here were held constant at $\chi N_{sc} = 6.0$, $N_{bb} = 30$, $\rho_0/N_{sc} = 10.0$, and $B/R_{e,0} = 0.16$. 120
5.8 Plots of calculated structure factors for a Janus bottlebrush polymer at varying N_{bb} and B. Unless being varied, parameters for all plots shown here were held constant at $\chi N_{sc} = 30.0$, $N_{bb} = 30$, $\rho_0/N_{sc} = 10.0$, and $B/R_{e,0} = 0.16$. 122
5.9 Plots of calculated structure factors for a Janus bottlebrush polymer. Unless being varied, parameters for all plots shown here were held constant at $\chi N_{sc} = 30.0$, $N_{bb} = 30$, $\rho_0/N_{sc} = 10.0$, and $B/R_{e,0} = 0.16$. 124
5.10 Plots of χN_{sc} at the order-disorder transition (ODT) as a function of several parameters for diblock and Janus bottlebrush polymers. **a)** is the diblock bottlebrush with varying backbone length. **b)** is the diblock bottlebrush with varying backbone monomer spacing. **c)** is the Janus bottlebrush with varying backbone length. **d)** is the Janus bottlebrush with varying backbone monomer spacing. . . 125

LIST OF TABLES

2.1 PDI-based coarse-grained molecules used in this study 13
2.2 Parameters for Coarse-Grained Benzene 40
2.3 Parameters for Coarse-Grained Ethylbenzene 41
2.4 Ethylbenzene Bonds 42
2.5 Ethylbenzene Angles 42
2.6 Ethylbenzene Dihedrals 44
2.7 Ethylbenzene Rigid Attachments 44
2.8 S-Function Parameters for Coarse-Grained PDI-based Molecules 44
2.9 hPDI and 4PDI Bonds (refer to Figure 2.13 for numerical labels) 44
2.10 hPDI and 4PDI Angles (refer to Figure 2.13 for numerical labels) 45
2.11 hPDI and 4PDI Dihedrals (refer to Figure 2.13 for numerical labels) 45
2.12 hPDI and 4PDI Rigid Attachments (refer to Figure 2.13 for numerical labels) . 45
2.13 TPH, Ph2a, and Ph2b Bonds (refer to Figure 2.14 for numerical labels) 45
2.14 TPH, Ph2a, and Ph2b Angles (refer to Figure 2.14 for numerical labels) 45
2.15 TPH, Ph2a, and Ph2b Dihedrals (refer to Figure 2.14 for numerical labels) . . . 46
2.16 TPH, Ph2a, and Ph2b Rigid Attachments (refer to Figure 2.14 for numerical labels) 46

4.1 Parameters for the virial model equation of state 103

ACKNOWLEDGMENTS

I would like to thank my advisor, Juan de Pablo, for his guidance during my graduate studies. I would also like to thank the following people who have I have been extremely fortunate to have had the privilege of working with: Lucas Antony, Nick Jackson, Grant Garner, Daman Khaira, Josh Moller, Viviana Palacio-Betancur, Mike Webb, Josh Lequieu, Emre Sevgen, Ashley Guo, Jiyuan Li, Weiwei Chu, Yamil Colón, Kyle Hoffmann, Brandon Peters, Phil Rauscher, Brian Keene, Tyler Roberts, Yongrui Su, Daniel Reid, and Moshe Dolejsi.

ABSTRACT

There is a vast set of industrially-relevant materials for which traditional molecular modeling techniques are not sufficient. Semiflexible, anisotropic, and stimuli-responsive materials all present distinct challenges toward the traditional techniques of developing theories and models with which to describe them. In this work, we develop specialized models to handle several different types of difficult materials, and then we use these newly developed models to perform a study on them. First we examine conjugated materials used in organic photovoltaics by creating an anisotropic coarse-grained model capable of describing the necessary twisted and fused geometries. A network analysis is performed to determine that molecules that are the most twisted can resist crystalline ordering and tend to work best for forming morphologies that are most fully connected and can easily transmit excitons. Second, we examine a semiflexible polymer brush that experiences nematic interactions by extending the theories that are commonly used to describe brushes with a wormlike chain backbone and Maier-Saupe pair interactions. We then examine the effect that grafting density and polymer length has on the nematic ordering that the brush experiences, and find that increasing grafting density tends to increase nematic correlation lengths, while increasing polymer length increases configurational entropy and decreases nematic ordering. Third, we examine polymers grafted onto cellulose nanocrystals under various solvent conditions by using a coarse-grained model with a three-body potential to implicitly model different solvent effects. We derive free energies as a function of distance and orientation between pairs of cellulose nanocrystals and use them to parameterize a coarser model and examine morphologies of cellulose nanocrystal suspensions for water percolation. Finally, we examine the self-assembly behavior of multi-component bottlebrush polymers in two architectures, diblock and Janus bottlebrushes, by extending a polymer model to include different architectures. We find that the two architectures have very different phase behavior, diblocks behave similar to linear polymers while Janus bottlebrushes rely more on the extent of side chain stretching to dictate their behavior.

CHAPTER 1

INTRODUCTION

Semiflexible, anisotropic, and stimuli-responsive molecules make up an enormous class of industrially-relevant materials. From the polymers found in organic solar cells to so-called "smart materials" that can reshape themselves upon encountering changing ambient conditions to micron-sized cellulose-based nanocrystals that can be used for water uptake, these materials have found many uses in both business-minded product development and purely scientific study. Although these types of materials have shown great promise for their potential impact on technology, they present challenges toward the traditional routes of developing theories and mathematical models to describe them. Such models are absolutely essential for improving our understanding of these materials and further developing our grasp on how best to use them. The most commonly used models, such as atomistic models for molecular dynamics, often perform very poorly when describing these types of systems. Typically, these models are designed for systems that are isotropic, at or near equilibrium, and of small size. The nature of anisotropic and semiflexible materials often resist full equilibration, tending more towards glassy states. Additionally, the large sizes of the molecules themselves can make full-scale atomistic simulations impractical outside of the largest and fastest supercomputers available. Instead, coarse-grained models must be designed specifically for each system of interest.

In this dissertation, we present several new models developed to study some of these challenging systems. The dissertation is organized into four main chapters. The common narrative throughout each chapter starts with a system that is difficult to describe using conventional modeling techniques. Then, a new model is described and developed to theoretically tackle the system. The model is then used to perform a study and new conclusions are drawn from the results of the simulations, thus concluding the narrative.

In Chapter 2, we examine a specific type of molecule for use in organic photovoltaics. The molecule, a conjugated-small molecule acceptor called perylene diimide, is highly anisotropic,

with incredible π-stacking tendencies. Furthermore, the molecule can be modified into several exciting architectures, including nanoribbons and propellor-like molecules with high-performing optical properties. We develop a new type of anisotropic coarse-grained model to handle this molecule and others like it, consisting of a pair potential called the S-function potential combined with torsional potentials defined between disks. These two features allow the model to capture the enormous anisotropic energetic wells that accompany perylene diimide as well as the twisted and fused architectures commonly found in molecules derived from it. Several of the molecular architectures are then examined more closely by running large scale simulations to reproduce their morphology in the bulk. Some simple network analysis is then carried out to examine their connectivity and determine which architectures work best for transmitting electricity throughout the material. It is shown that the more twisted the molecular architecture, the more fully connected the network becomes which enhances percolative electron transfer throughout.

In Chapter 3, we examine semiflexible polymer brushes that experience nematic interactions. These polymers belong to the class of so-called "smart materials" meaning that they can respond differently to changing conditions. Polymer brushes in general have been examined closely in numerous previous studies, and many theories have been developed to describe them. However, a large number of interesting polymers are both semiflexible and experience nematic interactions, specifically conjugated polymers that can conduct electricity and polymers with liquid crystalline monomers or moieties. These types of polymer brushes are less studied and hardly anything is known about their phase behavior. A coarse-grained model is developed that incorporates a discrete wormlike chain to describe the semiflexible backbone of the polymer, and a Maier-Saupe pair interaction to describe nematic effects. The polymer brush is examined under different grafting densities and polymer lengths. It is found that at low grafting densities, the brush tends to form small, locally aligned nematic clusters. As the grafting density is increased, the clusters get larger until they begin to overlap and a single continuous fully aligned brush is formed. In contrast, increasing the polymer

length causes the brush to lose its nematic characteristics due to increasing conformational entropy. At high enough polymer length, polymer brushes become isotropic regardless of the grafting density.

In Chapter 4, we examine block copolymer brushes and mixed brushes grafted onto cellulose nanocrystals. Cellulose nanocrystals are highly functionalizable biodegradable nanomaterials. One promising application for cellulose nanocrystals is grafting polymers onto them to enhance water uptake and water filtration. Similar to the previous chapter, the polymers grafted onto cellulose nanocrystals are stimuli-responsive. However, rather than the stimuli-responsive nature coming from nematic interactions between chains, the polymers instead react strongly to different solvent conditions. For example, one component of the polymer may collapse in a solvent, while the other swells. A model with a three-body potential is developed that can model such solvent effects implicitly. The model is then used to calculate pair potentials between polymer-grafted cellulose nanocrystals under several different solvent conditions. Thermodynamic intergration is used to calculate both the free energy as a function of distance and as a function of orientation. Next, these potentials are used to parameterize an even coarser model for the cellulose nanocrystals themselves. This model is then used to examine bulk cellulose nanocrystal morphology and some elementary clustering analysis is performed to quantify it.

In Chapter 5, we examine bottlebrush polymers and their self-assembly behavior. Bottlebrush polymers are a fascinating subclass of polymers, consisting of polymers with sidechains that are themselves polymeric. A lot of the most interesting properties of bottlebrush polymers comes from the repulsive effect that accompanies the crowded region near the polymer backbone. This steric repulsion creates side chains that are fairly extended, and a backbone that is fairly rigid, resulting in polymers that can resist entanglement. In addition, the added complexity of the bottlebrush architecture provides many opportunities for added complexity to phase separation. In this chapter, we examine two different types of two-component bottlebrush polymers and examine their phase separation behavior: diblock and Janus bot-

tlebrushes. Diblock bottlebrushes have two blocks along the backbone; the first block has polymer side chains of type A, while the other block has polymer side chains of type B. Janus bottlebrushes, in comparison, have two side chains for each backbone monomer, one of type A and one of type B. We build a model similar to the traditional polymeric field theory-type models, but we use Monte Carlo simulations, which allows us to examine important fluctuation effects. We find that diblock bottlebrushes have phase behavior similar to linear diblock polymers, longer chains appear to promote more phase separation. Janus bottlebrushes, however experience different phase behavior, where the backbone polymer length has little effect on the phase behavior.

Finally, in Chapter 6, we present a brief overview summarizing all of these findings and conclude. The general conclusion of this dissertation is that there is a host of materials of industrial interest for which traditional atomistic simulation models work poorly, and that new models must be derived instead to handle them.

CHAPTER 2
STRUCTURAL CORRELATIONS AND PERCOLATION IN TWISTED PERYLENE DIIMIDES USING A SIMPLE ANISOTROPIC COARSE-GRAINED MODEL

2.1 Abstract

Large, twisted, and fused conjugated molecular architectures have begun to appear more prominently in the organic semiconductor literature. From a modeling perspective, such structures present a challenge to conventional simulation techniques; atomistic resolutions are computationally inefficient, while traditional isotropic coarse-grained models do not capture the inherent anisotropies of the molecules. In this work, we develop a simple coarse-grained model that explicitly incorporates the anisotropy of these molecular architectures, thereby providing a route towards analyzing π-stacking, and thus qualitative electronic structure, at a computationally efficient coarse-grained resolution. Our simple coarse-grained model maintains relative orientations of conjugated rings, as well as inter-ring dihedrals, that are critical for understanding electronic and excitonic transport in bulk systems. We apply this model to understand structural correlations in several recently synthesized perylene diimide (PDI)-based organic semiconductors. Twisted and non-planar molecular architectures are found to promote amorphous morphologies while maintaining local π-stacking. A graph theoretical network analysis demonstrates that these twisted molecules are more likely to form percolating three-dimensional pathways for charge motion than strictly planar molecules, which show connectivity in only one dimension.

2.2 Introduction

A variety of molecular models exist for investigating the morphological and optoelectronic properties of conjugated systems. These models range from the fine-grained, in which ab

initio methods are used to simulate the electronic degrees of freedom, to the strongly coarse-grained, in which large superstructures representing clusters of molecules or fluid elements are used to access longer length scales. For conjugated materials, it is desirable to capture the main local structural features that influence optoelectronic properties, and to describe the mesoscale morphology that is ultimately responsible for the performance of a material. Conjugated systems are peculiar in that conventional coarse-grained models that were conceived for isotropic materials are often ill-suited to describe the strongly interacting, rigid, and anisotropic moieties, which can induce anisotropic packing and crystallization into distinct morphologies. Even as alkylic side chains are introduced into conjugated systems to promote solubility, the resultant morphologies exhibit pronounced anisotropic structural correlations.

Concrete examples of such systems are provided by a range of recently synthesized organic semiconductors consisting of large, fused, and twisted conjugated architectures.[156, 155, 154, 93, 19, 58, 146] Past coarse-grained models for conjugated systems have generally relied on spherical beads connected by springs[65, 91, 80, 61, 119, 36, 50, 119, 33, 1, 56] or on prolate ellipsoids[79, 77, 78, 135, 73] to represent clusters of monomers along the backbones of conjugated polymers. In doing so, some of the anisotropic interactions critical to describing many conjugated moieties are averaged out. Recent work has attempted to incorporate soft anisotropic interactions[46, 47] into models of conjugated polymers, but has so far been restricted to a single class of polymers and is not straightforwardly generalizable to different molecular architectures.

Importantly, in traditional coarse-grained models, extracting information about the optoelectronic functionality of a film of organic semiconductors necessitates a multi-scale approach. More specifically, the coarse-grained model must be back-mapped onto a fine-grained model which should then be allowed to relax before any optoelectronic characterization via quantum-chemical calculations are performed. Given the existence of a substantial literature on phenomenological electronic Hamiltonians that rely on simple configurational degrees of freedom,[150, 51, 63, 64, 13] the back-mapping to obtain optoelectronic information could in

principle be avoided, especially for qualitative electronic structure analysis. Significant information regarding electronic properties of a material could be directly obtained at coarse-grained resolution if the relevant configurational degrees of freedom were included and a suitable phenomenological Hamiltonian were parameterized.

Moreover, a coarse-grained model that focuses on retaining only nuclear degrees of freedom that are relevant to the valence electronic structure would potentially be desirable, particularly in the current era of multi-ring fused conjugated structures reported in the recent synthetic literature. The twisted helical nano-ribbons developed by Zhong, et al (Figure 2.1). [156, 155, 154] provide a good example of a molecular structure where there is no straightforward path to traditional coarse-graining, even though the entire structure is fused, twisted, and rigid, making an atomistic description inefficient for computational modeling work. A simple, generalizable coarse-grained model capable of accurately describing these unusual types of conjugated materials would find many uses and applications for development and characterization of organic electronic materials.

With those goals in mind, a coarse-grained model is presented here for organic semiconductors that is inspired by techniques more commonly used to investigate liquid crystalline systems.[97, 86, 84, 8, 11, 75, 41, 144, 22, 10, 5, 49, 81, 60, 107] Flat, rigid, and disk-like regions of molecules are represented by anisotropic "disks", with both orientational and translational degrees of freedom, whereas non-conjugated portions of the structures (e.g. alkyl chains) are described with simple isotropic beads. Interactions between disks are inherently anisotropic, thereby facilitating description of anisotropic conjugated systems, especially twisted and fused ones. Rather than averaging over all possible orientations of the rigid component, a disk-like description can often allow for a closer correspondence between the coarse-grained and atomistic models while reducing computational costs - for simple conjugated systems, it could even allow for a one-to-one correspondence. In addition to providing a more faithful description of anisotropic correlations between molecules, this level of representation allows for meaningful optoelectronic analysis using preserved dihedral an-

gles, π-stacking distances, and nearest-neighbor orientations. By avoiding back-mapping to atomistic models and quantum-chemical analysis, the proposed approach has the potential to further accelerate the ability to access configuration-dependent optoelectronic properties, which is a primary goal of organic semiconductor modeling.

The outline of the paper is as follows. Section I presents the coarse-grained model, strategies for coarse-graining, and methods used for ensemble simulations. Section II applies the model to elementary conjugated rings as a proof of concept for comparing structural features between coarse-grained and atomistic representations. The model is then applied to study a variety of fused, non-planar conjugated perylene diimide (PDI)-based systems that have been reported in the recent literature. A network analysis approach, similar to that of Savoie et al.,[118] is implemented on the coarse-grained configurations to assess the ability of the underlying charge transport networks, as represented by π-stacking correlations, of twisted conjugated structures to percolate disordered films of these materials. In Section III, we further suggest that for a number of optoelectronic applications, the optimal percolating molecular structure is twisted and conjugated, and link the conclusions derived from our coarse-grained model back to the chemistry of conjugated materials. Section IV presents our concluding remarks.

2.3 Model and Methods

The proposed model consists of combinations of coarse-grained "disks" and "beads" to describe unique chemical components. Each large conjugated region of a molecule is described by a single anisotropic disk. The disk may represent something that is truly disk-like, including the flat and rigid components that are found in organic small molecule acceptors, or the aromatic rings encountered along the backbones of conjugated polymers. Alternatively, the disk may represent spherical moieties, such as fullerenes.[143] More isotropically interacting regions of the molecular structure, such as those found along an alkylic side chain, are described by spherical coarse-grained beads.

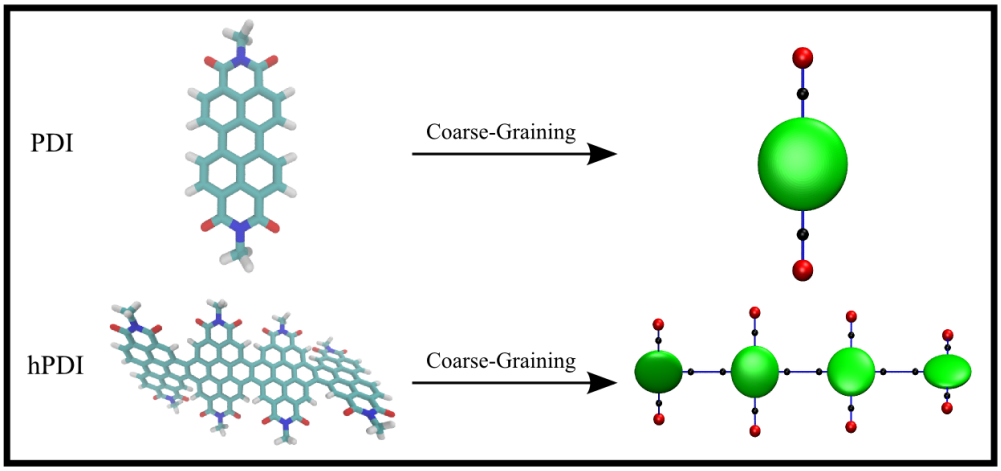

Figure 2.1: Diagrams of the coarse-graining procedure for two of the PDI-based molecules in this study. Rigid regions of the atomistic model are replaced by coarse-grained anisotropic disks (green disks), while more isotropic regions, such as alkyl side chains, are represented as coarse-grained beads (red spheres). In addition to these two objects, non-interacting rigid attachment sites (black spheres) are used to bond objects to the coarse-grained disks at locations other than their center of mass. Note that only methyl sidechains are shown in the diagram, while octyl sidechains were used in simulations.

The configuration of a system is described by a position vector, $\mathbf{r}$, and a momentum vector, $\mathbf{p}$. Coarse-grained disks are represented by a set of orthonormal unit vectors, $\mathbf{u}$, $\mathbf{f}$, and $\mathbf{v}$ that uniquely determine their orientation, as well as an angular momentum vector, $\mathbf{L}$. For planar molecules, $\mathbf{f}$ is defined as the vector orthogonal to the plane of the disk, and also acts as the uniaxial vector when evaluating the non-bonded energy. Here $\mathbf{u}$ is a vector within a plane that is orthogonal to $\mathbf{f}$; $\mathbf{v}$ is defined such that $\mathbf{v} = \mathbf{u} \times \mathbf{f}$. In total, each disk has 12 independent degrees of freedom (6 describing position and orientation, 6 describing momentum), while a bead only has 6 independent degrees of freedom.

2.3.1 Bonded Potentials

Bonded interaction energies are described using harmonic bonds, harmonic angles, and OPLS-style dihedrals.[69] Dihedral interactions can be defined between two adjacent disks using the $\mathbf{f}$ vectors in addition to the more common four-body interaction (see SI). The

bonded energy is given by

$$\begin{aligned} E_b &= \sum_{i\in\text{bonds}} \tfrac{k_{b,i}}{2}(d_i - d_0)^2 + \sum_{i\in\text{angles}} \tfrac{k_{a,i}}{2}(\theta_i - \theta_0)^2 \\ &+ \sum_{i\in\text{dihedrals}} \tfrac{1}{2}[k_{1,i}(1+\cos\phi_i) + k_{2,i}(1-\cos 2\phi_i) \\ &+ k_{3,i}(1+\cos 3\phi_i) + k_{4,i}(1-\cos 4\phi_i)] \end{aligned} \tag{2.1}$$

In addition to these bonded interactions, rigid bonds are also included from the center of mass of the coarse-grained disks to massless attachment sites. The locations of these attachment sites can be uniquely specified in terms of the **ufv** coordinate system, so that the attachment sites move and rotate with their corresponding disk. These attachment sites allow for harmonic bonds and angles for linking sites that are removed from the disk center of mass, which is necessary for specifying the location of side-chains on large conjugated systems.

2.3.2 Non-Bonded Potential

Non-bonded interactions between disks are described using a pairwise anisotropic potential consisting of an S-function expansion.[128] The potential takes as input the two vectors describing the orientation for each pair of disks, $\mathbf{f}_i$ and $\mathbf{f}_j$, and the vector describing the distance between their centers of mass: $\mathbf{r}_{ij} = \mathbf{r}_i - \mathbf{r}_j$. Since the interaction potential must be rotationally invariant, it depends only on the dot products of the three relative orientation vectors ($\mathbf{f}_i$,$\mathbf{f}_j$,$\mathbf{r}_{ij}$). The S-function expansion is a generalized Fourier series in these dot products, and can be tuned to fit arbitrary uniaxial anisotropy. Note that, in general, we find that the structures considered in this study are not described sufficiently well by a Gay-Berne potential (See SI); typically, they require a flatter disk-like shape than the Gay-Berne potential can represent. Additionally, the S-function expansion allows for T-shaped configurations to have deeper energy minima than edge-to-edge configurations, which is important for capturing the intermolecular interactions between many aromatic rings.[124] The

non-bonded potential used here is assumed to account for all Lennard-Jones and electrostatic interactions of the underlying atomistic model. This short-ranged electrostatic assumption is justified for PDI-based systems, as PDI is charge neutral and exhibits no dipole moment, meaning the lowest order electrostatic interactions between PDI are quadrupole-quadrupole, which will decay rapidly with distance (r) as (r^{-5}), and can be absorbed into the short-range S-function potential. For systems where long-range interactions are important, such as molecules with permanent charge or dipole moments, the model must be extended to incorporate a potential of the necessary form. Augmentation with additional potentials is straightforward, as charge and dipole potentials can be included on top of the S-function potential, and fast electrostatic solvers can be directly applied. Note that in such a case the short-range electrostatic interactions should not be averaged into the S-function expansion, and should be treated in the appropriate Ewald-like fashion.

The intermolecular potential is of the form:

$$E_{nb} = \sum_{i=1}^{n} \sum_{i<j}^{n} U(\mathbf{f}_i, \mathbf{f}_j, \mathbf{r}_{ij}) \tag{2.2}$$

For two disks:

$$U(\mathbf{f}_i, \mathbf{f}_j, \mathbf{r}_{ij}) = 4\epsilon(\mathbf{f}_i, \mathbf{f}_j, \mathbf{r}_{ij}) \left[a^{12} - a^{6}\right] \tag{2.3}$$

$$a = \frac{\sigma_0}{|\mathbf{r}_{ij}| - \sigma(\mathbf{f}_i, \mathbf{f}_j, \mathbf{r}_{ij}) + \sigma_0} \tag{2.4}$$

Interactions between coarse-grained beads, such as the methyl groups in an alkane, are modeled using an isotropic Lennard-Jones interaction. Interactions between beads and disks were described using a modification of the S-function expansion, (see SI) where only the terms of the expansion that involve anisotropy of one disk are included. Specific definitions for each term in Eq. 2.2-2.4, as well as the calculation of forces, are provided in the Appendix.

Figure 2.1 displays a detailed schematic for how these coarse-grained anisotropic molecules are represented.

2.3.3 Monte Carlo and Molecular Dynamics

Metropolis Monte Carlo simulations were performed in the NVT ensemble. Disk/bead displacement, disk rotation, full molecule translation, and full molecule rotation moves were implemented, with different moves being randomly selected with probabilities (0.3,0.3,0.2,0.2), respectively. Attachment sites (as described in the Bonded Potentials section) are not treated as independent components and are not given individual Monte Carlo moves. Instead, they are updated simultaneously with their corresponding parent disk to reflect the rigid nature of the bond.

Conjugated systems often exhibit high glass transition temperatures, and tend to become kinetically trapped (non-ergodic). For example, PDI has an energetic minimum of approximately 80 kJ/mol in the π-stacked configuration. While a variety of "advanced" Monte Carlo techniques are available to address some of these issues,[142, 123] molecular dynamics was used to determine time-dependent structural and dynamical properties in the glassy state. Force and torque calculations for the S-function expansion are described in the Appendix. In this work, the time evolution is performed using the symplectic and time-reversible integrator of Kamberaj et al.[70, 104] Molecular dynamics runs are initiated from high temperature configurations imported from Monte Carlo simulations, and annealed to 300 K over the course of 5 ns using periodic velocity rescaling. Once cooled, simulations are propagated under NVE dynamics, from which structural and network analysis is then performed over the course of 5 ns trajectories. The coarse-grained molecular dynamics model described has been fully implemented in LAMMPS, and is available upon request.

Table 2.1: PDI-based coarse-grained molecules used in this study

	Architecture	Group	Image
PDI	None	Planar	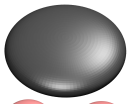
Ph2b[58]	Linear	Planar	
Ph2a[58]	2-Propeller (30 degrees)	Non-Planar	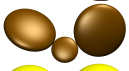
TPH-0	3-Propeller (0 degrees)	Planar	
TPH-30[93]	3-Propeller (30 degrees)	Non-Planar	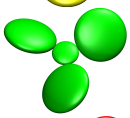
TPH-60	3-Propeller (60 degrees)	Non-Planar	
TPH-90	3-Propeller (90 degrees)	Non-Planar	
4PDI	Linear	Planar	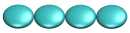
hPDI[156]	Linear	Non-Planar	

2.3.4 Determination of Coarse-Grained Simulation Parameters

The coarse-grained interaction parameters used here were adopted with reference to atomistic models by using an iterative potential-energy matching technique. The parameters defining the anisotropy as a function of relative orientation, $\epsilon(\mathbf{r}_{ij}, \mathbf{f}_i, \mathbf{f}_j)$ and $\sigma(\mathbf{r}_{ij}, \mathbf{f}_i, \mathbf{f}_j)$, were calculated by first fitting atomistic pair-wise potential energy curves as a function of distance at a set of known minimum-energy configurations, as well as 100 randomly selected orientations. These fitted curves provided values of σ and ϵ for each orientation. The S-function expansion in the anisotropic $\epsilon(\mathbf{r}_{ij}, \mathbf{f}_i, \mathbf{f}_j)$ and $\sigma(\mathbf{r}_{ij}, \mathbf{f}_i, \mathbf{f}_j)$ terms was then fit to these values using the sbplx optimization routine.[68, 115] Each orientation was weighted according to $\exp(-\beta\epsilon)$, so that orientations with the deepest energetic minima possessed the highest accuracy, and the higher energy configurations, which are less relevant in statistical averaging, were weighted less heavily. The goal for such fitting was to approximately retain

the appropriate well-depths and contact distances in different orientations within the coarse-grained model (see SI for fits to different molecules). For simple anisotropic molecules like benzene and ethylbenzene, these potential energy functions should be sufficient in the dilute limit, where many-body correlations can be neglected. In dense systems, these parameters may require some correction. For benzene and ethylbenzene simulations, σ_0 and ϵ_0 were fine-tuned by sweeping over a small range of perturbations around the original values, and selecting those that best fit the RDFs. For simulations of PDI-based molecules, we use combinations of the disk parameterized to produce the well-depths and excluded volume of a single PDI to generate the structures of Table 2.1, with no additional fine-tuning performed. Bonded potential parameters were selected to match the mean bond length, mean angle, and mean dihedral angle between different chemical components. Due to the stiffness and lack of flexibility that are characteristic of conjugated systems, many bond, angle, and dihedral parameters were chosen to render the molecules effectively rigid (see SI).

2.3.5 Coarse-Grained Analysis of π-Stacking Correlations

By construction, the coarse-grained model preserves the fundamentally important orientational anisotropies of the system; coarse-grained analysis of π-stacking correlations can therefore be applied without relying on back mapping to more detailed atomistic representations. As a proof-of-principle, a network analysis based on the methodology of Savoie et al.[118] was applied to determine the percolative nature of charge transport networks in the simulated morphologies. This analysis uses a weighted adjacency matrix, $\mathbf{w}$, to incorporate the electronic coupling of the valence orbitals between neighboring molecules. In our analysis, we use a geometrical definition of local π-stacking orientational correlations as a proxy for the electronic coupling. Element $\mathbf{w}_{ij}$ of the adjacency matrix represents the "connection strength" between disk components i and j. Disk components on the same molecule were defined as "always connected" and given a weight of 1.0 in the weighted adjacency matrix - this assumption reasonably treats all intramolecular electronic couplings as substantially

larger than intermolecular. Intermolecular connection strength was determined via:

$$\mathbf{w}_{ij} = \left(\mathbf{f}_i \cdot \hat{\mathbf{r}}_{ij}\right)^2 \left(\mathbf{f}_j \cdot \hat{\mathbf{r}}_{ij}\right)^2 \left(\mathbf{f}_i \cdot \mathbf{f}_j\right)^2 e^{-\alpha|\mathbf{r}_{ij}|} \tag{2.5}$$

where α is a constant (0.1 Å^{-1} in this study),[145] $\mathbf{f}$ refers to the uniaxial normal vector defining the orientation of a disk, $\mathbf{r}_{ij}$ is the vector defining the distance between molecules, and the hat denotes a unit vector. This form of the connection strength was chosen to capture the correct orientational dependence of π-stacking, as well as the correct distance dependence of the electronic coupling.[145] We note that this form for the graph weights has been used previously, and can quantitatively describe the orientationally dependent electronic couplings in ethene, as well as many of the qualitative changes in more complex organic semiconducting molecules[134, 9, 63].

For network analysis, $\mathbf{w}$ was used to decompose the weighted graph into unconnected subgraphs. A threshold connectivity criterion, ζ, was set, and for each disk pair, if the corresponding $\mathbf{w}_{ij}$ was greater than ζ, the two disks were considered connected. Otherwise, they were considered unconnected. From this connection graph, the degree of connectivity, ϕ, was calculated. The degree of connectivity provides a measure of how connected a network is, and was defined as the inverse of the number of unconnected subgraphs for a given threshold value of $\mathbf{w}$.[118] For example, if all "nodes" in the network are connected to all other nodes, then there is only one subgraph, and the degree of connectivity is unity. If four such subgraphs can be described amongst which all nodes are connected, but having no connections across subgraphs, then the degree of connectivity is 0.25. The dependence of ϕ on ζ was determined for different molecular architectures described in Table 2.1. Morphologies that exhibit the most percolative charge transport networks are those that remain fully connected ($\phi = 1$) at high threshold values and resist fracturing of the network. If a bulk morphology has a high degree of connectivity on the basis of electronic couplings, then it represents a necessary, but not sufficient, criterion for efficient performance. Note that other

factors such as energetic disorder also play a critical role in charge carrier transport.[7]

2.4 Results

2.4.1 Simple Conjugated Rings

As benzene is one of the simplest conjugated rings, liquid benzene was selected as a test of our model's ability to capture the most important features of an anisotropic conjugated system. While benzene may appear trivial, it is important to examine in detail for two reasons. First, it allows for the assessment of the flexibility of the S-function expansion, since the T-shaped configuration of benzene has a lower energy than the π-stacked configuration,[6] and has a closer contact distance than the Gay-Berne model will allow (see SI). Second, benzene is a common building block of many conjugated materials, and its accurate description is essential. Anisotropic S-function parameters were determined from the benzene OPLS-AA force field[69] by directly fitting potential energy surfaces between molecules using the nonlinear sbplx optimization routine.[68, 115] Scaling parameters for the S-function potential, σ_0 and ϵ_0, were then tuned to fit the RDF of the atomistic simulation at 300 K. Figure 2.2 displays the plots of the RDF, where quantitative agreement between atomistic and coarse-grained models is observed at 300 K, as well as 250 K and 350 K using the coarse-grained parameters derived at 300 K.

Ethylbenzene was selected as a second test system, as it is structurally similar to benzene, but allows for the incorporation of isotropic beads in conjunction with anisotropic disks in the coarse-grained representation. The ethylbenzene system was modeled as a disk to represent the aromatic ring, with two beads to represent the methyl groups. The disk parameters controlling anisotropy were taken to be the same as those of benzene. Parameters for the methyl groups were selected from the OPLS-UA force field, and the bond, angle, and dihedral parameters were determined through direct Boltzmann inversion at 300 K. All ethylbenzene parameters used here are provided in the Appendix. Ethylbenzene simulations

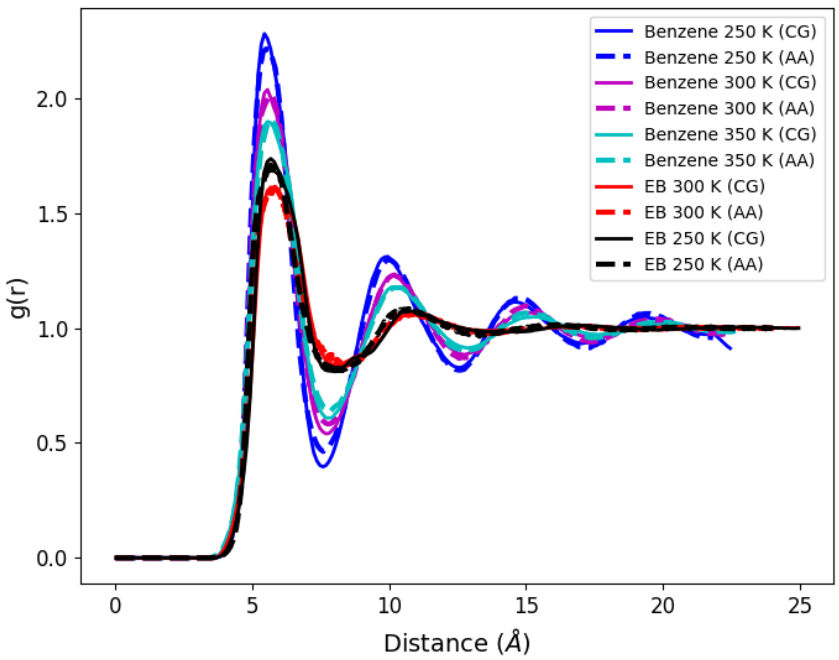

Figure 2.2: Comparison between RDFs for coarse-grained and atomistic benzene and ethylbenzene at 250 K, 300 K, and 350 K. All coarse-grained simulations use parameters fitted to 300 K atomistic simulations.

.

were run at 300 K and 250 K with identical parameters, and the resulting RDFs are presented in Figure 2.2. The model accurately describes the atomistic system over a wide range of temperatures and densities. The high accuracy of the coarse-grained model can be attributed to the simplicity of benzene and the phenyl group. The S-function potential can properly accommodate and account for nearly all orientation dependencies of the atomistic interaction potential due to benzene's near-uniaxiality. For larger, biaxial or non-symmetric conjugated moieties, this level of transferability cannot be expected.

2.4.2 Perylene Diimide Derivatives

Coarse-grained simulations were performed on a number of systems of PDI-based small molecule organic semiconductors from the organic photovoltaic (OPV) literature, including helical nanoribbons,[156, 155, 154, 125] three-bladed propellers,[93] and ring-fusion based molecules.[58] (Table 2.1) The majority of these structures are based on recent reports, but four hypothetical structures (4PDI, TPH-0, TPH-60, TPH-90) have also been included that represent slight perturbations of existing structures. Simulations were used to assess the impact of molecular structure on both the resulting morphology, as well as the percolative connectivity of the morphology for charge transport. In general, the most robust materials in the context of OPVs are those wherein the bulk material exhibits fully percolated charge transport pathways. Morphologies that are fully connected and do not contain a preferred conducting direction naturally work best to promote this desired behavior.[63, 64, 118, 136, 103] Simple, flat disk-like molecules, such as bare PDI, are expected to crystallize readily, a fact well-known experimentally.[85, 57] While these molecules are well-coupled electronically along "tubes" in the π-stacking direction,[118] the tubes are inherently one-dimensional. The more distorted "non-planar" structures are designed to disrupt crystallization and induce disorder in the bulk structure, all while maintaining a percolative network.

Coarse-grained interaction parameters between disks were chosen to retain the main qualitative features of PDI - specifically the relative orientational well-depths and positions. The

same fitting procedure as was used for benzene was used to capture the well-depths and shape parameters of PDI in different orientations. Unlike benzene, however, these systems tend to readily crystallize or form glassy states at ambient temperature due to the strength of the π-π interaction. For this reason, direct comparison of RDFs between atomistic and coarse-grained systems was not effective, as they largely depend on the precise structural details of whichever kinetically trapped state the system is in. Rather than focusing on reproducing quantitative structural features in this study, we are interested in learning how simple changes to molecular architecture can influence the robustness of percolative network formation in disordered morphologies. Specifically, molecules whose charge transport networks are robust to nanoscale disorder may be useful in a variety of organic semiconducting applications. In view of these facts, along with the deep enthalpic minima of the π-stacked configurations and highly rigid structures, we did not modify the S-function potential beyond the initial fitting to exactly match coarse-grained and atomistic RDFs.

Molecular configurations were prepared with 150 PDI disk components in a cubic simulation box with 50 Å sides and periodic boundary conditions. Each disk included an octyl side-chain attached at each N-imide position of the PDI (2 octyl chains/PDI), where the alkyl groups of the side-chains were represented as coarse-grained beads with OPLS-UA parameters. This density corresponds to $\sim$ 1.1 g/cm^3, which is that obtained by cooling an atomistic OPLS model for octyl-PDI from 600K to 300K at a cooling rate of 10K/ns. The total number of molecules for each molecular architecture of Table 2.1 was varied in order to maintain a constant density. For example, bare PDI had four times as many molecules in a simulation as hPDI, but was represented with the same number of disks and density. All results were averaged over five independent trajectories for each molecular structure.

2.4.3 Morphologies of PDI Derivatives

For convenience, the different molecular architectures of Table 1 can be divided into two groups, referred to as "planar" and "non-planar." Planar molecules have all conjugated

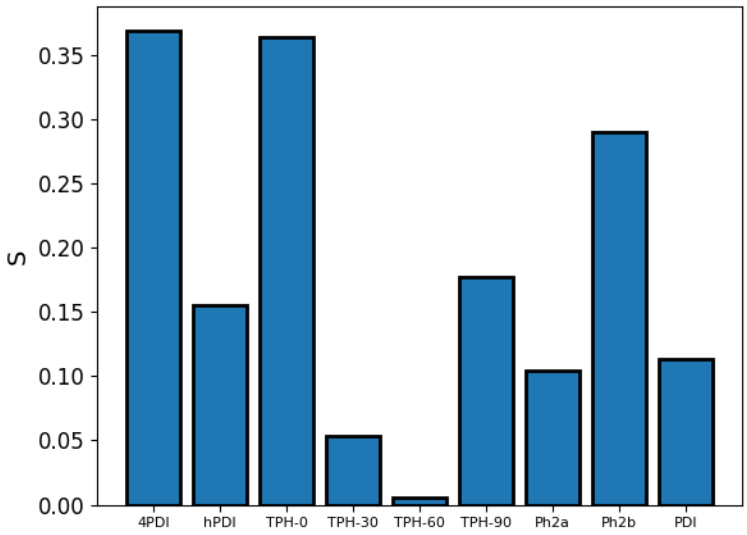

Figure 2.3: Global nematic order parameter comparison between different PDI-based molecules. Order parameter analysis utilizes the PDI disk orientational vector **f**.

.

regions located within the same plane: PDI, Ph2b, TPH-0, and 4PDI. We expect these molecules to exhibit a strongly preferential stacking direction, which could give rise to large crystalline regions throughout the film. Non-planar molecules are those with fixed torsions throughout : TPH (30, 60, and 90 degree variants), Ph2a, and hPDI.

Global nematic order parameters and radial distribution functions were computed for the morphologies of all structures displayed in Table 2.1, and are presented in Figure 2.3 and Figure 2.4, respectively. Nematic order parameter analysis used the **f** orientational vector of each PDI disk and was calculated as the largest eigenvalue of the Q-tensor:

$$\mathbf{Q} = \frac{1}{N}\sum_{i=1}^{N}\left(\frac{3}{2}\mathbf{f}_i\mathbf{f}_i^T - \frac{1}{2}\mathbf{I}\right) \tag{2.6}$$

From the nematic order parameter analysis, there is a clear preferential alignment for the large planar molecular structures within the bulk morphology, in particular 4PDI and Ph2b. These molecules, upon inspection of the morphologies, cluster readily into small groups. PDI displays a smaller value of the nematic order parameter than both 4PDI and Ph2b while simultaneously having a similar height of the first neighbor peak of the RDF. This suggests

that bare PDI tends to correlate strongly with its immediate neighboring molecules because of its smaller size, but independent clusters do not have persistent orientations over many molecular lengths, which lowers the value of the nematic order parameter. 4PDI, TPH-0, and Ph2b, having stronger neighboring interactions, exhibit larger orientational correlations with their longer-range neighbors.

Compared to the planar molecules, the non-planar molecules exhibit smaller values of the nematic order parameter, which is to be anticipated considering that their twisted architectures disrupt molecular alignment. Surprisingly, the RDFs for nearly all of the PDI-based molecules show similar features, including a peak at approximately 4.5 Å. However, the propeller-like molecules display a weaker first peak than the linear molecules, which corroborates their design as more disordered materials.

PDI components on the twisted propeller-like molecules are placed together in such a way that excluded volume effects frustrate π-π stacking, as exhibited by the TPH molecules in Figure 2.3. Rather than aligning directly on top of each other, individual PDI components are forced into a π stacking configuration that is slightly offset, which is revealed by a first peak in the RDF that is smaller than that found for the linear molecules. For TPH-30, the first peak of the RDF is noticeable at 4.5 Å, even though it is smaller than that of the linear molecules, which indicates that PDI components are still able to stack to some extent. The excluded volume effects are so strong in TPH-60 and TPH-90 that the first peak is changed entirely. In TPH-60, the system is nearly amorphous, so no first peak can be seen. Since TPH-90 has its side chains perpendicular to the rest of its body, the molecules align in a manner similar to gears in a cogwheel assembly. Excluded volume effects in TPH-90 push the first peak to a distance of 5.5 Å. Linear molecules do not have the same packing frustration effects as the TPH variants; hPDI, TPH-0, 4PDI, and Ph2b all show similar behavior at the first peak, indicating that PDI components on these linear molecules are allowed to overlap directly, and not forced into offset π stacking configurations.

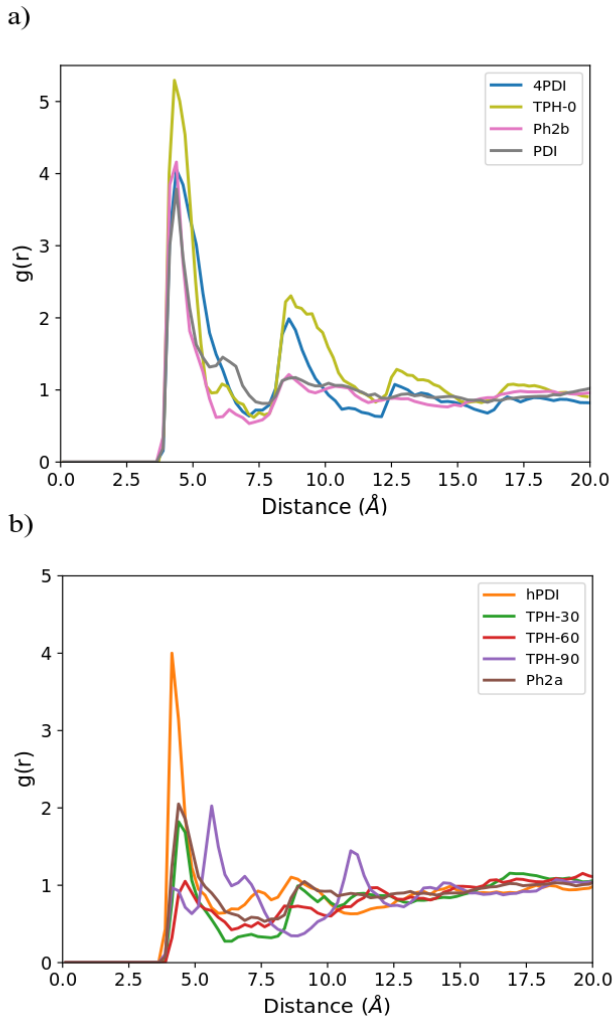

Figure 2.4: Intermolecular RDF for all PDI-based molecules. **a)** shows RDFs for planar molecules, while **b)** shows RDFs for the non-planar molecules. Linear molecules show sharper first peaks than propeller-like molecules, a result of the stronger excluded volume effects in propeller-like molecules.

.

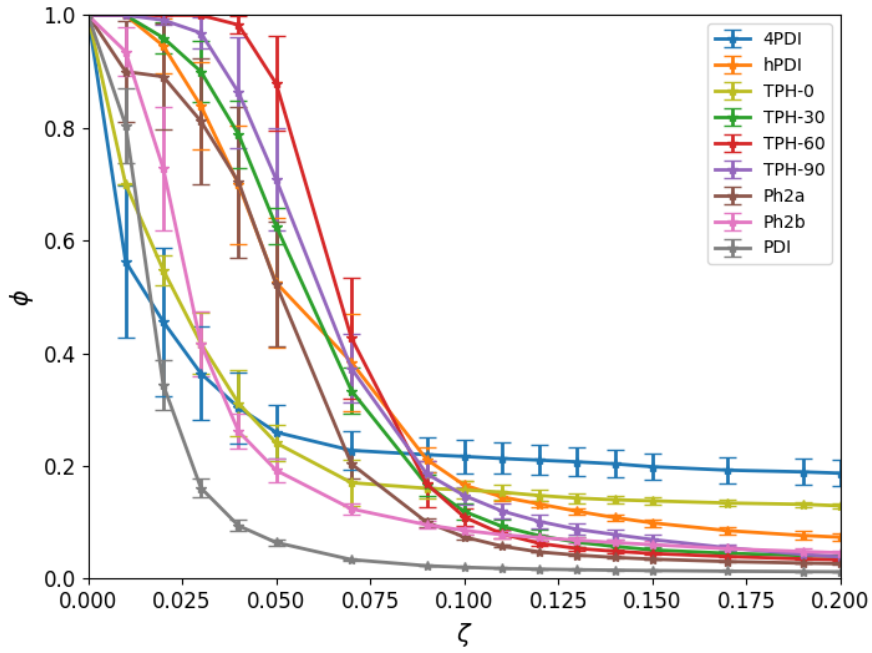

Figure 2.5: Degree of connectivity (ϕ) as a function of connectivity threshold value (ζ) for all simulated molecular structures. Planar molecules show a rapid drop in ϕ compared to non-planar molecules, indicating that their morphologies are not as percolative as those of the non-planar molecules.

.

2.4.4 π-Stacking and Percolation Analysis of PDI Derivatives

The network analysis procedure described in the Methods section was performed for all simulated molecular structures in Table 2.1. The results are shown in Figure 2.5. The performance of different molecular structures was examined by comparing the degree of connectivity, ϕ, as a function of threshold value, ζ. At low ζ, the network is fully connected, which is shown in the limit as $\zeta \to 0$. As ζ is increased, the morphology eventually fractures into unconnected subgraphs, represented by the drop in ϕ. Certain regions of the morphology may be weakly connected, and fracture immediately upon increasing ζ, while others may be strongly connected and will not fracture even for high ζ. Our main concern is to determine which architectures are most percolative, meaning those architectures that resist initial fracturing of the network and maintain a high degree of connectivity for as large a value of ζ as possible. These same molecules are the ones that would likely perform most

robustly in an OPV setting, where percolative connectivity is paramount. In nearly all cases, the molecules described as non-planar fracture at higher ζ than the planar molecules.

A representative example of this behavior can be appreciated by comparing planar 4PDI to non-planar hPDI, where the only difference between the two molecules is a thirty degree torsion between neighboring PDIs along the backbone of hPDI. As shown in Figure 2.5, 4PDI begins to fracture at a lower ζ than hPDI, and then fractures more rapidly as ζ is increased. Upon inspection of the morphology (Figure 2.6 a,b), this behavior can be explained through the observation that 4PDI tends to form crystalline clusters. Even though each cluster has strongly connected PDI components within it, the connections across separate clusters are weak. When ζ is increased, the network quickly breaks into these discrete clusters. In contrast, hPDI promotes an amorphous morphology. While individual PDI components still stack and remain highly correlated, as deduced from the RDF in Figure 2.4b, they do not form clusters as in 4PDI. Individual hPDI molecules are spaced out more evenly than 4PDI, and exhibit greater connections across molecules. Figures 2.6a and 2.6b show representative morphologies of 4PDI and hPDI at $\zeta = 0.075$ with each unconnected subgraph denoted by a different color. The individual clusters can be clearly seen in the case of 4PDI; hPDI, while not as tightly connected as 4PDI, maintains a more uniform morphology, which promotes greater connectivity throughout the entire film.

Similarly, propeller-like molecules are effective at forming percolative structures because of their non-planarity. The behavior of Ph2a compared to Ph2b is analogous to the behavior of hPDI compared to 4PDI. The non-planar structure of Ph2a promotes disorder within the film, allowing it to be more resistant to the initial network fracturing than Ph2b.

Interestingly, while all TPH variants exhibit a similar behavior in Figure 2.5, one can identify several differences in their underlying morphologies. TPH-30 and TPH-60 have similar behavior, and form three dimensional percolating networks, similar to hPDI and Ph2a. Since TPH-90 aligns in a gear-like manner, it has a greater tendency to form two-dimensional networks separated by alkyl side chain layers. An example of such a morphology

can be seen in Figure 2.6e where the bottom two layers are nearly separate. This behavior suggests that it is the low symmetry, twisted structures, such as in TPH-30, TPH-60, hPDI, and Ph2a that disrupt crystallization and are more adept at forming three-dimensional percolating networks.

These results correspond well to experimental characterizations of systems of Ph2a, Ph2b,[58] and hPDI[155] using GIWAXS. In those studies, the twisted materials, hPDI and Ph2a, were found to not have any preferred orientation relative to a substrate, and their orientation correlation with surrounding molecules was found to be low. Ph2b, however, was found to have a strongly preferred packing direction and be much more highly correlated with surrounding molecules. Both of these results are strongly supported by our nematic order parameter and network connectivity analysis.

2.5 Discussion

The results presented above serve to highlight some of the benefits, beyond increased computational efficiency, of relying on an anisotropic coarse-grained model for conjugated systems. In multiscale modeling, it is common to select coarse-grained parameters based on some form of statistical averaging over the configurations of a fine-grained model.[62, 122, 101, 102, 117, 90, 135, 98] In general, the more information that is removed during this averaging process, the more the "effects" of this information must be implicitly built back into the coarse-grained potential energy surfaces. The removal of information is the reason, for example, that coarse-grained interaction potentials often exhibit a stronger temperature or density dependence than the underlying detailed model, thereby limiting transferability. In the case of the coarse-grained model presented here, the chemical moieties that are transformed into coarse-grained disks are rigid; the atoms tend to vibrate slightly around their equilibrium positions, but no systematic rearrangements of the moieties occur. In fact, a recent study has shown that treating these moieties in conjugated systems as rigid bodies is sufficient for describing bulk morphology,[59] effectively reducing the number of independent

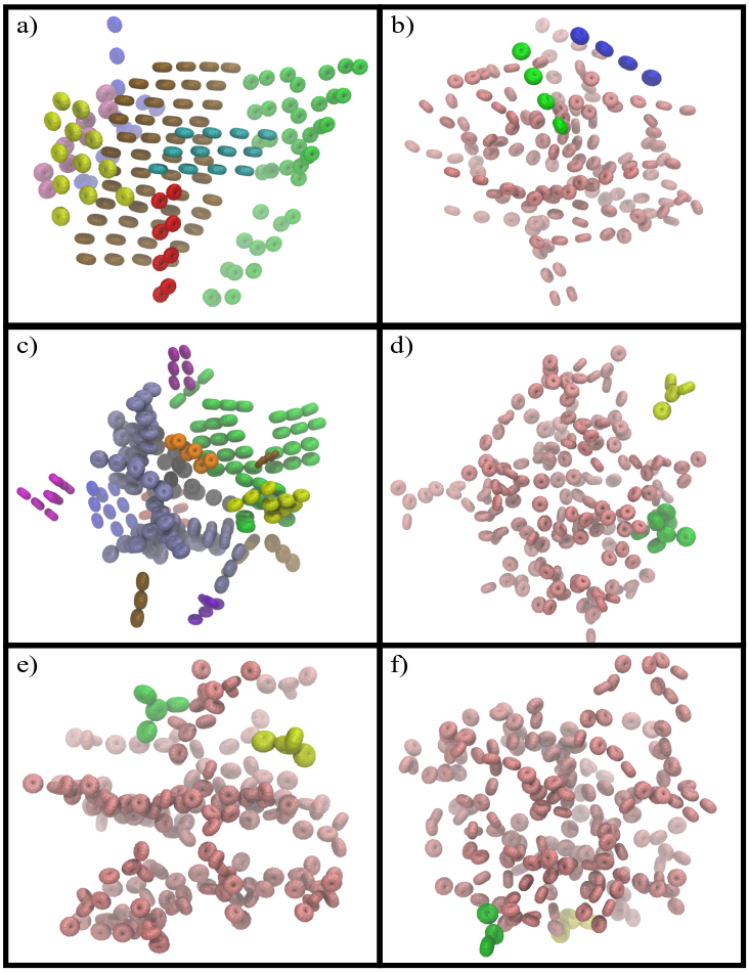

Figure 2.6: Visualized morphology networks with each color representing an independent unconnected subgraph for $\zeta = 0.075$. The morphologies are **a)** 4PDI, **b)** hPDI, **c)** Ph2b, **d)** TPH-30, **e)** TPH-90, and **f)** Ph2a. Side chains are not shown for clarity. All images shown here have unwrapped periodic boundary conditions. Note that planar molecules cluster into separate groups, while non-planar molecules form three-dimensional percolating networks. Additionally, when non-planar molecules fracture, only a few molecules break off and form unconnected subgraphs, while the unconnected subgraphs in planar molecules are larger.

degrees of freedom to the same level as the coarse-grained disk. The S-function expansion allows for a great deal of anisotropic information to be encoded within its functional form, and therefore reduces information loss during the coarse-graining process. For these reasons, we expect this coarse-grained model to have greater transferability across different temperatures and densities without having to adjust the interaction parameters, a hypothesis that is supported by the high accuracy shown for the benzene and ethylbenzene models at different temperatures and densities (Figure 2.2.

In addition to enhanced transferability, the coarse-grained model allows for meaningful optoelectronic analysis. The application of the coarse-grained model to PDI-based molecules is a simple demonstration to this end, where it is possible to isolate key structural features of interest and examine their effect on bulk charge percolation behavior while ignoring less relevant details at the atomistic level. Note that the full parameterization of an equivalent atomistic model would be a demanding process using traditional simulation approaches, but is rendered straightforward with the model introduced here. Furthermore, parameterization would be challenging for traditional coarse-grained approaches where crucial torsion and dihedral information would be eliminated. The minimal model of PDI used here suggests that small organic molecules with twisted and non-planar architecture disrupt crystallization within the bulk material, yet still promote connectivity. In general, these molecular structures more robustly form three-dimensional percolating charge transport networks in a disordered environment. In contrast, molecules with planar architectures readily crystallize and form strong connections between one or two other molecules. Although planar molecules form stronger connections than their non-planar counterparts, they do not form percolative networks as connections between individual crystalline regions are weak. These results support literature reports, which have hypothesized that rigid, planar structures are not necessarily better for efficient charge transport, and that properly constructed molecular architectures can exhibit robust charge transport even in disordered environments.[7]

More generally, this type of analysis could be extended beyond small organic acceptors

to other conjugated materials. The ability of the S-function expansion potential to describe arbitrarily anisotropic conjugated structures could be used to describe conjugated polymers and their backbones, thereby greatly accelerating simulations while simultaneously maintaining critical dihedral and orientational degrees of freedom. In the field of OPVs, such a model could be extended to describe mixtures of polymers and small molecules, including the spherical or near-spherical structure of fullerene and non-fullerene small-molecule acceptors. Such a model of a bulk heterojunction would allow access to greater time and length scales than is possible through atomistic simulations alone, while maintaining the monomer orientations necessary for performing qualitative analysis of intramolecular and intermolecular charge transport features in the bulk. Investigations of the application of this coarse-grained model to polymers and mixtures is currently underway, and will be presented in a future publication.

2.6 Conclusion

A flexible anisotropic coarse-grained model has been presented for the study of conjugated molecules. The model was conceived to capture the most important features of such systems for optoelectronic analysis. Applications to simple conjugated rings demonstrate quantitative agreement between the coarse-grained and atomistic descriptions for common structural properties. Coarse-graining of complex PDI-geometries relevant to small molecule organic acceptors is showcased as a straightforward application of the model to conjugated system geometries that are not amenable to traditional coarse-graining strategies. Simulations have provided chemical insights showing that the more non-planar and lower the symmetry of a molecular architecture, the more robustly that material's charge transport network percolates across the bulk structure. Molecules that are too planar tend to promote crystallization, which prevents three-dimensional charge percolation.

2.7 Appendix

2.7.1 Fits to Gay-Berne and S-Function Expansion Potentials

The Gay-Berne model for anisotropic interactions was found to be insufficient for modeling both benzene and perylene diimide (PDI), as it does not have enough parameters to properly describe their anisotropy. The Gay-Berne potential treats particles as ellipsoids. Whenever the particles cannot be accurately treated as ellipsoids, substantial error appears in the calculations. In the case of benzene, two molecules in the T-shaped configuration are at a closer distance than what an ellipsoidal structure would allow, so it fails to properly capture the distance of the minimum energy configuration. Figure 2.7 shows the potential energy fits of the benzene molecules using the Gay-Berne potential and the S-function potential. Note that in addition to the three orientations shown in Figure 2.7, 100 other randomly selected orientations were also sampled as a function of separation distance to fit to the two potential energy functions. The S-function expansion is more flexible when describing anisotropic interactions, so it is better at capturing the non-ellipsoidal character of the benzene molecule.

Figure 2.8 shows the potential energy fits for the PDI molecule in three representative configurations. Note that the S-function expansion is a uniaxial potential, while the PDI molecule has inherent biaxiality. The fitting procedure is averaged over all possible orientations that could be considered the "face-to-face" and "side-to-side" configurations, which is why the minimum energy fitted potential is not as large as that of the representative configurations shown.

2.7.2 Comparison of AA and CG RDF

Since PDI is glassy at 300 K, direct comparisons of atomistic and coarse-grained radial distribution functions for independently initialized simulations is difficult. Instead, we here show that the two representations are capable of stabilizing the same morphologies. Simu-

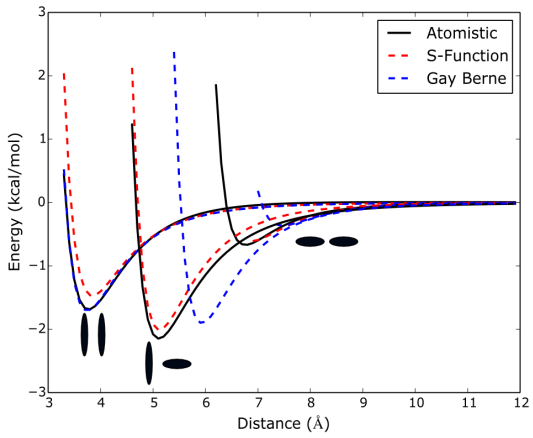

Figure 2.7: Comparison of benzene potential energy fits using the Gay-Berne model and the S-function expansion. Three representative orientations are shown. In addition to the displayed orientations, randomly selected orientations were also used in the fitting procedure.

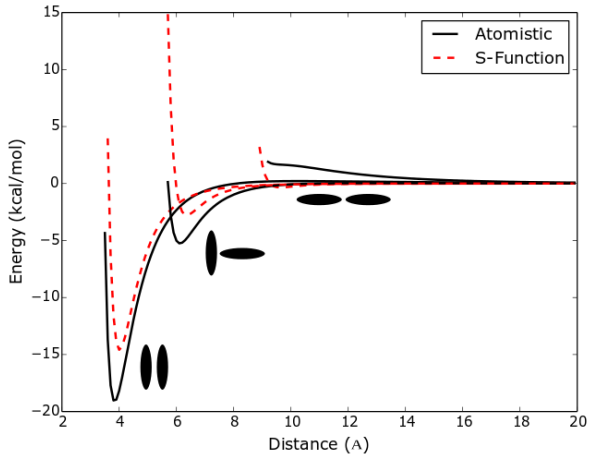

Figure 2.8: PDI potential energy fits using the S-function expansion for three representative orientations. Note that in addition to the displayed orientations, 100 other randomly selected orientations were also fit. Fitting was biased using the Boltzmann factor so that configurations with the deepest minima were fit more accurately.

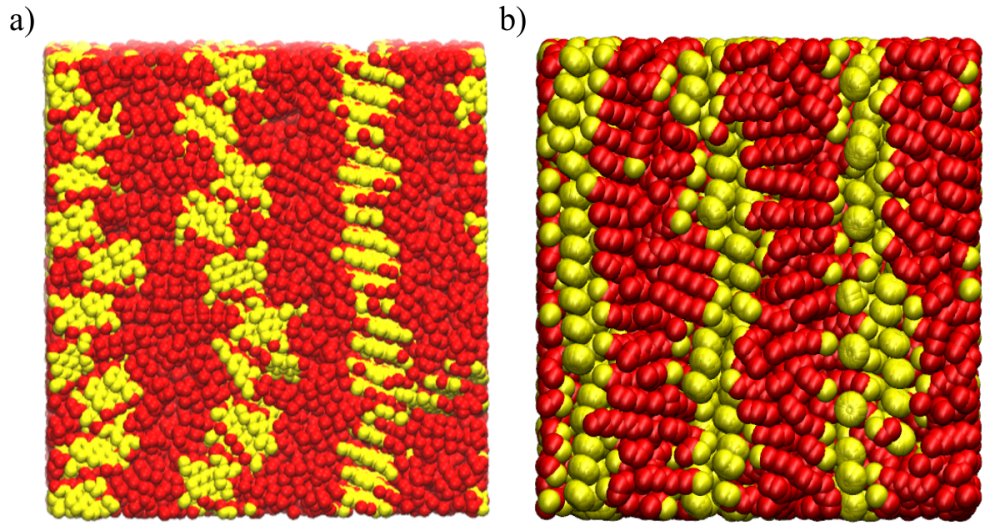

Figure 2.9: Comparison of all-atom (**a**) and coarse-grained morphologies (**b**) for perylene diimide. Conjugated blocks are colored yellow, while alkyl side chains are red. Coarse grained simulations were initialized by mapping from the atomistic configuration, and were then allowed to relax.

lations of 500 atomistic PDI molecules were cooled from 1000 K to 300 K and allowed to settle into a highly ordered morphology. The atomistic configuration was then mapped to a coarse-grained representation, which was then simulated at 300 K and allowed to relax. Figure 2.9 displays side-by-side comparisons of the fully relaxed atomistic and coarse-grained configurations, which are qualitatively similar. Figure 2.10 compares the radial distribution functions and nematic order parameters of the atomistic and coarse-grained models. As can be seen, the height of the peaks are slightly different, but the location of the peaks themselves are nearly identical. The nematic order parameter is also very similar. These results show that the coarse-graining procedure discussed in the Methods section is sufficient to generate models that stabilize the same morphologies.

2.7.3 S-Function Expansion

The S-Function expansion is a potential of the shifted Lennard-Jones form:

$$E_{nb} = \sum_{i=1}^{n} \sum_{i<j}^{n} U(\mathbf{f}_i, \mathbf{f}_j, \mathbf{r}_{ij}) \tag{2.7}$$

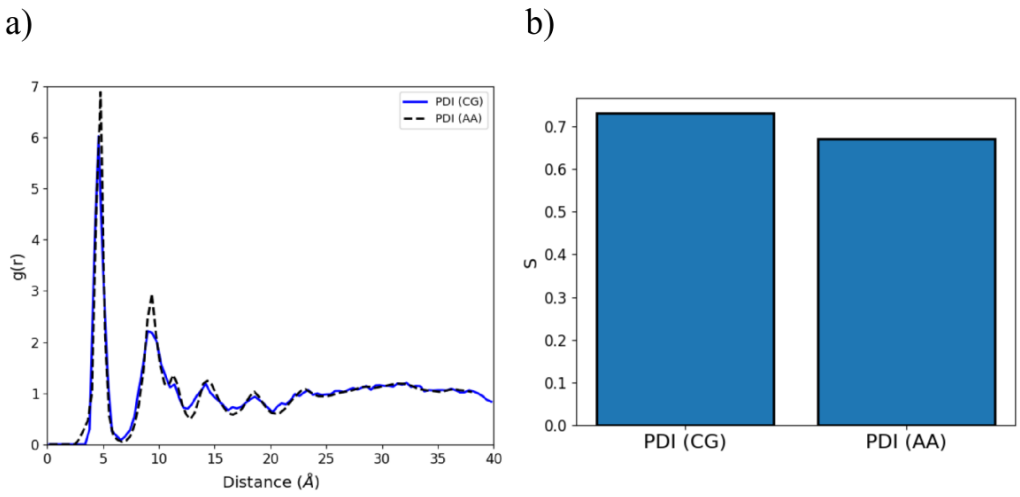

Figure 2.10: Comparison of all-atom and coarse-grained radial distribution functions (**a**) and nematic order parameters (**b**) for perylene diimide. Radial distribution functions were calculated between the center of mass of each molecule.

$$U(\mathbf{f}_i, \mathbf{f}_j, \mathbf{r}_{ij}) = 4\epsilon(\mathbf{f}_i, \mathbf{f}_j, \mathbf{r}_{ij}) \left[a^{12} - a^6\right] \tag{2.8}$$

$$a = \frac{\sigma_0}{|\mathbf{r}_{ij}| - \sigma(\mathbf{f}_i, \mathbf{f}_j, \mathbf{r}_{ij}) + \sigma_0} \tag{2.9}$$

The precise definition of $\sigma(\mathbf{f}_i, \mathbf{f}_j, \mathbf{r}_{ij})$ and $\epsilon(\mathbf{f}_i, \mathbf{f}_j, \mathbf{r}_{ij})$ depends on which types of particles are interacting. Within our model, there are three possible types of interactions: disk-disk, disk-bead, and bead-bead. For the bead-bead interactions, there is no orientation-dependence and $\sigma(\mathbf{f}_i, \mathbf{f}_j, \mathbf{r}_{ij}) = \sigma_0$ and $\epsilon(\mathbf{f}_i, \mathbf{f}_j, \mathbf{r}_{ij}) = \epsilon_0$ so the non-bonded potential reduces to the standard Lennard-Jones potential.

For disk-disk interactions, the orientation-dependence takes on the full S-function expansion form:

$$f_0 = \mathbf{f}_i \cdot \mathbf{f}_j; f_1 = \mathbf{f}_i \cdot \frac{\mathbf{r}_{ij}}{|\mathbf{r}_{ij}|}; f_2 = \mathbf{f}_j \cdot \frac{\mathbf{r}_{ij}}{|\mathbf{r}_{ij}|} \tag{2.10}$$

$$\sigma(\mathbf{f}_i, \mathbf{f}_j, \mathbf{r}_{ij}) \quad = \sigma_0[\sigma_{000} S_{000} + \sigma_{cc2}(S_{202} + S_{022})$$

$$+\sigma_{220}S_{220} + \sigma_{222}S_{222} + \sigma_{224}S_{224}] \tag{2.11}$$

$$\begin{aligned}\epsilon(\mathbf{f}_i, \mathbf{f}_j, \mathbf{r}_{ij}) &= \epsilon_0[\epsilon_{000}S_{000} + \epsilon_{cc2}(S_{202} + S_{022}) \\ &+\epsilon_{220}S_{220} + \epsilon_{222}S_{222} + \epsilon_{224}S_{224}]\end{aligned} \tag{2.12}$$

with

$$S_{000} = 1 \tag{2.13}$$

$$S_{202} = \frac{1}{2\sqrt{5}}\left(3f_1^2 - 1\right) \tag{2.14}$$

$$S_{022} = \frac{1}{2\sqrt{5}}\left(3f_2^2 - 1\right) \tag{2.15}$$

$$S_{220} = \frac{1}{2\sqrt{5}}\left(3f_0^2 - 1\right) \tag{2.16}$$

$$S_{222} = \frac{1}{\sqrt{70}}\left(2 - 3f_1^2 - 3f_2^2 - 3f_0^2 + 9f_1f_2f_0\right) \tag{2.17}$$

$$\begin{aligned}S_{224} = \frac{1}{4\sqrt{70}}(1 - 5f_1^2 - \quad & 5f_2^2 + 2f_0^2 - 20f_1f_2f_0 \\ & +35f_1^2f_2^2)\end{aligned} \tag{2.18}$$

The calculation for bead-disk interactions is similar. However, since one of the interacting

objects has no $\mathbf{f}$ vector, only f_1 can be meaningfully assigned.

$$\sigma(\mathbf{f}_i, \mathbf{f}_j, \mathbf{r}_{ij}) = \sigma_0 \left(\sigma_{000} S_{000} + \sigma_{cc2} S_{202}\right) \tag{2.19}$$

$$\epsilon(\mathbf{f}_i, \mathbf{f}_j, \mathbf{r}_{ij}) = \epsilon_0 \left(\epsilon_{000} S_{000} + \epsilon_{cc2} S_{202}\right) \tag{2.20}$$

In the cases of all forms of the interaction, the σ and ϵ variables are empirical parameters that need to be fit. In this work, they were determined through a least squares fitting of the underlying potential energy surface.

2.7.4 Dihedral Angles

OPLS-style dihedral potentials are used within the coarse-grained model to describe interactions between adjacent disks. While the standard 4-body dihedrals can be used within the model, more often it is useful to incorporate dihedral angles defined between only two disks. In such a case, the $\mathbf{f}$ vector is used in place of the displacement vector between two of the bodies. Figure 2.11 identifies the different cases for which the dihedral angle can be defined.

The dihedral angle can be determined from the following quantities, where $\mathbf{b}_1$, $\mathbf{b}_2$, and $\mathbf{b}_3$ are as defined in Figure 2.11 (These quantities will also be used for dihedral force and torque calculations).

$$c_{11} = \mathbf{b}_1 \cdot \mathbf{b}_1 \tag{2.21}$$

$$c_{22} = \mathbf{b}_2 \cdot \mathbf{b}_2 \tag{2.22}$$

$$c_{33} = \mathbf{b}_3 \cdot \mathbf{b}_3 \tag{2.23}$$

$$c_{12} = \mathbf{b}_1 \cdot \mathbf{b}_2 \tag{2.24}$$

$$c_{13} = \mathbf{b}_1 \cdot \mathbf{b}_3 \tag{2.25}$$

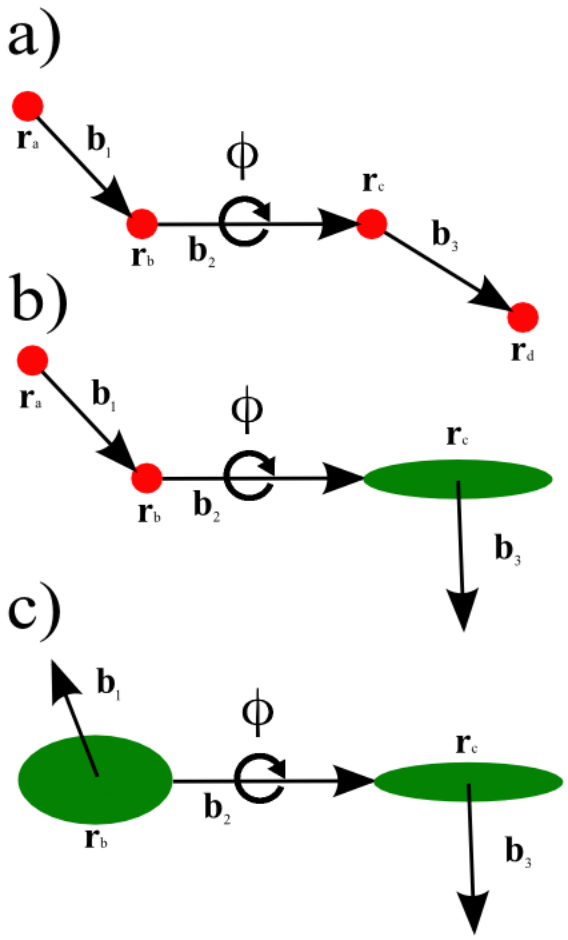

Figure 2.11: Dihedral angles can be defined within the model between **a)** four beads, **b)** two beads and a disk, or **c)** two disks. When a disk is present, the normal vector **f** is used to define one of the vectors necessary for specifying the two planes.

$$c_{23} = \mathbf{b}_2 \cdot \mathbf{b}_3 \tag{2.26}$$

$$d_{12} = c_{11}c_{22} - c_{12}^2 \tag{2.27}$$

$$d_{13} = c_{11}c_{33} - c_{13}^2 \tag{2.28}$$

$$d_{23} = c_{22}c_{33} - c_{23}^2 \tag{2.29}$$

$$\tag{2.30}$$

$$\cos(\phi) = \frac{c_{13}c_{22} - c_{23}c_{12}}{\sqrt{d_{23}d_{12}}} \tag{2.31}$$

2.7.5 S-Function Force Calculations

In order to implement this model for use in molecular dynamics, forces and torques must be calculated. The point force, $\mathbf{F}$, and the point torque, τ, acting on any uniaxial particle with position $\mathbf{r}$ and unit normal orientation vector $\mathbf{f}$ can be determined from the interaction potential, U.[3]

$$\mathbf{F} = -\frac{\partial U}{\partial \mathbf{r}} \tag{2.32}$$

$$\tau = -\mathbf{f} \times \frac{\partial U}{\partial \mathbf{f}} \tag{2.33}$$

We include here methods for calculating forces and torques for any orientation-dependent potential that is used within the model, specifically the S-function expansion for disk-disk and disk-bead interactions, as well as dihedral interactions when a disk is involved, and the additional torques and forces from the rigid attachment sites.

A good pedagogical outline for calculating the derivatives used in determining the forces and torques from the S-function expansion is given in Lequieu et al.[81] Here we only display the minimum equations necessary for performing the calculations. To be clear, for the pair potential, $\mathbf{F}_{ij}$ denotes the force acting on particle i from its pair interaction with particle j, τ_{ij} denotes the point torque acting on particle i from its pair interaction with particle j,

and $\mathbf{r}_{ij} = \mathbf{r}_i - \mathbf{r}_j$. The following is the definition for the disk-disk interaction.

$$\begin{aligned}\mathbf{F}_{ij} = -\left(\frac{\partial U}{\partial r_{ij}}\right)\frac{\mathbf{r}_{ij}}{r_{ij}} &- \left(\frac{\partial U}{\partial f_1}\right)\left(\frac{\mathbf{f}_i}{r_{ij}} - \frac{f_1\mathbf{r}_{ij}}{r_{ij}^2}\right) \\ &- \left(\frac{\partial U}{\partial f_2}\right)\left(\frac{\mathbf{f}_j}{r_{ij}} - \frac{f_2\mathbf{r}_{ij}}{r_{ij}^2}\right)\end{aligned} \tag{2.34}$$

$$\tau_{ij} = -\mathbf{f}_i \times \left[\left(\frac{\partial U}{\partial f_0}\right)\mathbf{f}_j + \left(\frac{\partial U}{\partial f_1}\right)\left(\frac{\mathbf{r}_{ij}}{r_{ij}}\right)\right] \tag{2.35}$$

$$\begin{aligned}\left(\frac{\partial U}{\partial r_{ij}}\right) &= 4\epsilon\frac{-12\sigma_0^{12}}{(r_{ij}-\sigma+\sigma_0)^{13}} \\ &+4\epsilon\frac{6\sigma_0^6}{(r_{ij}-\sigma+\sigma_0)^7}\end{aligned} \tag{2.36}$$

The derivatives with respect to f_0, f_1, and f_2 are of the same form and will be denoted simply as f.

$$\begin{aligned}\left(\frac{\partial U}{\partial f}\right) &= 4\frac{\partial\epsilon}{\partial f}\left(\frac{\sigma_0^{12}}{(r_{ij}-\sigma+\sigma_0)^{12}} - \frac{\sigma_0^6}{(r_{ij}-\sigma+\sigma_0)^6}\right) \\ &+4\epsilon\frac{\partial\sigma}{\partial f}\left(\frac{12\sigma_0^{12}}{(r_{ij}-\sigma+\sigma_0)^{13}} - \frac{6\sigma_0^6}{(r_{ij}-\sigma+\sigma_0)^7}\right)\end{aligned} \tag{2.37}$$

$$\begin{aligned}\frac{\partial\epsilon}{\partial f} &= \epsilon_0(\epsilon_{000}\frac{\partial S_{000}}{\partial f} + \epsilon_{cc2}\left(\frac{\partial S_{202}}{\partial f} + \frac{\partial S_{022}}{\partial f}\right) \\ &+\epsilon_{220}\frac{\partial S_{220}}{\partial f} + \epsilon_{222}\frac{\partial S_{222}}{\partial f} + \epsilon_{224}\frac{\partial S_{224}}{\partial f})\end{aligned} \tag{2.38}$$

$$\begin{aligned}\frac{\partial\sigma}{\partial f} &= \sigma_0(\sigma_{000}\frac{\partial S_{000}}{\partial f} + \sigma_{cc2}\left(\frac{\partial S_{202}}{\partial f} + \frac{\partial S_{022}}{\partial f}\right) \\ &+\sigma_{220}\frac{\partial S_{220}}{\partial f} + \sigma_{222}\frac{\partial S_{222}}{\partial f} + \sigma_{224}\frac{\partial S_{224}}{\partial f})\end{aligned} \tag{2.39}$$

$$\frac{\partial S_{000}}{\partial f_0} = 0 \tag{2.40}$$

$$\frac{\partial S_{000}}{\partial f_1} = 0 \tag{2.41}$$

$$\frac{\partial S_{000}}{\partial f_2} = 0 \tag{2.42}$$

$$\frac{\partial S_{202}}{\partial f_0} = 0 \tag{2.43}$$

$$\frac{\partial S_{202}}{\partial f_1} = 3f_1/\sqrt{5} \tag{2.44}$$

$$\frac{\partial S_{202}}{\partial f_2} = 0 \tag{2.45}$$

$$\frac{\partial S_{022}}{\partial f_0} = 0 \tag{2.46}$$

$$\frac{\partial S_{022}}{\partial f_1} = 0 \tag{2.47}$$

$$\frac{\partial S_{022}}{\partial f_2} = 3f_2/\sqrt{5} \tag{2.48}$$

$$\frac{\partial S_{220}}{\partial f_0} = 3f_0/\sqrt{5} \tag{2.49}$$

$$\frac{\partial S_{220}}{\partial f_1} = 0 \tag{2.50}$$

$$\frac{\partial S_{220}}{\partial f_2} = 0 \tag{2.51}$$

$$\frac{\partial S_{222}}{\partial f_0} = \left(9f_1f_2 - 6f_0\right)/\sqrt{70} \tag{2.52}$$

$$\frac{\partial S_{222}}{\partial f_1} = \left(9f_0f_2 - 6f_1\right)/\sqrt{70} \tag{2.53}$$

$$\frac{\partial S_{222}}{\partial f_2} = \left(9f_0f_1 - 6f_2\right)/\sqrt{70} \tag{2.54}$$

$$\frac{\partial S_{224}}{\partial f_0} = \left(4f_0 - 20f_1f_2\right)/4\sqrt{70} \tag{2.55}$$

$$\frac{\partial S_{224}}{\partial f_1} = \left(-10f_1 - 20f_0f_2 + 70f_1f_2^2\right)/4\sqrt{70} \tag{2.56}$$

$$\frac{\partial S_{224}}{\partial f_2} = \left(-10f_2 - 20f_0f_1 + 70f_2f_1^2\right)/4\sqrt{70} \tag{2.57}$$

$$\tag{2.58}$$

2.7.6 Dihedral Force and Torque Calculations

The form of the dihedral potential is given in Equation 1 and we will denote it here as U_d. The four-body dihedral forces between four beads is well-established, so here we only calculate forces and torques when a disk is involved in the interaction: cases **b** and **c** in Figure 2.11 where the disk may either be located at position $\mathbf{r}_b$ or $\mathbf{r}_c$. First, we define the

following quantities.

$$\frac{\partial U_d}{\partial \cos(\phi)} = -\frac{1}{2\sin(\phi)}[-k_1\sin(\phi) + 2k_2\sin(2\phi) - 2k_3\sin(3\phi) + 4k_4\sin(4\phi)] \tag{2.59}$$

$$f = -(c_{23}c_{12} - c_{13}c_{22}) \tag{2.60}$$

$$g = \sqrt{d_{23}d_{12}} \tag{2.61}$$

$$h_1 = 2c_{33}\mathbf{b}_2 - 2c_{23}\mathbf{b}_3 \tag{2.62}$$

$$h_2 = 2c_{11}\mathbf{b}_2 - 2c_{12}\mathbf{b}_1 \tag{2.63}$$

$$\frac{\partial \cos(\phi)}{\partial \mathbf{b}_1} = (-(c_{23}\mathbf{b}_2 - c_{22}\mathbf{b}_3)g - f(c_{22}\mathbf{b}_1 - c_{12}\mathbf{b}_2)\sqrt{d_{23}/d_{12}})/|g|^2 \tag{2.64}$$

$$\frac{\partial \cos(\phi)}{\partial \mathbf{b}_2} = (-(c_{12}\mathbf{b}_3 + c_{23}\mathbf{b}_1 - 2c_{13}\mathbf{b}_2)g - f(h_1 d_{12} + h_2 d_{23})/(2\sqrt{d_{12}d_{23}}))/|g|^2 \tag{2.65}$$

$$\frac{\partial \cos(\phi)}{\partial \mathbf{b}_3} = (-(c_{12}\mathbf{b}_2 - c_{22}\mathbf{b}_1)g - f(c_{22}\mathbf{b}_3 - c_{23}\mathbf{b}_2)\sqrt{d_{12}/d_{23}})/|g|^2 \tag{2.66}$$

For a disk located at position $\mathbf{r}_b$ the following defines the force and torque

$$\mathbf{F} = -\frac{\partial U_d}{\partial \mathbf{r}_b} = -\frac{\partial U_d}{\partial \cos(\phi)}\frac{\partial \cos(\phi)}{\partial \mathbf{r}_b} = \frac{\partial U_d}{\partial \cos(\phi)}\frac{\partial \cos(\phi)}{\partial \mathbf{b}_2} \tag{2.67}$$

$$\tau = -\mathbf{f} \times \frac{\partial U_d}{\partial \mathbf{f}} = -\mathbf{b}_1 \times \left(\frac{\partial U_d}{\partial \cos(\phi)} \frac{\partial \cos(\phi)}{\partial \mathbf{b}_1} \right) \tag{2.68}$$

And for a disk located at position $\mathbf{r}_c$.

$$\begin{aligned} \mathbf{F} &= -\frac{\partial U_d}{\partial \mathbf{r}_c} = -\frac{\partial U_d}{\partial \cos(\phi)} \frac{\partial \cos(\phi)}{\partial \mathbf{r}_c} \\ &= -\frac{\partial U_d}{\partial \cos(\phi)} \frac{\partial \cos(\phi)}{\partial \mathbf{b}_2} \end{aligned} \tag{2.69}$$

$$\tau = -\mathbf{f} \times \frac{\partial U_d}{\partial \mathbf{f}} = -\mathbf{b}_3 \times \left(\frac{\partial U_d}{\partial \cos(\phi)} \frac{\partial \cos(\phi)}{\partial \mathbf{b}_3} \right) \tag{2.70}$$

2.7.7 Benzene Parameters

The coarse-grained benzene model is represented entirely by anisotropic disks, so no bonded interactions are present. Included in the following table are the S-function parameters for the coarse-grained benzene model.

Table 2.2: Parameters for Coarse-Grained Benzene

σ_0	3.357
σ_{000}	1.588
σ_{cc2}	-0.698
σ_{220}	-0.175
σ_{222}	-0.268
σ_{224}	0.841
ϵ_0	1.4
ϵ_{000}	1.344
ϵ_{cc2}	1.090
ϵ_{220}	0.293
ϵ_{222}	0.063
ϵ_{224}	-4.152

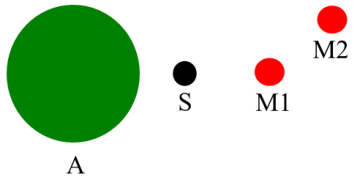

Figure 2.12: Schematic for coarse-grained ethylbenzene

.

2.7.8 Ethylbenzene Parameters

The coarse-grained ethylbenzene molecule consists of a single disk representing the aromatic ring and two beads representing methyl groups. A non-interacting rigid attachment site is also included to handle bonded interactions to the disk. Figure 2.12 provides a schematic of the model.

S-Function Parameters

Table 2.3: Parameters for Coarse-Grained Ethylbenzene

	A-A	A-M1 / A-M2	M1-M1	M2-M2
σ_0	3.45	3.129	4.068	4.152
σ_{000}	1.588	1.439		
σ_{cc2}	-0.698	-0.872		
σ_{220}	-0.175			
σ_{222}	-0.268			
σ_{224}	0.841			
ϵ_0	1.25	1.0	0.1986	0.25
ϵ_{000}	1.344	0.695		
ϵ_{cc2}	1.090	0.884		
ϵ_{220}	0.293			
ϵ_{222}	0.063			
ϵ_{224}	-4.152			

Table 2.4: Ethylbenzene Bonds

Bond	k_b	d_0
S-M1	604.0	1.52
M1-M2	496.0	1.532

Table 2.5: Ethylbenzene Angles

Angle	k_a	θ_0
A-S-M1	229.3	3.067
S-M1-M2	143.18	2.0

Bonded Interaction Parameters

2.7.9 PDI-based Molecule Parameters

S-Function Parameters

Non-bonded interactions occur between only two particles for all of the PDI-based molecules in this study: PDI disks (P) and methyl beads (M). The following table displays the S-function parameters for all possible interactions.

Bonded Interaction Parameters

hPDI and 4PDI

TPH, Ph2a, and Ph2b

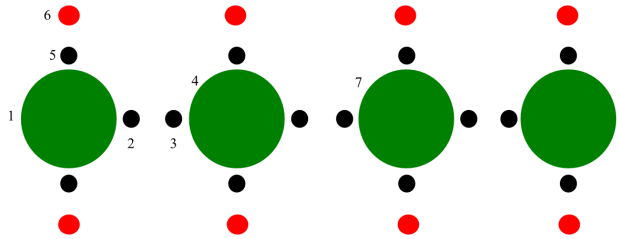

Figure 2.13: Schematic for coarse-grained hPDI and 4PDI. Note that only a single methyl group is depicted in the schematic, while octyl side chains were used in simulations.

.

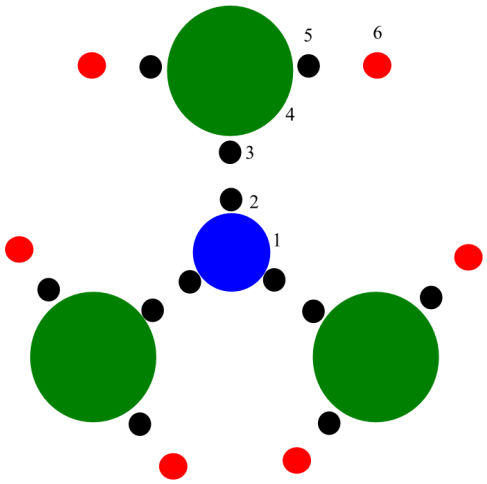

Figure 2.14: Schematic for coarse-grained TPH. The central blue disk is used only for bonded interactions and maintaining dihedral angles. It does not interact through the S-function potential. Ph2a and Ph2b are almost identical to this structure. The only difference is that one of the PDI components is removed (Ph2b additionally has a 180 degree angle between the PDI components as opposed to 120 degrees). Note that only a single methyl group is depicted in the schematic, while octyl side chains were used in simulations.

.

Table 2.6: Ethylbenzene Dihedrals

Dihedral	k_1	k_2	k_3	k_4
A-M1-M2	0.0	0.61	0.0	0.138

Table 2.7: Ethylbenzene Rigid Attachments

Attachment	u	f	v
A-S	1.4	0	0

Table 2.8: S-Function Parameters for Coarse-Grained PDI-based Molecules

	P-P	P-M	M-M
σ_0	3.09	3.621	4.152
σ_{000}	2.2276	1.478	
σ_{cc2}	-1.221	-0.902	
σ_{220}	-0.448		
σ_{222}	0.451		
σ_{224}	0.553		
ϵ_0	1.0	1.0	0.25
ϵ_{000}	2.943	0.733	
ϵ_{cc2}	8.429	2.833	
ϵ_{220}	3.756		
ϵ_{222}	8.178		
ϵ_{224}	2.005		

Table 2.9: hPDI and 4PDI Bonds (refer to Figure 2.13 for numerical labels)

Bond	k_b	d_0
2-3	1900	2.3
5-6	520	1.6
Alkyl	520	1.961

Table 2.10: hPDI and 4PDI Angles (refer to Figure 2.13 for numerical labels)

Angle	k_a	θ_0
1-2-3	400.0	3.142
1-5-6	126.0	3.142
Alkyl	126.0	1.961

Table 2.11: hPDI and 4PDI Dihedrals (refer to Figure 2.13 for numerical labels)

Dihedral	k_1	k_2	k_3	k_4
Alkyl	-3.4	1.25	-3.1	0.0
1-4 (hPDI)	463	-161.14	52.37	-41.14
1-4 (4PDI)	463	0.0	0.0	0.0
1-7 (hPDI)	107	-80.62	12.13	-41.26
1-7 (4PDI)	107	0.0	0.0	0.0

Table 2.12: hPDI and 4PDI Rigid Attachments (refer to Figure 2.13 for numerical labels)

Attachment	u	f	v
1-2	2.5	0	0
1-5	0	0	5.6

Table 2.13: TPH, Ph2a, and Ph2b Bonds (refer to Figure 2.14 for numerical labels)

Bond	k_b	d_0
2-3	1900	2.3
5-6	520	1.6
Alkyl	520	1.961

Table 2.14: TPH, Ph2a, and Ph2b Angles (refer to Figure 2.14 for numerical labels)

Angle	k_a	θ_0
1-2-3	400.0	3.142
2-3-4	400.0	3.142
4-5-6	126.0	3.142
Alkyl	126.0	1.961

Table 2.15: TPH, Ph2a, and Ph2b Dihedrals (refer to Figure 2.14 for numerical labels)

Dihedral	k_1	k_2	k_3	k_4
Alkyl	-3.4	1.25	-3.1	0.0
1-4 (TPH-30, Ph2a)	427	-161.24	48.46	-41.26
1-4 (TPH-60)	214	-161.24	24.26	-41.26
1-4 (TPH-90)	0	-161.24	0	-41.26
1-4 (Ph2b)	427	0	0	0

Table 2.16: TPH, Ph2a, and Ph2b Rigid Attachments (refer to Figure 2.14 for numerical labels)

Attachment	u	f	v
1-2	1.6	0	0
4-3	1.6	0	0
4-5	0	0	5.6

CHAPTER 3

CLUSTER FORMATION AND ALIGNMENT IN LIQUID CRYSTALLINE POLYMER BRUSHES

3.1 Abstract

Many theories have been developed for polymer brushes consisting of flexible chains, yielding straightforward scaling relations. However, many polymer brushes, such as those made from conjugated polymers or polypeptides, exhibit semiflexibility and cannot be accurately described using such theories. In this work, we study computational models of a polymer brush consisting of wormlike chains that experience nematic interactions. We find that such brushes have a stronger dependence on grafting density, as they cannot access many of the configurations available to flexible brushes. Furthermore, when nematic interactions are included, we find that the brush can undergo a nematic collapse into locally aligned clusters or a widespread tilted configuration. Under these conditions, the brush can display multiple morphologies as well as exhibit extremely rough surface topographies. At high polymer lengths, the conformational chain entropy is found to be the dominant factor, forcing the brush into an isotropic phase.

3.2 Introduction

Polymer brushes consist of chain molecules with one end covalently grafted onto a surface. When constrained in this manner, polymers have been known to display substantially different characteristics as compared to their behavior in the bulk. For example, if the grafting density is increased sufficiently high, the constituent polymers can experience stretching and tension rather than the random coil configurations they adopt in the bulk.[55, 66] Many desirable surface effects can be achieved from tuning brush properties, such as grafting density and polymer length. In particular, polymer brushes are well known for their ability

to prevent the adhesion of biological materials to surfaces as well as for their anti-fouling properties.[18] Additionally, they can be used to precisely control the preferential wetting properties of a surface.[88, 38]

In the realm of polymer theory, polymer brushes with flexible chains are the most widely studied. Under the assumption of highly flexible chains, the "Gaussian chain approximation" becomes accurate, and chain statistics and free energies of chain extension become straightforward.[2] This approximation predicts that flexible polymer brushes undergo a transition of sorts from a "mushroom" configuration to a stretched "brush" configuration as the polymer grafting density is increased.[20, 76] At low densities, each polymer is independent of the others and can explore many configurations, leading to the "mushroom" regime. Excluded volume effects become increasingly prominent as the density is increased and act to effectively repel the polymers from one another and eliminate many of the configurations that the freely grafted polymer can adopt. At a certain point, these excluded volume effects become so strong that the only available configurations are those where the polymer is stretched, leading to the "brush" regime. Scaling laws have been developed for such theories: within the mushroom regime, the brush height does not increase as density is increased. At a certain density, individual grafted chains begin to overlap, and the crossover from mushroom-to-brush occurs. The brush height has been shown to increase with density to the one third power under such conditions. Once the grafting density becomes so high that the finite extensibility of the polymer becomes important, the scaling exponent increases to a value greater than one third. These scaling behaviors have been confirmed experimentally.[147, 153, 12, 94, 4, 53, 151]

The behavior of semiflexible brushes is less studied.[76] Some examples of semiflexible brushes are those consisting of polypeptides or conjugated polymers (e.g. P3MT or P3HT). By definition, a semiflexible polymer has a persistence length on the same order of magnitude as the total polymer length. For such polymers, the Gaussian chain is a bad approximation because it allows the polymer to bend sharply in any direction.[126, 127] The height depen-

dence of a semiflexible polymer on grafting density can be expected to be more complicated than the flexible case. For example, semiflexible brushes have been known to transition out of the "mushroom" regime at lower grafting densities than would be expected of a flexible brush.[37] In fact, when sufficiently short, these semiflexible polymers are effectively rigid, so available conformations would be substantially different from the highly bent Gaussian chains. In addition to changes in scaling behavior, semiflexible polymers often show liquid crystal-like behavior: it is energetically favorable when all the polymers are aligned in the same direction. These effects often arise from π-π interactions between monomers of adjacent chains, inducing crystallization.[133, 132, 113]

Experimental studies have provided insight into semiflexible polymer brush behavior. In one study of P3MT brushes, it was found that as the length of the individual polymer strands in the brush was increased, the system underwent a change from an isotropically aligned brush, to an anisotropically tilted brush with semicrystalline behavior.[137] As the polymer length was increased further, the system returned to an isotropic brush. Additionally, the study found that the surface features of the brush were very rough with numerous columns with rounded tops. Similarly, another study[116] found that certain P3MT brushes took on aligned configurations with tilt angles of as much as 60 degrees which could allow them to experience enhanced thermal conductivity.

In this study, we examine the phase behavior of semiflexible polymers brushes that experience local nematic ordering. In particular, we place emphasis on how the interplay between enthalpic effects controlling polymer alignment and the entropic effects of increased chain length contributes to the variety of phases seen. The isotropic-to-nematic transition in the bulk polymer is examined as a function of both alignment energy as well as polymer length. Additionally, the behavior of semiflexible polymer brushes was examined under three nematic interaction conditions: no nematic interactions, nematic interactions in the brush only, and nematic interactions in both the brush and solvent.

The case of the nematic brush in isotropic solvent shows particularly complicated phase

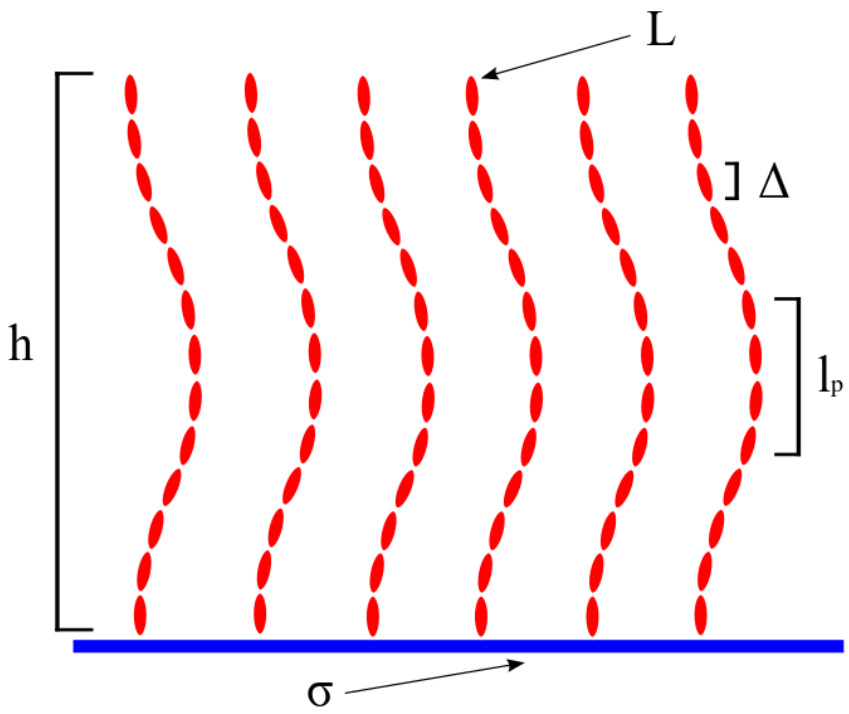

Figure 3.1: Schematic for the semiflexible polymer brushes examined in this work. The orientation of each discrete unit of the polymer is indicated by the elongated axis of the ellipse. The parameters studied in this work are the following: l_p is the persistence length of the polymer brush (4 discrete units in this work). Δ is the length of a single discrete polymer unit. L is the length of a fully extended polymer. h is the average height of the brush. σ is the grafting density of the brush. All parameters in this work describing length are in units of l_p.

behavior. For certain values of the nematic interaction parameter, the brush collapses into an anisotropic tilted configuration. Depending on the grafting density and polymer length, the brush may collapse into large uniformly aligned regions or into individual clusters which are randomly aligned. We investigate the nature of this nematic collapse and how it is changed with grafting density and polymer length. In addition, we examine how correlated these aligned structures are, and describe the effects of different polymer parameters on these correlations.

3.3 Model and Methods

3.3.1 Nematic Semiflexible Polymer Model

The model used in this work is based on the theoretically informed coarse-grained model that has been used extensively in the past for simulating flexible polymeric systems, such as block copolymer melts and homopolymer blends.[30, 112, 114] Two modifications have been made that allow for the investigation of the phenomena of interest here. First, rather than each polymer being treated as a Gaussian bead-spring chain, each polymer is modeled as a wormlike chain. Specifically, the discrete wormlike chain[74] is used to capture both the semiflexibity and finite extensibility of liquid crystalline polymers. With the discrete wormlike chain, an inextensible polymer of arc-length L is discretized into N beads, representing a segment of the continuous curve. The bonds between each bead are rigid, and the entirety of the intramolecular interaction energy comes from the following energy term:

$$\frac{H_b}{k_B T} = \sum_{i=1}^{N-2} k_b \cos\theta_i = \sum_{i=1}^{N-2} \frac{l_p}{\Delta} \cos\theta_i \tag{3.1}$$

where θ_i is the angle between beads i, $i+1$, and $i+2$, and where k_b is the bending energy coefficient, which is equivalent to l_p/Δ, where l_p is the persistence length of the polymer, and Δ is the length of a discretized unit of the wormlike chain. It has been shown[74] that the statistical behavior of the discrete wormlike chain accurately reproduces the continuous wormlike chain for discretization values $\Delta \leq 0.3\ l_p$. In this work, $\Delta = 0.25\ l_p$.

The second modification to the model is the addition of an energetic Maier-Saupe nematic interaction term (μ). The soft-core interaction energies are commonly expressed as a functional over the instantaneous polymer density fields which can be calculated using numerical grid-based approximation techniques,[30] and include a Flory-Huggins interaction term (χ) as well as an energy term that punishes deviations from the mean density (κ). Similar to these two terms, the Maier-Saupe interaction is a local interaction defined across

a finite distance, so that it can easily be incorporated into the same grid-based calculations. The overall non-bonded interaction energy is of the following form:

$$\frac{H_{nb}}{k_BT} = \rho_0 \int \chi\phi_A\phi_B + \frac{\kappa}{2}(\phi_A + \phi_B)^2 d\mathbf{r} - \frac{\mu\Delta^2}{\rho_0 V_{int}} \sum_{i<j} (\mathbf{u}_i \cdot \mathbf{u}_j)^2 \Gamma(\mathbf{r}_i, \mathbf{r}_j) \tag{3.2}$$

where $\mathbf{u}$ is the tangent vector of the wormlike chain given at a single bead, which can be calculated using finite difference methods from the locations of the beads along the chain. Γ is a function of the relative positions of two beads that regulates the interaction strength. Γ is unity if the distance between the two beads is less than some "interaction distance" and zero otherwise, while V_{int} is the "interaction volume" around any given bead: $V_{int} = \int_V \Gamma(\mathbf{r}_i, \mathbf{r}_j) d\mathbf{r}_i$. It should be noted here that ρ_0 refers to the "persistence-length density" and not the bead density, and is thus independent of the discretization length, Δ. The sum in the final term of the equation is over all pairs of beads. The prefactor was selected to make this energy term independent of both the discretization length, as well as the interaction distance, which is represented by V_{int}.

All lengths presented here are in units of the polymer persistence length, l_p. Simulations were performed by discretizing the non-bonded potential into a grid using the particle-to-mesh technique at the PM0 level with a randomly moving grid.[30] In the case of the PM0 approximation technique, the Maier-Saupe interaction becomes particularly simple: $\Gamma(\mathbf{r}_i, \mathbf{r}_j)$ is nonzero only for beads within the same grid cell, and V_{int} is the grid cell volume. In PM0, if κ is selected to be larger than μ, then the system can be shown to be thermodynamically stable.

Brushes were simulated at grafting density σ on a substrate of area A by tethering σA semiflexible polymers to a flat surface in a random pattern. Solvent molecules were included in brush simulations and were modeled as semiflexible polymers with length of 0.75 l_p (three beads) so that they can also incorporate nematic interactions when necessary.

Figure 5.1 provides a schematic for the system, and outlines all of the important variables discussed in the previous paragraphs.

3.3.2 Order Parameter Correlation Function Calculations

Correlation functions were calculated from brushes undergoing nematic collapse using the following strategy. A two-dimensional Q-tensor field was calculated using the following formula from the brush segments:

$$Q(x,y) = \frac{1}{N_g} \sum_{i=1}^{N_g} \left(\frac{3}{2} \mathbf{u}_i \mathbf{u}_i^T - \frac{1}{2} \mathbf{I} \right) \tag{3.3}$$

Where the sum is over all beads within a grid cell located at coordinate (x, y), N_g is the number of beads in that grid cell, and $\mathbf{I}$ is the unit tensor. A director field was then calculated from the Q-tensor field as the eigenvector associated with the greatest eigenvalue of the Q-tensor at each position. This unit vector was then projected onto the XY plane and renormalized into another unit vector, $\mathbf{n}$. $\mathbf{n}$ represents an order parameter for the local symmetry breaking that occurs when the brush undergoes nematic collapse. Correlation functions of this order parameter were calculated as the following:

$$C(x,y) = \\ \frac{1}{A} \int \int \left\langle \mathbf{n}(x',y') \cdot \mathbf{n}(x'+x, y'+y) \right\rangle dx' dy' \tag{3.4}$$

To analyze these correlation functions, it was assumed that they were radially symmetric and experience exponential decay. The radial correlation function, $C(r)$, was fit to a function of the form:

$$C(r) = \exp\left(-r/\lambda\right) \tag{3.5}$$

Where λ is defined to be the correlation length of the system.

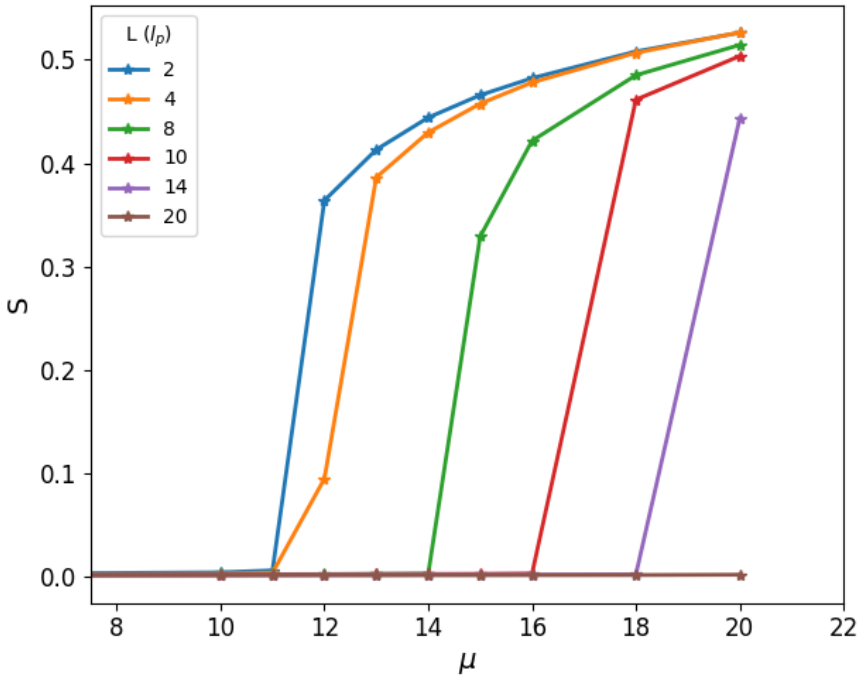

Figure 3.2: Plot of nematic order parameter (S) as a function of Maier-Saupe parameter (μ) for different polymer lengths (L). With the exception of $L = 20$, the polymer undergoes a first order isotropic-to-nematic transition at a finite value of μ. The necessary value of μ for this transition to take place increases with L, which reflects the increased conformational entropy which can counteract μ.

3.4 Results

3.4.1 Bulk Polymer - Height Dependence on Chain Length and Nematic Interaction Strength

In order to pinpoint the phase behavior of the polymer, several simulations were performed in the bulk at varying chain lengths and values of the nematic interaction parameter, μ. Simulations were performed in a cube with side lengths of 16 l_p and 280,000 total beads. The number of chains varied depending on the chain length. In all cases, κ was set to 20.0. The grid was selected to have a length of 0.75 l_p. Figure 3.2 shows the nematic order parameter (S) dependence on μ for several chain lengths. As can be seen, for sufficiently short chain lengths, the polymer undergoes what appears to be a first-order phase transition

from the isotropic phase to the nematic phase, which agrees with previous studies and models of nematic polymers.[114]. The value of μ at which the phase transition occurs also appears to depend strongly on the chain length: polymers of larger length require larger values of the nematic interaction parameter to enter a nematic phase. As the polymer gets longer, it can bend and twist more easily, allowing it to sample from more conformations. This increased conformational entropy allows it to resist the energetic driving force to align everywhere.

This result appears to contradict results from previous studies[114, 46] where the polymer length has no effect on the isotropic-to-nematic transition location. However, in these other papers the nematic term represents a Landau-de Gennes free energy of alignment associated with the Q-tensor order parameter. Here, it represents the potential energy of alignment. Since the Landau-de Gennes model uses a continuous free energy, which accounts for entropic effects, the isotropic-to-nematic transition is independent of the polymer length. A benefit of using a Maier-Saupe potential energy over a Landau-de Gennes free energy is that the potential energy is a chain-chain interaction. Intuitively, the potential energy represents a property that can be calculated by taking into consideration the interactions of only a few particles, similar to the Flory-Huggins χ parameter. Additionally, since these interactions are pairwise, they should not change as the composition of the system or density changes. In contrast, the Landau-de Gennes free energy does not directly correspond to an interaction at the polymer length scale, but rather a continuum free energy density which could complicate comparisons to experimental systems. Since the free energy parameters may not be independent of the system composition, it would be poorly suited to studies of polymer brushes where changing densities and compositions can have large effects.

3.4.2 Polymer Brush - Grafting Density and Nematic Interactions

Simulations were performed of semiflexible polymer brushes across a range of grafting densities under three conditions: no nematic interactions, nematic brush only, and nematic brush with nematic solvent. In all cases, κ was set to 20.0, while μ was either 0.0 or 20.0

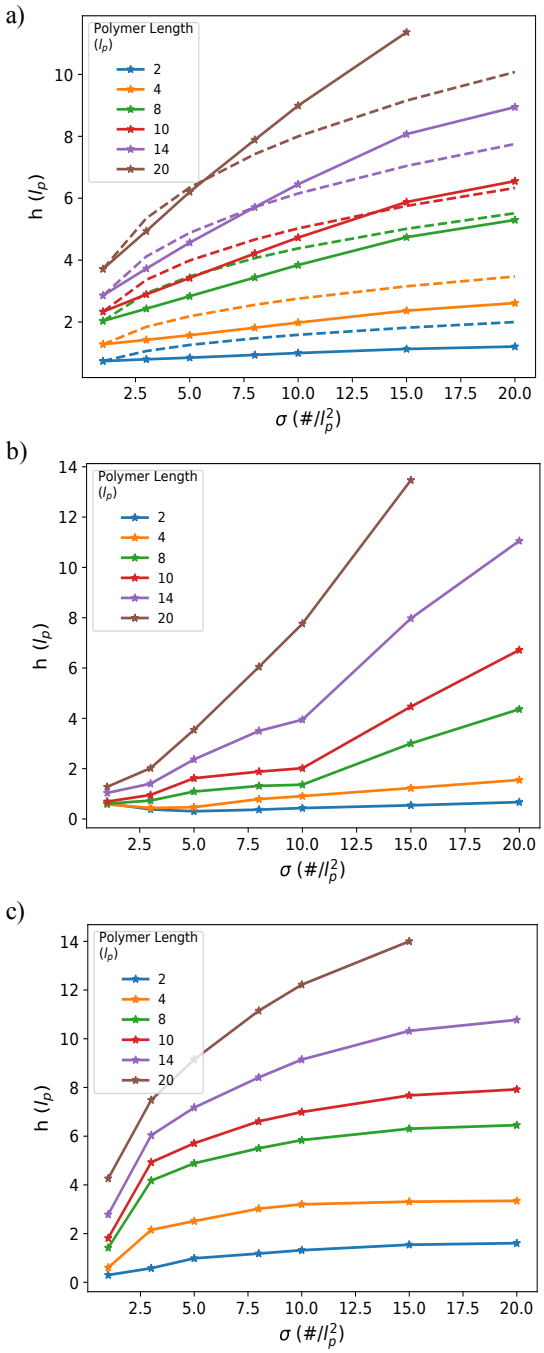

Figure 3.3: Brush height (h) dependence on grafting density (σ). **a)** shows the dependence for a system with $\kappa = 20.0$ and $\mu = 0.0$ while **b)** shows the dependence for a system with a nematic brush with $\kappa = 20.0$ and $\mu = 20.0$ and **c)** shows the dependence for a system with a nematic solvent in addition to the brush. Dotted lines in **a)** show the expected scaling behavior for an ideal flexible chain.

depending on which nematic interactions were considered. Simulation box dimensions were 16 $l_p \times 16\ l_p \times 20\ l_p$, and solvent molecules were generated so that there were 350,000 total beads in the system (solvent and brush combined) for all simulations (350,000 beads corresponds to 87,500 persistence length segments, or $\rho_0 = 17.1$). Additionally, the grid was chosen to have a length of 0.75 l_p on all sides, which allows for approximately 25 beads to be interacting within each grid cell.

Figure 3.3 displays plots of brush height as a function of grafting density. The behavior when there are no nematic interactions (Figure 3.3a) is straightforward, as the brush height increases monotonically with grafting density. The dotted lines on Figure 3.3a show the grafting density dependence that would be expected from an ideal flexible brush with Gaussian statistics at moderate stretching, where $h \sim \sigma^{1/3}$. As can be appreciated from Figure 3.3a, there are several notable differences between the semiflexible brush and the equivalent Gaussian brush. First, for short polymers ($L \leq 4\ l_p$) the height of the semiflexible brush increases more slowly than the flexible brush for all densities examined. The reason for this result is that the short polymers are so rigid that they are near full extension even at low densities. As the grafting density is increased and excluded volume effects become more important, they have minimal effect on the polymer as it cannot be stretched further. Second, the longer polymers all experience a scaling exponent that is greater than the ideal flexible case, i.e. $h \sim \sigma^{\nu}$ with $\nu \geq 1/3$, which can be clearly seen by how the semiflexible brush height increases past the flexible brush height for greater σ. A possible explanation for this is similar to what was suggested before. The semiflexible brushes are already fairly rigid. As the density is increased, the available positions that the chain can inhabit decreases more readily than a Gaussian chain because a lot of these positions would require the chain to contort into highly bent, high energy configurations. In effect, the energetically permissible configurations for the semiflexible brush are much more rigid and straightened than those of the flexible Gaussian brush, forcing it to adopt a large scaling exponent. In a sense, the semiflexible brush is similar to a flexible brush in the highly stretched regime where the

scaling exponent is greater than 1/3. However, unlike the flexible brush where the stretching is caused by excluded volume effects from the high density polymer, the semiflexible brush is straightened because of the rigidity of the backbone. Naturally, as the polymer gets larger, it can be expected to behave more like a flexible Gaussian chain, especially at low values of σ.

Figure 3.3b shows the brush height dependence on σ for a polymer brush that has nematic interactions in the presence of a non-interacting solvent. As can be seen, the behavior is not as straightforward as the case where no nematic interactions are present. For short polymers ($L \leq 4\ l_p$), h decreases as the grafting density increases before eventually increasing again at higher grafting density. The reason for this result is that as density is increased, the polymer begins to lie along the surface of the substrate in order to align with its neighbors, forming small clusters of randomly aligned polymers. This behavior lowers the total energy of the system. As the density increases, the polymers overlap more and more until they reach the point where aligning along the surface is no longer advantageous. At a high enough density, the polymer uniformly aligns throughout the film and stands up to form a tilted, but aligned configuration. For longer polymers, the situation is similar. In comparison to the semiflexible brush without nematic interactions, the nematic brush can be seen to have smaller brush heights at low grafting density while having a larger height at high grafting density. At low density, the longer polymers lie along the surface, albeit aligned in the same direction rather than forming randomly aligned clusters like the shorter polymers. As the density is increased, they also undergo a transition to the tilted aligned configuration. Polymers of intermediate length ($L = 4$, 8, and 10) demonstrate interesting morphologies as they undergo the planar-to-tilted transition, which is remarked upon further in the next section.

Figure 3.3c shows the brush height dependence on σ for a nematic brush in a nematic solvent. Similar to the case of no nematic interactions and unlike the case of the nematic brush only, it shows a monotonically increasing height dependence on σ. The brush height

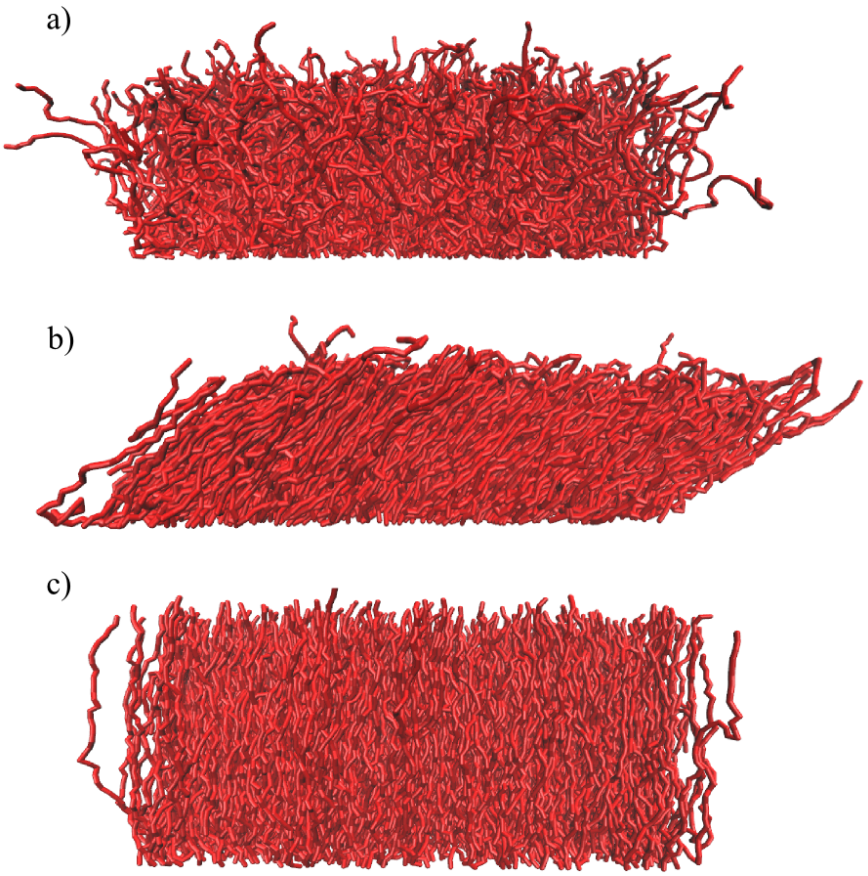

Figure 3.4: Side view images of the semiflexible brush under three separate conditions. **a)** has only excluded volume interactions, **b)** includes nematic brush interactions, and **c)** includes both nematic brush and nematic solvent interactions. The solvent is not shown in these images for clarity.

increases noticeably faster with both σ and L than the case of no nematic interactions. The nematic interactions between the brush and solvent allow the solvent to more easily mix into the brush, both swelling the brush and stabilizing it in a rigid vertical configuration.

Figure 3.4 shows representative side view images of the system with $L = 10\ l_p$ and $\sigma = 10\ l_p^{-2}$ in the three cases. At this grafting density and polymer length, the density of polymer units is high enough that the brush uniformly coats the substrate and does not form the independent clusters discussed in the following section. In Figure 3.4a, it can be seen that the excluded volume effects force the polymers to stand up on average. However, individual chains still have coils and turns when no nematic interactions are present. In contrast, Figures 3.4b and c show that individual polymer chains are more extended with

nematic interactions, where the energy decreases when neighboring polymers align. In the case of the isotropic solvent, it becomes energetically favorable for the brush to expel all of the solvent and form a high density layer near the substrate. These conditions allow for the maximum amount of alignment between neighboring polymer strands. This separation of polymer from the solvent does force the polymer to take on a tilted configuration relative to what is seen when no nematic interactions are present and thus lowers the height of the brush. In the case of the nematic solvent, the brush is stabilized by nematic interactions with the solvent, which allow the two components to mix more thoroughly than the other two cases would allow, which forces the brush to swell considerably, while still remaining aligned with neighboring polymer chains and solvent molecules.

3.4.3 Polymer Brush - Correlation Lengths and Domain Formation

The morphological behavior of the nematic brush in isotropic solvent is here further examined. As was mentioned in the discussion of Figure 3.3b, shorter polymers in these conditions undergo a transition from randomly oriented clusters of aligned polymers to a uniformly aligned tilted configuration as the grafting density is increased. Representative examples of this transition are shown for a brush with $L = 4\ l_p$ at different grafting densities in Figure 3.5. The simulation boxes shown in Figure 3.5 are for a system that is four times as large as the systems discussed in the last section, with dimensions of $32\ l_p \times 32\ l_p \times 20\ l_p$, but with the same intensive parameters. A good example of the independently aligned clusters can be found in Figure 3.5a, which is at a low grafting density. As the grafting density is increased, these clusters overlap and join together to form different domains, each of which begin to stand up and form a tilted configuration. While energetically, it is most favorable for all polymers to align in the same direction, entropically there are many different directions for the polymer to choose from and it can become trapped in a structure representing a local minimum free energy configuration. Figure 3.5e provides an example of a morphology where the minimum energy configuration would occur when the brush is uniformly aligned,

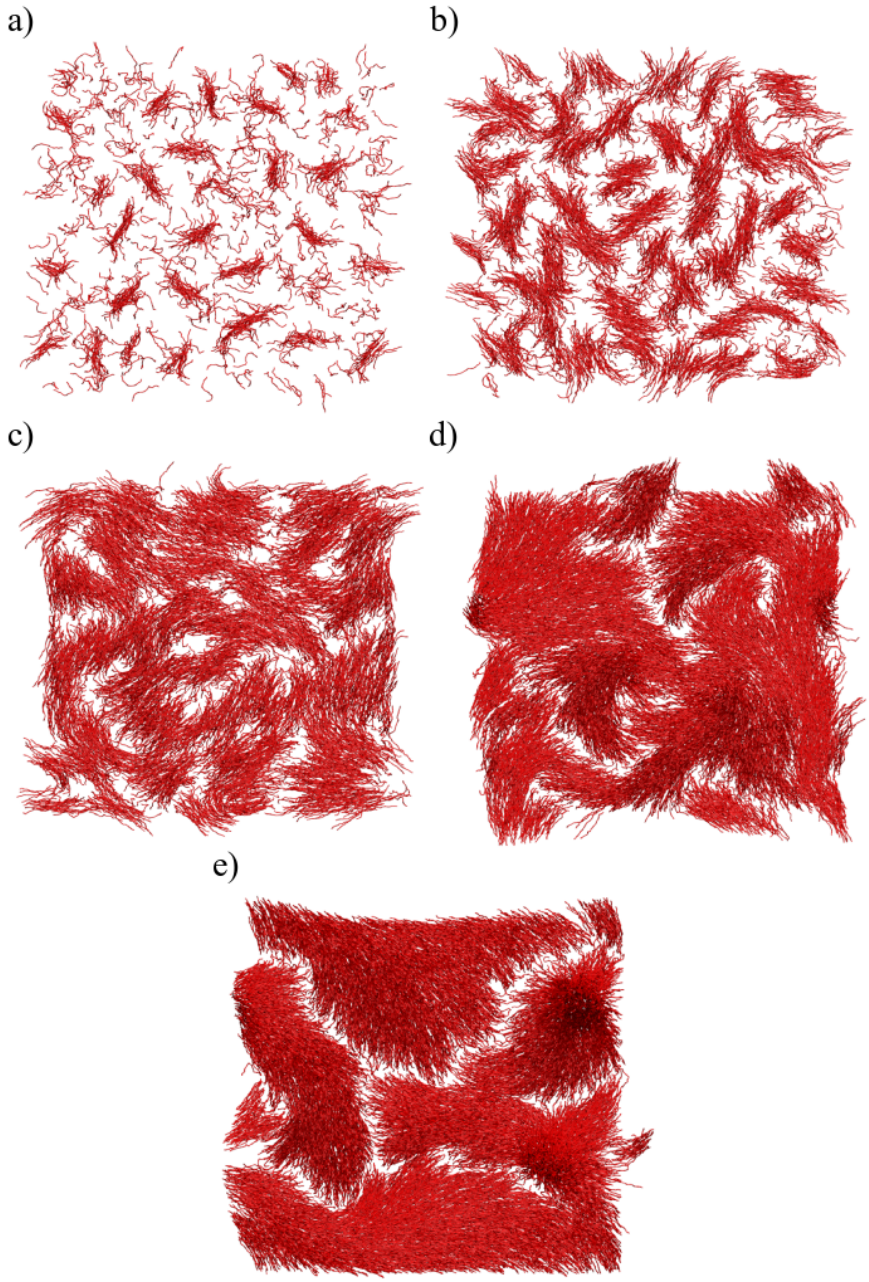

Figure 3.5: Top-down images of the brush morphology at different grafting densities, σ. Each brush polymer has length $L = 4\ l_p$ with $\kappa = 20.0$ and $\mu = 20.0$. Grafting densities are **a)** 1, **b)** 3, **c)** 5, **d)** 8, and **e)** 10 l_p^{-2}.

but instead forms defective microstructures. Eventually the grafting density becomes large enough that excluded volume effects force the polymer to align uniformly throughout the system.

In addition to the grafting density, the polymer length can affect the morphology of the brush. Increasing the polymer length can have effects similar to those of increasing the grafting density: the polymer density increases, so the polymer can align over larger length scales and undergo a similar transition from randomly aligned clusters to a homogeneously aligned brush. In addition to increasing correlation lengths, increasing the polymer length also increases the conformational entropy associated with each molecule which allows it to resist the energetic driving force to align, similar to what happens when the bulk polymer is considered. Figure 3.6 displays a few representative brush morphologies at different polymer lengths but with the same grafting density. At short lengths (Figure 3.6a) small clusters can form, but do not remain uniformly aligned over large distances. At longer chain lengths (Figure 3.6b) the polymers are capable of overlapping more. However, unlike the shorter polymer at high grafting density shown in Figure 3.5e, the polymers in Figure 3.6b display substantially more disorder. This disorder overtakes the nematic interactions at the longest polymer lengths (Figure 3.6c) in which the brush becomes isotropic. These results correspond well with experimental studies of P3MT brushes,[137] where it has been shown that increasing the polymer length causes the brush to transition from an anisotropically aligned structure to an isotropic brush.

The scalar nematic order parameter, S, does not work well to describe these different brush phases and the transitions between them. Even idealized Gaussian brushes will stand on end if the grafting density is high enough, leading to a nonzero value of S. The two-dimensional alignment correlation length, λ (as described in the Methods), is a more suitable order parameter for studying this transition. For a completely isotropic brush, there will be no alignment correlation and $\lambda = 0$. For systems where individually aligned clusters form, λ will take on a finite but nonzero value. For any systems that are homogeneously aligned,

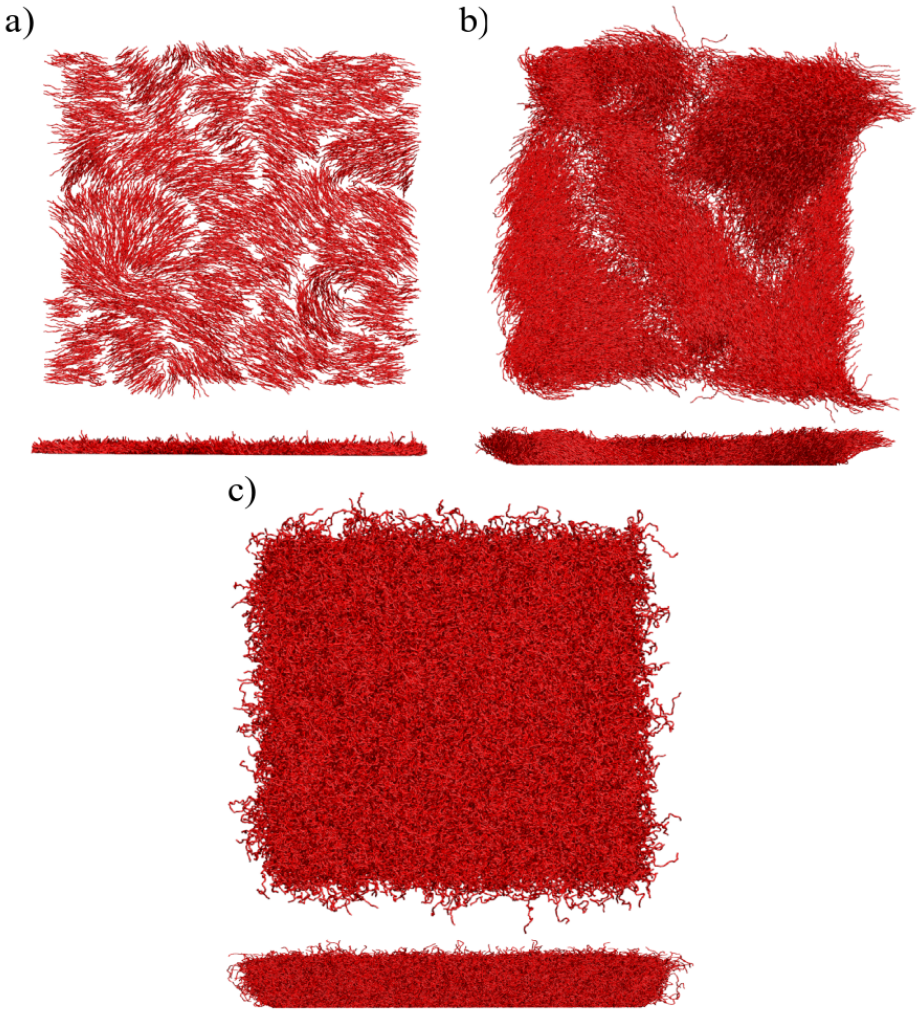

Figure 3.6: Top-down and side-view images of brush morphology at different polymer lengths (L): **a)** $L = 2.0$, **b)** $L = 8.0$, **c)** $L = 16.0\ l_p$, all at $\sigma = 8.0\ l_p^{-2}$. As the polymer length increases, the behavior of the brush changes from locally aligned clusters, to a fully aligned brush, to an isotropic brush.

λ will diverge (or become very large) as the alignment correlation increases rapidly.

Figure 3.7 provides two ways of visualizing the phases that the nematic polymer brush can adopt, displaying λ at several different polymer lengths (L) and grafting densities for systems with $\mu = 20$ and $\kappa = 20$. Figure 3.7a is a traditional plot of λ versus polymer length at different grafting densities, while Figure 3.7b provides a heat map of the same data. For low σ and low L, there is not enough polymer available to align properly, so λ stays close to zero. As σ increases, the polymer begins to become more strongly aligned at certain values of L where the brush begins to form clusters of aligned polymer (e.g. $L = 8.0$, $\sigma = 5$). For lower grafting densities ($\sigma \leq 6\ l_p^{-2}$), λ reaches a maximum value with L before decreasing again; the system simply is not dense enough to align fully. However, as the grafting density is increased further ($\sigma \geq 7$), there are entire ranges of L for which λ increases rapidly beyond the size of the simulation box, and the brush prefers to adopt a uniformly aligned state.

In all grafting densities shown in Figure 3.7, λ drops sharply to zero for high enough L. At this point, the conformational entropy associated with each polymer dominates over the potential energy associated with alignment, and the polymer brush becomes isotropic. Again, these effects can be seen directly in Figures 3.5 and 3.6.

In addition to the formation of clusters, the nematic collapse of the polymer brush can induce dramatic changes in the height of the brush at different points along the substrate, depending on how the polymer is aligned. Figure 3.8 visualizes some of these differences in brush height. Specifically, in areas where the brush is well aligned, the polymers tend to lie flat, and the brush height tends to be low. In areas where there is a defect in the alignment of the brush, the polymer chains tend to stand up, leading to dramatic surface topography. In Figure 3.8a and b, two regions near the right side of the image can be seen to be have something like point defects, where the polymer chains surrounding the defect all point towards it. Figure 3.8c display slices of brush heights corresponding to the lines in Figure 3.8a, showing that the defects can cause the brush heights immediately surrounding the defects to increase by factors greater than two. These defective regions provide an

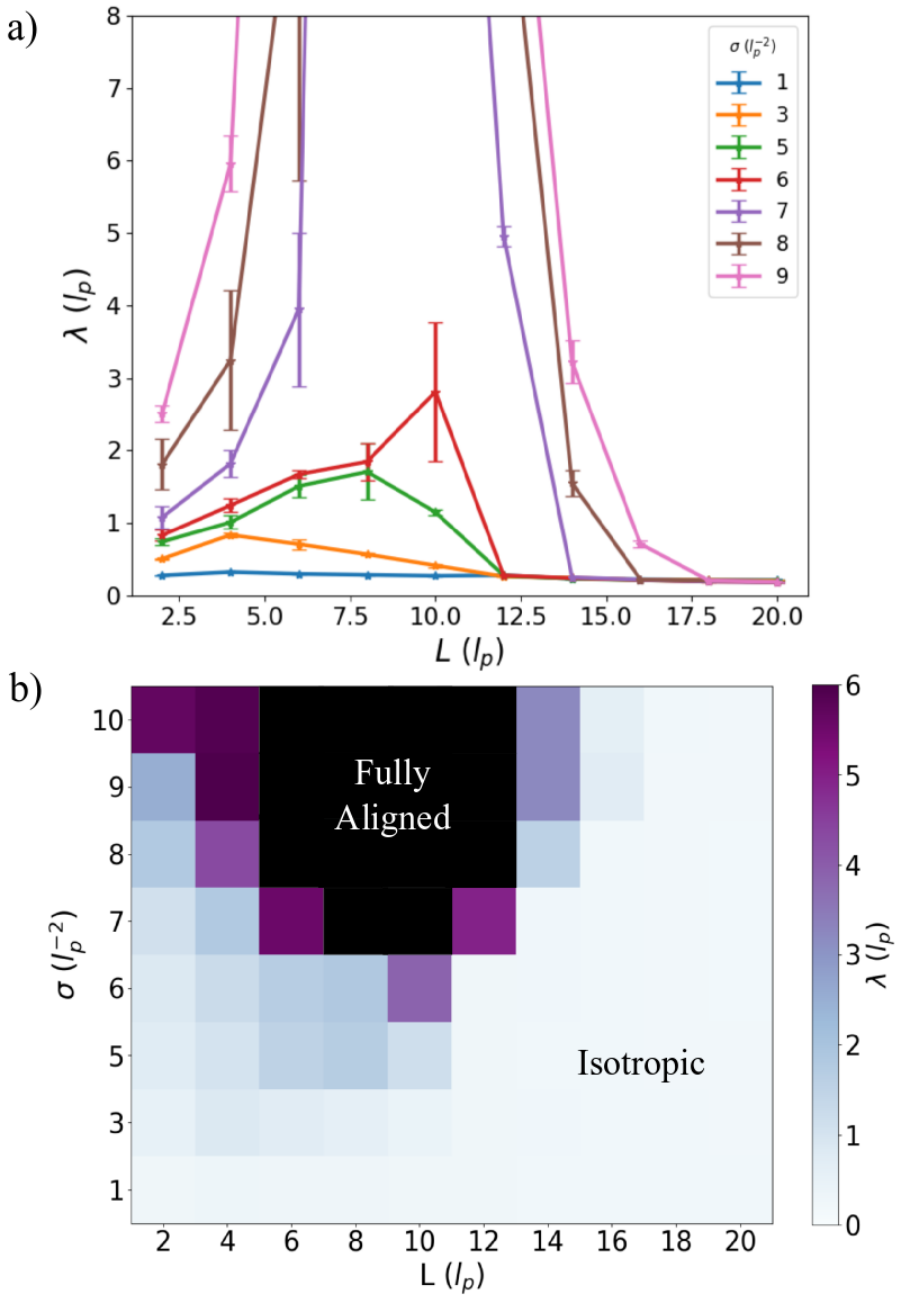

Figure 3.7: Plots of the two-dimensional alignment correlation length (λ) as a function of polymer length (L) and grafting density (σ). At low σ, the polymer forms independent clusters of locally aligned polymer strands, which is signified by the finite values of λ. At higher grafting densities, λ increases rapidly beyond the size of the simulation box for some ranges of L, indicating the sudden transition to a fully aligned phase. As the grafting density is increased further, this range of fully aligned polymer is expanded. At all grafting densities shown here, λ drops rapidly to zero at high enough L, indicating a transition to the isotropic phase due to increased chain conformation entropy.

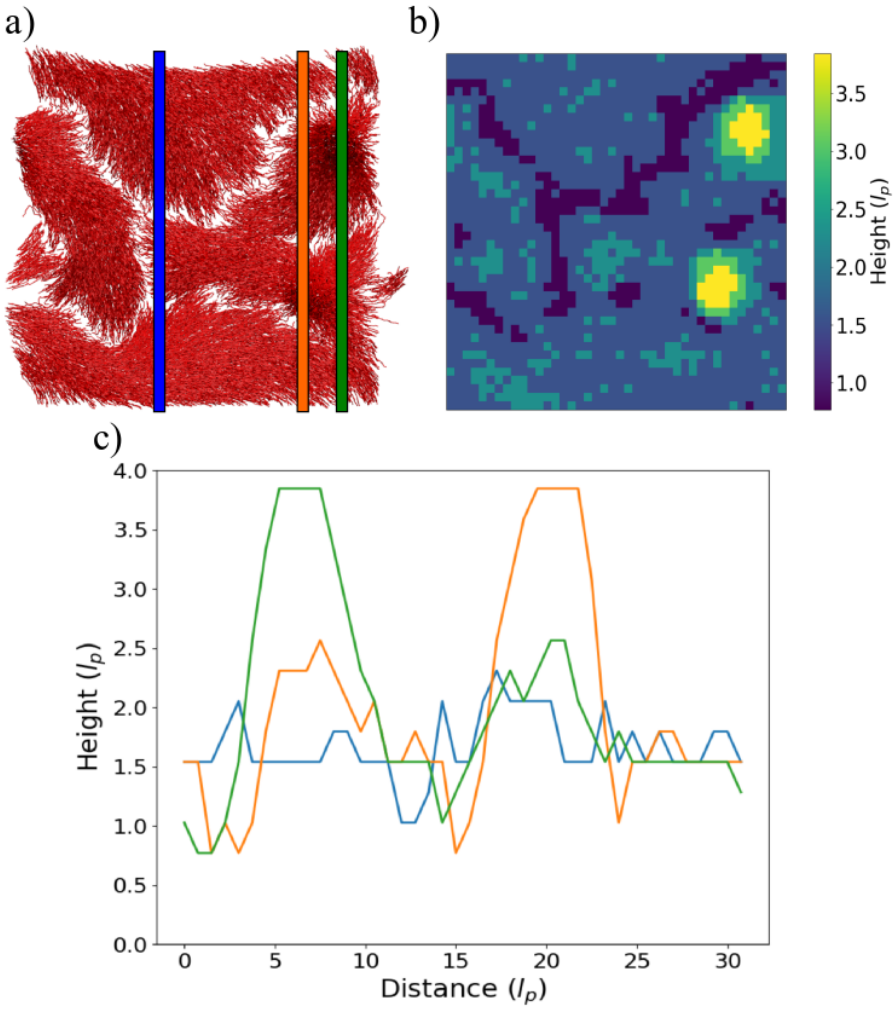

Figure 3.8: An AFM-style image of the topography of the nematically collapsed brush. **a)** The explicit chain morphology of the brush. Depending on how the chains are oriented, the brush may have a diversity of heights across the substrate. **b)** Heat map depicting brush height. **c)** Height as a function of y-coordinate position from different line slices. The line colors match the lines drawn on **a)**.

explanation for some of the dramatic morphologies - especially the columns with rounded tops - seen in experimental studies.[137]

3.5 Conclusion

We have used Monte Carlo polymer simulations to study the phase behavior of semiflexible polymer brushes that experience nematic interactions. It was found that such brushes experience different phase behavior than flexible brushes. Even without nematic interactions present, semiflexible brushes were found to lack access to many of the configurations available to their flexible counterparts. As grafting density was increased, brushes were forced more rapidly into the rigid, upright brush configuration, and finite extensibility effects became prominent. For these reasons, semiflexible brush heights were found to grow faster with grafting density than the one third power expected for flexible brushes. When nematic interactions were considered, the brush was found to experience a variety of different phases. In particular, at low grafting density and polymer length, the brush was found to form a semicrystalline structure with small clusters of aligned polymer segments. As the grafting density was increased, these clusters overlapped and the brush became homogeneously aligned throughout, forming a tilted configuration. Furthermore, as polymer length was increased beyond a certain point, the brush lost its tilted configuration and became completely isotropic, a result of the increased conformational entropy available to longer, more flexible chains that can more easily adopt twisted and bent configurations.

CHAPTER 4

POLYMERS GRAFTED ONTO CELLULOSE NANOCRYSTALS

4.1 Abstract

Cellulose nanocrystals have attracted interest as highly functionalizable nanomaterials that are also green and biodegradable. In this work, we perform a simulation study of block copolymer brushes and mixed brushes grafted onto the surface of a simple cellulose nanocrystal model. The morphology of the polymer brushes are examined under a variety of different solvent conditions, which can cause the different polymer components to alternately swell or collapse. Depending on the configuration of the polymer brush, the different solvents create dramatic changes in cluster formation atop the surface of the nanocrystal. Multi-component systems of nanocrystals are also examined by calculating the free energy as a function of separation distance and orientation between two cellulose nanocrystals for the different solvent-polymer systems. In addition to affecting the morphology, the solvent type and brush configuration also greatly affects the qualitative shape of the free energy curve. A more heavily coarse-grained model for cellulose nanocrystals is then used to examine the morphology of suspensions of cellulose nanocrystals based on the qualitative behavior of the pair potentials.

4.2 Introduction

Cellulose nanocrystals have recently attracted great interest as highly functionalizable nanomaterials that are low-cost, green, biodegradable, and do not rely on fossil fuels to produce.[39, 54, 95, 24] Possible applications of cellulose nanocrystals include uses in wastewater treatment, energy storage, and drug delivery.[131] Some of the most useful properties of cellulose nanocrystals come from their extensively functionalizable surface as well as their ability to

reinforce softer materials.[100, 71] For example, carboxylic acid or amine moieties can render cellulose nanocrystals pH-responsive.[141] In addition to these smaller moieties, polymers can also be grafted onto cellulose nanocrystals to enhance their properties.[152]

Polymer brushes have been used to functionalize a variety of surfaces for numerous applications.[55, 66] Many desirable surface effects can be achieved by tuning certain polymer physical parameters, such as grafting density and molecular weight.[2, 20, 76] Other effects can be obtained by altering the chemistry of the polymer itself, such as anti-fouling[18] and preferential wetting properties.[88, 38] Polymer brushes can also be highly stimuli-responsive, especially when the brush consists of more than one component.[129] Stimuli-responsive materials exhibit dramatic structural or morphological responses to external stimuli. For example, block copolymer brushes with top blocks that are heavily responsive to solvent conditions,[149] mixed brushes that undergo microphase separation and change wettability conditions when washed with different solvents,[35] and mixed copolymer brushes grafted onto nanoparticles that respond to different pH conditions[96] have all been synthesized.

Several theoretical studies have been performed examining the properties of stimuli-responsive polymer brushes on flat surfaces. In particular, Wang & Müller examined the morphological characteristics of diblock copolymer brushes and two-component mixed brushes under various solvent conditions.[138, 139] They found that, depending on the solvent conditions, a broad range of structures and morphologies could be formed, including lamella and cylinders. However, unlike more traditional block copolymer phases, these structures were not correlated over long length scales due to the constrained nature of the brush. In addition, these polymer brushes in solvent were shown to exhibit phases that have no straightforward correspondence to a bulk polymer, such as block copolymers that bend back upon themselves in order to keep the top block shielded from the solvent.

One can consider functionalizing the surface of cellulose nanocrystals with multicomponent polymers. Cellulose nanocrystals are high aspect ratio materials, so grafting polymers to them is not necessarily the same as grafting polymers to a flat surface. Past work has

examined both polymer films and polymers grafted on the surface of spheres[48, 17] which can be shown to create morphologies that are different from those that form on a flat surface due to the underlying curvature. Similarly, high aspect ratio nanorods can be expected to produce different morphologies from flat surfaces and even from one another, depending on the dimensions of the nanorod. Cellulose nanocrystals can vary dramatically in size and shape depending on the source of the cellulose. For example, cellulose nanocrystals derived from tunicin tend to have a diameter of around 10-12 nm, while those deriving from Avicel have much smaller diameters - around 4.5-5 nm.[40, 26, 24]

Of particular interest is what happens when more than one polymer-functionalized cellulose nanocrystal comes into contact with another. By altering polymer chemistry, temperature, or solvent effects, the energetics by which the cellulose nanocrystals interact can be changed dramatically, and can potentially be utilized to produce desirable effects, such as materials that change in stiffness,[25, 121] mechanical strength,[14, 15] provide adhesive properties,[23] or uptake water along percolation pathways.[16, 27] One can imagine many applications for such a system. For example, generating a highly percolative network out of swollen polymer grafted to cellulose nanocrystals could be used for water filtration, among other applications. In order to understand how such an assembly would behave, it is important to understand the interactions and morphology between pairs of cellulose nanocrystals.

In this study, a model system of multi-component polymers grafted onto cylindrical surfaces is examined as a representation of cellulose nanocrystals. The morphological behavior of both diblock copolymer brushes and mixed brushes grafted onto cellulose nanocrystals is studied in detail. In addition, the interactions between pairs of such nanocrystals are quantified, both as a function of distance as well as relative orientation under a variety of solvent conditions. These free energies are then used to parameterize simple interactions for a heavily coarse-grained model of cellulose nanocrystal suspensions in order to determine their qualitative morphological behavior in the bulk.

4.3 Model and Methods

In this work, the so-called virial model originally used by Wang & Müller to study brushes on flat surfaces is adapted for cellulose nanocrytals.[139, 138] Within this model, the polymers are described explicitly as bead-spring chains. The surface of the cellulose nanocrystal is described as a hard wall, while the cellulose nanocrystal itself is modeled as a cylinder. The solvent is described implicitly. Polymer-polymer interactions are described by effective potentials using a third-order expansion of the equation of state:

$$\frac{H_{nb}}{k_B T} = \int_V \sum_{\alpha,\beta} \frac{1}{2} \nu_{\alpha\beta} \hat{\rho}_\alpha(\mathbf{r}) \hat{\rho}_\beta(\mathbf{r}) + \sum_{\alpha,\beta,\gamma} \frac{1}{3} w_{\alpha\beta\gamma} \hat{\rho}_\alpha(\mathbf{r}) \hat{\rho}_\beta(\mathbf{r}) \hat{\rho}_\gamma(\mathbf{r}) d\mathbf{r} \tag{4.1}$$

Where $\hat{\rho}_K(\mathbf{r})$ represents the polymer chain density of components of type K, and the ν and w terms are second-order and third-order interaction coefficients, respectively. The polymers themselves are discretized into N beads ($N = 32$ in this work). From a theoretical perspective, the polymer chain density is often treated as delta function valued, where the delta functions are located on the contour of the polymer.[42] However, from a computational perspective, analyzing equilibrium properties for systems with delta function interactions is intractable, so regularizing the density with a smooth and finite valued function is often used instead. In previous studies using this model, the densities were regularized by meshing to a rectangular grid, which allows for computationally efficient calculations.[30, 111] However, since surfaces with high curvature are examined in this work, it is preferable not to use the grid-based regularization in order to avoid artifacts related to the orientation of the grid relative to the curved surface. Instead, the density is regularized by modeling each bead as a Gaussian density cloud. The polymer density can then be calculated from the bead positions

using the following:

$$\hat{\rho}_K(\mathbf{r}) = \sum_{i=1}^{n} \frac{\delta_{iK}}{N\left(2\pi\sigma^2\right)^{3/2}} \exp\left(-\frac{|\mathbf{r}-\mathbf{r}_i|^2}{2\sigma^2}\right) \tag{4.2}$$

Where σ is the standard deviation of the Gaussian distribution, and δ_{iK} is unity if bead i is of type K and zero otherwise. While the choice of σ is fairly arbitrary, it can be thought of as the parameter that controls how many beads another bead interacts with (in this work, $\sigma = 0.08\ R_e$). The factor of N in the denominator makes the average polymer density independent of the chain discretization. As $\sigma \to 0$ and $N \to \infty$ while keeping the number of interacting beads constant, the delta function interactions of the un-regularized model are recovered.

With the specified Gaussian density clouds, the nonbonded energy function can be transformed into a sum of two-body and three-body potentials, which can be used straightforwardly in simulations. Any term of the form:

$$u[\mathbf{r}] = \int_V \hat{\rho}_\alpha(\mathbf{r})\hat{\rho}_\beta(\mathbf{r})d\mathbf{r} \tag{4.3}$$

is transformed into the two-body potential:

$$u(\mathbf{r}^n) = \sum_{i}^{n}\sum_{j}^{n} \frac{\delta_{i\alpha}\delta_{j\beta}}{N^2\left(4\pi\sigma^2\right)^{3/2}} \exp\left(-\frac{|\mathbf{r}_{ij}|^2}{4\sigma^2}\right) \tag{4.4}$$

And any term of the form:

$$u[\mathbf{r}] = \int_V \hat{\rho}_\alpha(\mathbf{r})\hat{\rho}_\beta(\mathbf{r})\hat{\rho}_\gamma(\mathbf{r})d\mathbf{r} \tag{4.5}$$

is transformed into the three-body potential:

$$u(\mathbf{r}^n) = \sum_i^n \sum_j^n \sum_k^n \frac{\delta_{i\alpha}\delta_{j\beta}\delta_{k\gamma}}{N^3\left(2\sqrt{3}\pi\sigma^2\right)^3} \exp\left(-\frac{|\mathbf{r}_{ki}|^2 - \mathbf{r}_{ki}\cdot\mathbf{r}_{ji} + |\mathbf{r}_{ji}|^2}{3\sigma^2}\right) \tag{4.6}$$

4.3.1 Thermodynamic Integration

Free energies of cellulose nanocrystal pairs in different configurations are calculated using thermodynamic integration.[44] Two parameters are varied: cellulose nanocrystal separation distance, λ, and cellulose nanocrystal relative orientation, θ.

Free energy curves as a function of separation distance between cellulose nanocrystals, $F(\lambda)$, are calculated via the following:

$$F(\lambda) = \int \frac{\partial F(\lambda)}{\partial \lambda} d\lambda = \int \left\langle \frac{\partial U}{\partial \lambda} \right\rangle_\lambda d\lambda \tag{4.7}$$

Where we impose that

$$\lim_{\lambda\to\infty} F(\lambda) = 0$$

.

Three independent simulations are performed for each separation distance, λ. The thermodynamic average, $\langle \partial U/\partial\lambda \rangle_\lambda$ is then calculated numerically by evaluating the potential energy for the same system with the cellulose nanocrystals slightly further apart, U_+, and slightly closer together, U_-, by a distance of $\Delta\lambda$. The numerical derivative is then calculated via

$$\left\langle \frac{\partial U}{\partial \lambda} \right\rangle_\lambda \approx \left\langle \frac{U_+ - U_-}{\Delta\lambda} \right\rangle_\lambda \tag{4.8}$$

In this work, $\Delta\lambda$ is 0.1 $R_{e,0}$. Similarly, orientation dependence is calculated for different cellulose nanocrystal rotation angles while holding separation distance constant. $F(\theta)$ is calculated using the same method as $F(\lambda)$, but here $F(\theta = 0)$ is set to zero, the cellulose nanocrystals undergo a rotation of 90 degrees, and $\Delta\theta$ is 4.5 degrees.

4.3.2 Coarse-Grained Nanocrystal Suspension Model

Heavily coarse-grained simulations of systems of cellulose nanocrystal suspensions are performed by modeling each cellulose nanocrystal as 7 Lennard-Jones beads rigidly connected in a row. Systems consisting of 5000 such nanocrystals are annealed down to low temperature to represent a kinetically trapped state. Their configuration in this frozen, kinetically trapped state is based purely on their attractive and repulsive interactions, and should provide insight into how cellulose nanocrystals with similar interactions would behave. All simulations were performed using LAMMPS. Specific parameters for each interaction type are provided in the Appendix.

Cluster analysis on the suspension model was performed in several steps. First, each nanocrystal was represented as a point in an 8-dimensional space. The first three dimensions were the position coordinates of the center of mass of the nanocrystal. The other five dimensions were the independent elements of the Q-tensor defined by the orientation of the nanocrystal: $\mathbf{Q}_i = \mathbf{u}_i\mathbf{u}_i^T$. Using this representation for the nanocrystals ensured that if the Euclidean distance between two nanocrystals was small, then they were positioned near each other with similar orientations. Using the Q-tensor also ensures that the analysis treats orientations differing only by sign as identical ($\mathbf{u}_i$ is the same as $-\mathbf{u}_i$).

The size and number of individual clusters was determined using a Dirichlet process infinite mixture model, implemented in scikit-learn.[109] The infinite mixture model did not require a priori knowledge of the number of clusters in the system, so it provided a good option for this particular analysis.[45, 99]

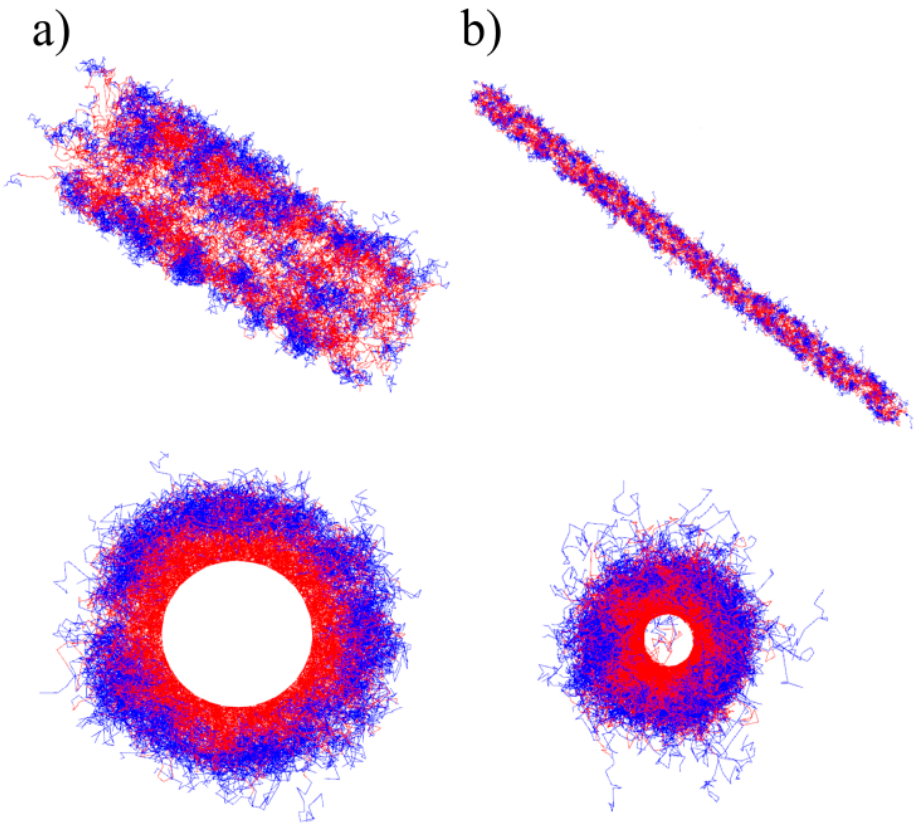

Figure 4.1: Comparison of the two nanorod styles examined in this work. **a)** Nanorod with diameter of approximately 30 nm and grafting density of something chains per nm^2. **b)** Nanorod of diameter of approximately 5 nm and grafting density of 0.3 chains per nm^2. Note that while the shapes and sizes of the nanorods differ, the chains themselves are the same size. Block copolymer chains shown here are under solvent BO.

4.4 Results

4.4.1 Solvent Effects

Parameters for the virial model are selected to implicitly reproduce effects of various solvent conditions for different polymer components (All parameters are provided in the Appendix). Of particular interest in the present study is the polymer morphology in the presence of a solvent that is good for one component but very poor for the other. Under such circumstances, one polymer component will swell considerably while the other will collapse to a much smaller size. In some solvents, the collapsed domain will become fully surrounded by

the swollen polymer, while in others the two polymer components will repel one another.

These solvent effects are important when polymers grafted onto adjacent cellulose nanocrystals come into close contact. Certain types of polymers will clump together and form a bridge-like structure between the two objects. In the case of a large collection of objects, these collapsed yet connected domains may form a percolating network.

We have analyzed four types of solvent in detail which can be characterized by how they affect the different polymer components: solvents A, B, C, and D. Solvent A acts as a good solvent for both components, causing each to swell and become extended beyond the sizes typically expected from an unperturbed polymer. Solvent B acts as a poor solvent for one of the components, causing it to collapse. In solvent B, the repulsive interactions between the two polymer components are still present, so that considerable separation of the components occurs. Solvent C differs from solvent B only in that the collapsing component is attracted to the swollen component, so it is favorable for the collapsed component to be fully surrounded by the other component. Solvent D acts as a poor solvent for both components, causing them both to collapse.

For solvents B and C, the interactions are asymmetric between the two components, and there is a substantial morphological difference in block copolymer brushes when the inner component collapses as compared to when the outer component collapses. To clarify which situation is being considered, we refer to the block copolymer brush solvents as solvent BI and CI when the inner component collapses, and BO and CO when the outer component collapses in all future notation. For mixed brushes, these distinctions are irrelevant as there is no inner and outer component, and the solvents are referred to simply as B and C.

4.4.2 Single CNC Systems

In this section, the morphology of block copolymer brushes and mixed brushes grafted onto cylindrical surfaces are examined qualitatively to gain an understanding of how these polymers behave under different solvent conditions. Two different sizes of cellulose nanocrystals

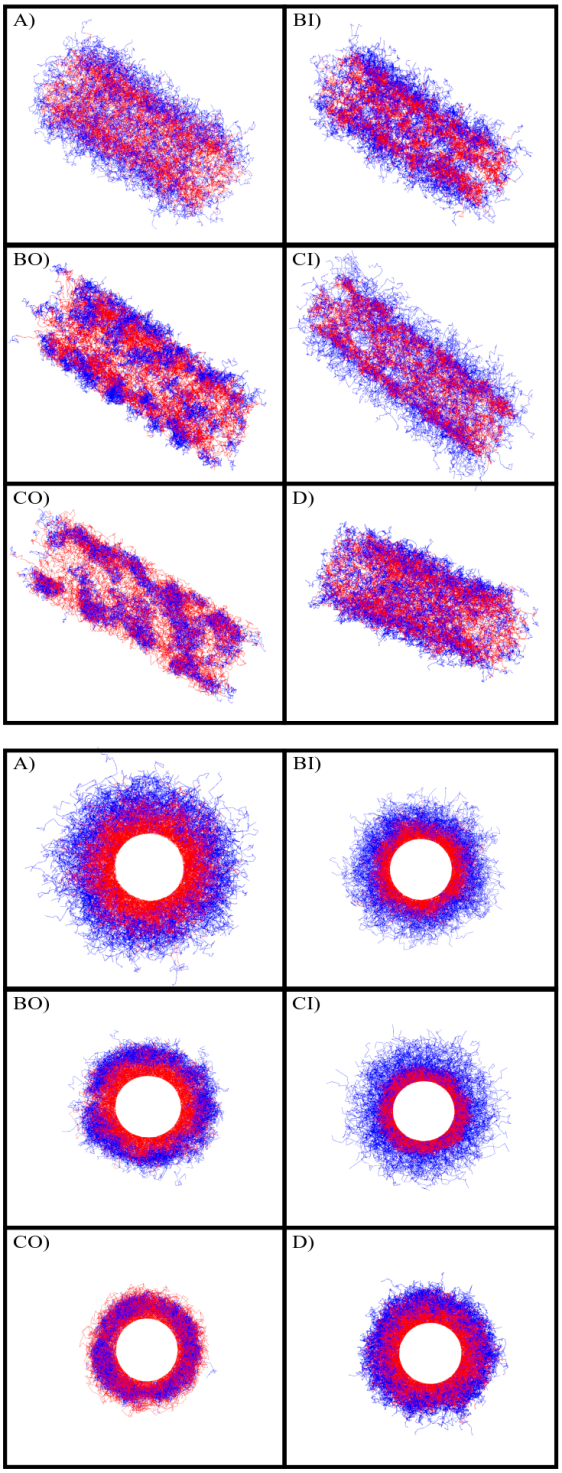

Figure 4.2: Side and end views of block copolymer brush morphologies under the different solvent conditions.

are examined. The first is representative of a nanorod with a diameter of approximately 15 nm, similar to that of a cellulose nanocrystal derived from tunicin, and with a length of 35 nm, and a grafting density of 0.3 chains / nm. The second is representative of a nanorod with a diameter of 5 nm, similar to a cellulose nanocrystal derived from wood, a length of 150 nm, and a grafting density of 0.3 chains / nm. An image of the two nanocrystals is shown in Figure 4.1. Figure 4.2 displays images of equilibrium morphologies for block copolymer brushes under the aforementioned solvent conditions for the wider cellulose nanocrystal size (narrow nanocrystal morphologies are displayed in Figure 4.3, and they are qualitatively similar).

As can be seen, the different solvent conditions create qualitative differences in the morphology. For solvent A, the block copolymer brush expands radially outward and no general ordered structure appears to form. Individual polymers are extended, so the polymer density gradually becomes more diffuse as the radial distance increases away from the surface of the nanocrystal. The stronger repulsion between the different blocks does not appear to have a strong qualitative effect on the morphology beyond causing the polymers to become further extended.

Solvent B, in comparison, does create clustering in the collapsed component. For BI, where the inner block collapses, this clustering occurs near the surface of the nanocrystal, while in BO the clustering occurs on top of the inner component. Since the interactions between polymer components are repulsive in solvent B, highly separated domains form. In BI, the collapsed domain forms clusters on the surface of the nanocrystal that expel the swollen component, which fills in the leftover void regions. In BO, the clusters of collapsed component lie on top of the swollen component, but they do not mix together.

In many ways, the solvent C morphologies look similar to those forming under solvent B, but the mutual attraction between the two block copolymer components creates important differences. For CI, the collapsed inner component spreads more evenly across the surface of the nanocrystal, as it is stabilized by the swollen outer component which mixes with

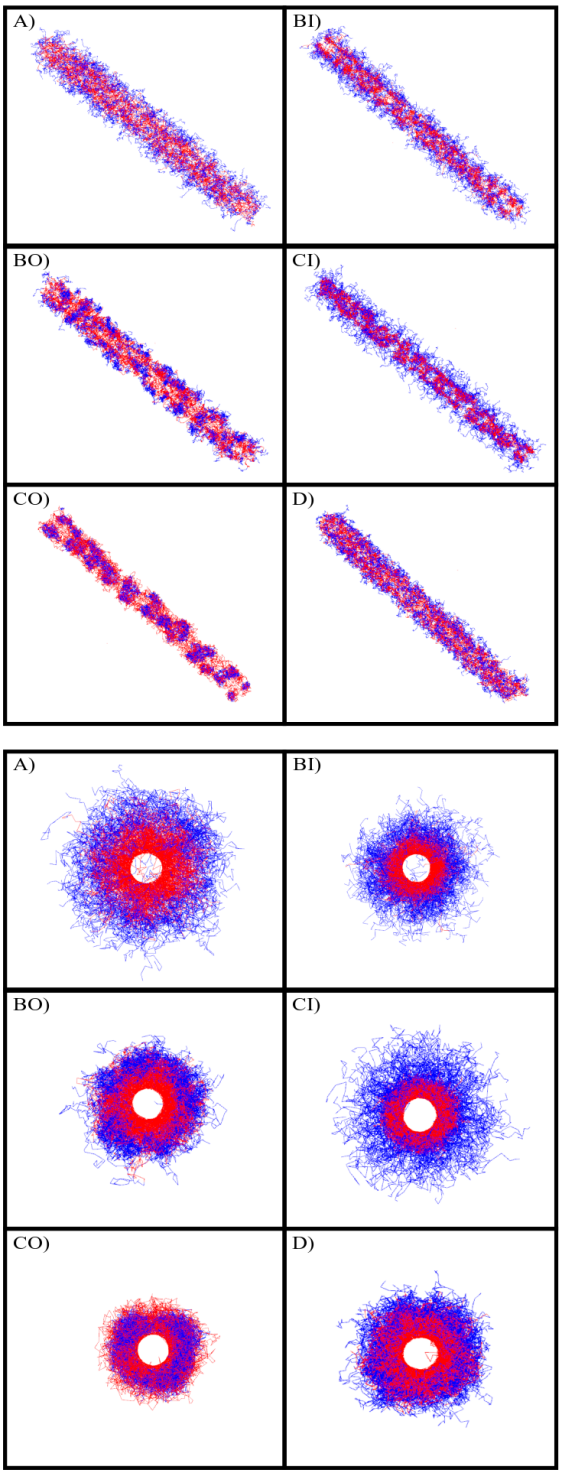

Figure 4.3: Side and end views of block copolymer brush morphologies under the different solvent conditions for the narrow cellulose nanocrystal.

it. The overall effect is to make a more uniformly coated nanocrystal rather than forming into the separated clusters as in BI. For CO, the collapsed outer domain falls into the inner component, making the morphology substantially different from BO. The collapsed component is able to form larger cluster sizes as it is also stabilized by the inner component.

Solvent D, where both domains collapse, is substantially shrunken compared to solvent A. In addition, the two components mix together so the polymer distribution is not as diffuse as in solvent A. Unlike solvents B and C, no clustered domains form. Instead, both blocks are evenly distributed around the nanocrystal.

Figure 4.4 displays qualitative images for mixed brush morphologies on the wider cellulose nanocrystal (The narrow nanocrystal is displayed in Figure 4.5). Solvent A with the mixed brush once again causes the polymers to become highly extended. Unlike the block copolymer brush, the mixed brush is able to undergo some level of lateral demixing between the two components into separated domains due to the stronger repulsion between unlike polymer components. However, these domains are not persistent and gradually fluctuate.

Solvent B and solvent C look similar to their BI and CI counterparts in the block copolymer brush: one of the polymer components collapses near the surface of the nanocrystal. However, the lack of connectivity between the different polymer components allows phase separation to occur more easily. In solvent B, the collapsed component segregates away from the swollen one near the surface leading to patches of both collapsed material and patches of extended material. In solvent C, these distinct patches do not form as the swollen component mixes in freely with the collapsed component, essentially shielding it from the surroundings.

For solvent D, both components are collapsed and the behavior is similar to that of the block copolymer brush. There is considerable mixing between the two components, unlike for solvent A where the two components tend to form separated fluctuating domains.

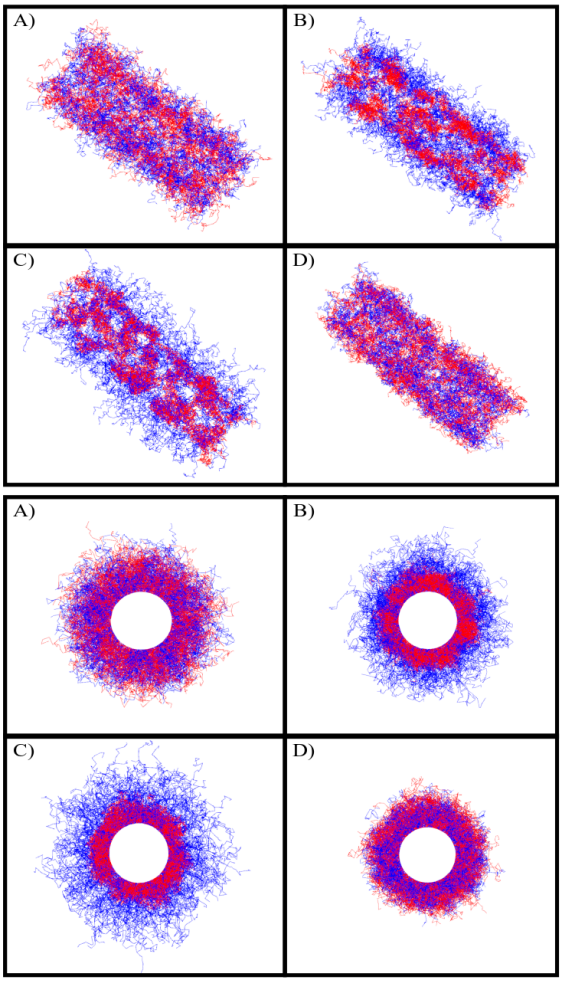

Figure 4.4: Side and end views of mixed brush morphologies under the different solvent conditions.

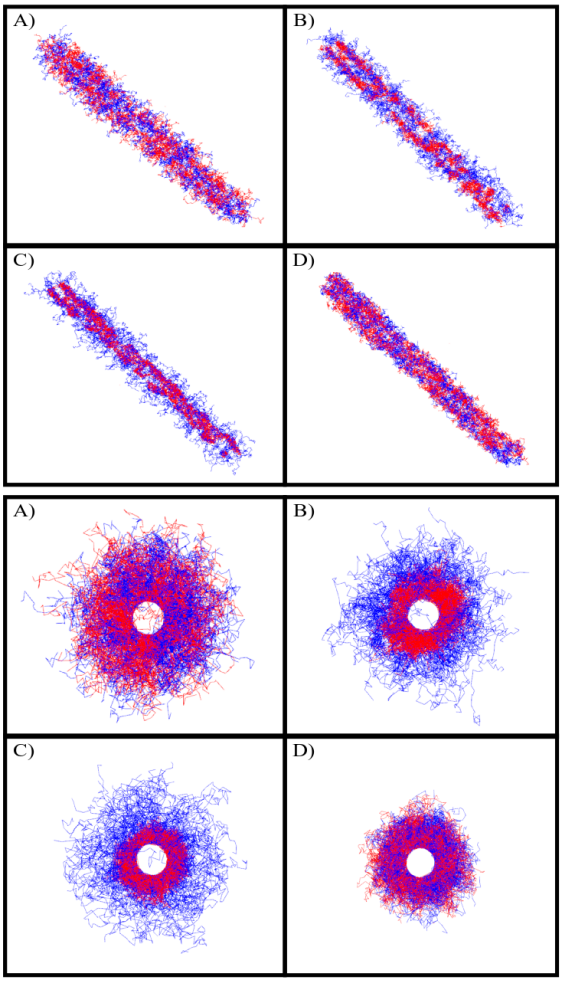

Figure 4.5: Side and end views of block copolymer brush morphologies under the different solvent conditions for the narrow cellulose nanocrystal.

4.4.3 Distance Dependence - Block Copolymer Brush

In large assemblies of nanocrystals, the effective interactions between nanocrystals caused by the grafted polymers can dictate how they interact with one another. Here, interactions between pairs of nanocrystals with grafted polymers are examined by using thermodynamic integration to calculate free energies of separation. Figure 4.6 displays free energies for block copolymer grafted cellulose nanocrystals under the different solvent conditions detailed earlier for the wider cellulose nanocrystal. As can be seen, the different solvents create substantial differences in the free energy curves.

The first free energy curve is for solvent A. Since the interaction is purely repulsive across all components, the free energy is also repulsive. The value of the free energy is near zero for distances greater than 5 $R_{e,0}$ at which point polymers from the two nanocrystals come into contact. It then steadily increases from there until it reaches the distance at which the nanocrystals come into contact.

The free energy curves for solvent BI and BO behave differently than solvent A due to the attractive interactions present in the collapsing component. The shape of the curve is dictated entirely by which order the blocks of the copolymer come into concact with each other as the separation distance decreases. For BI, the swollen blocks come into contact first, causing the interaction to be initially repulsive. As the nanocrystals come into closer proximity, the collapsed components are able to form "bridges" across the two cylindrical bodies. The additional interactions between the collapsed components is able to counteract the repulsion between swollen components as well as between swollen and collapsed components, causing the free energy to level off at the shortest distances. For BO, on the other hand, it is the collapsed components which initially come into contact. As can be seen in Figure 4.6, the free energy curve for BO decreases slightly as the nanocrystals come into contact before increasing again as the swollen components start to come into contact. At the shortest distances, the free energy curve for BO increases above the free energy at full separation.

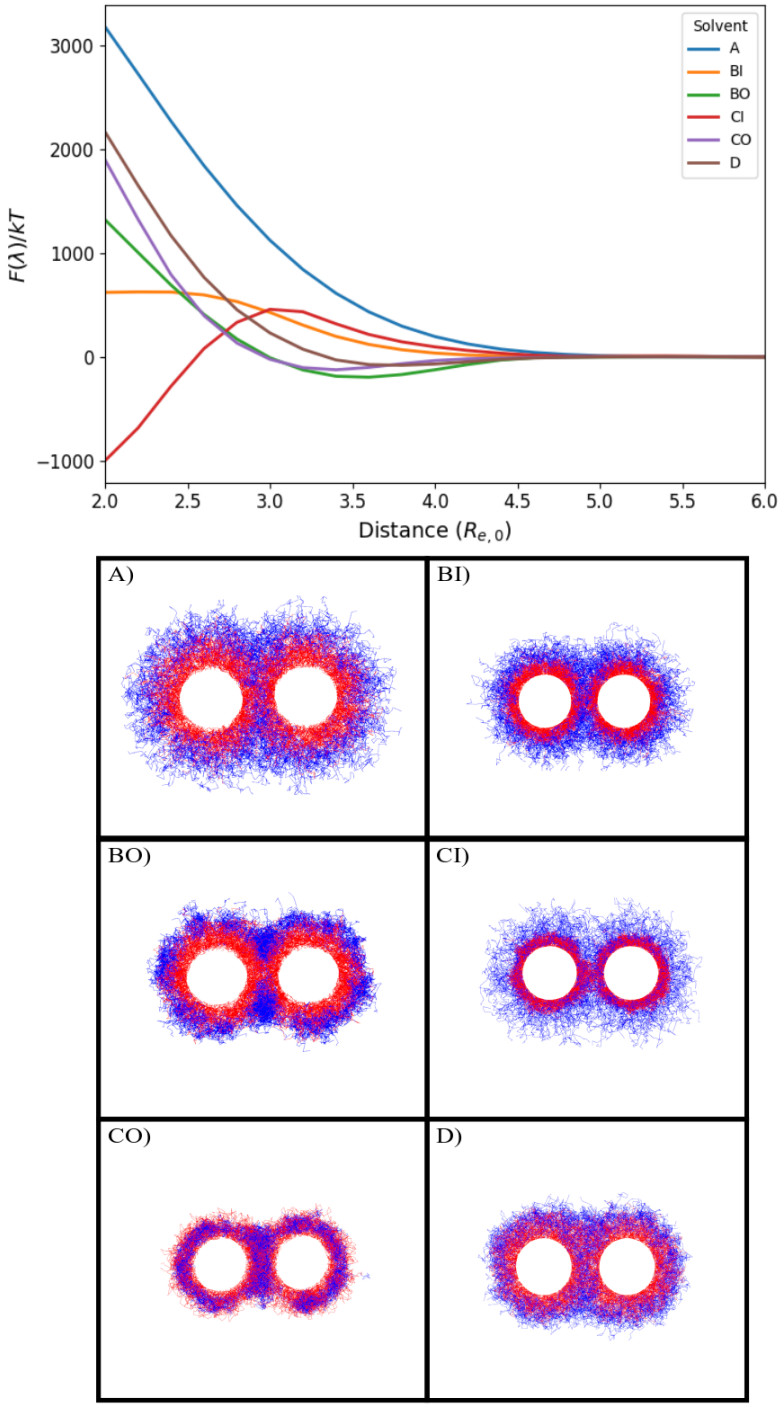

Figure 4.6: Pair potentials of block copolymer brushes under various solvent conditions along with corresponding side views of cellulose nanocrystal pairs. Interactions among polymers on the different nanocrystals dictates the shape of the free energy curve. The free energy curve shapes can be divided into roughly three types: purely repulsive (A), attractive at intermediate ranges and repulsive at short ranges (BO,CO,D), and repulsive at intermediate distances and attractive at short ranges (BI,CI).

Solvent CI and CO are similar to their BI and BO counterparts. The free energy curve for CI initially increases as the swollen components first come into contact and then decreases when the nanocrystals are close enough for the collapsed components to come into contact. However, unlike BI, the interaction between swollen and collapsed components is also attractive, which stabilizes the nanocrystals at short distances. In fact, the decrease in energy associated with mixing the unlike components makes solvent CI the only one with a free energy curve that is below zero when the nanocrystals come into contact. Solvent CO behaves nearly identically to solvent BO. As can be seen in Figures 4.2 and 4.6, the outer component collapses into the inner component for solvent CO, which makes the size of the polymer smaller than that of BO, and also makes the distance at which the free energy starts to decrease slightly smaller. In addition, the polymer in solvent CO is more densely packed together than BO, so at the shortest distances, the repulsion is stronger for CO, as indicated by the higher energy when the nanocrystals come into contact.

Finally, solvent D behaves qualitatively similar to solvents BO and CO. When the polymers on the two nanocrystals first come into contact, the energy decreases because of the attractive forces among all components. However, as for CO, the density of a single block is already fairly high, so the free energy begins to increase as the nanocrystals are forced into closer proximity until reaching the point when they come into contact.

4.4.4 Distance Dependence - Mixed Brush

Figure 4.7 displays free energy pair potentials for mixed brushes grafted onto the wider nanocrystals under solvent conditions A, B, C, and D. As can be seen from the plots, the mixed brush configuration does create some slightly different effects when compared to the block copolymer brush under the same solvents.

Solvent A for the mixed brush, which is purely repulsive, behaves nearly identically to solvent A for the block copolymer brush, and approaches nearly the same value of the free energy at contact of the nanocrystals. The lack of difference between different brush types

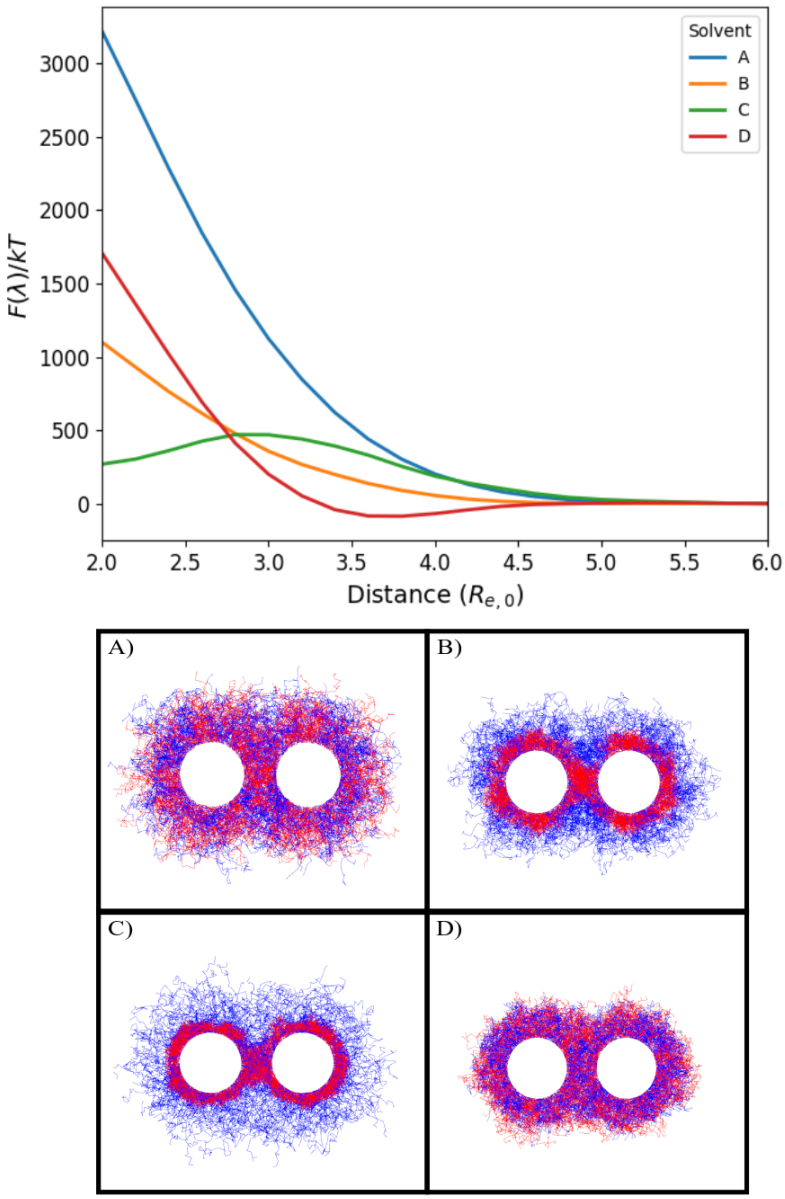

Figure 4.7: Pair potentials of mixed brushes under various solvent conditions along with corresponding side views of cellulose nanocrystal pairs. While solvents A and D behave similarly to their block copolymer brush counterparts, the greater extension of the swollen block in solvents B and C on the mixed brush causes the attractive regime to be weaker relative to the block copolymer brush.

can be attributed to the fact that the polymers in both cases are highly extended, and bringing the nanocrystals closer together does not cause any morphological changes in the material.

Both the free energy curve and image for solvent B look similar to those of solvent BI for the block copolymer. The collapsed component tends to cluster near the surface of the nanocrystal, while the swollen component extends far beyond it. However, since the separate components are unconnected in the mixed brush, both the collapsed and swollen components form larger clusters than in the block copolymer brush. For the collapsed component, the clusters are more irregularly shaped and are able to extend to a greater distance away from the surface. For the swollen component, the polymers are able to reach the same extention as those in solvent A, which is very different from the block copolymer brush. The increased repulsion from these fully extended swollen polymers prevent the free energy curve for the mixed brush from leveling off to the same extent as the block copolymer brush under solvent BI when the nanocrystals come into contact.

The attractive interactions between unlike components in solvent C causes the collapsed component to coat the nanocrystal much more uniformly than in solvent B. This can be seen by the more evenly and circularly distributed collapsed component in Figure 4.7. Similar to solvent CI relative to BI for the block copolymer brush, solvent C stabilizes the energy at short nanocrystal distances more than solvent B due to the attractive interactions between the unlike components, which actually causes the energy to decrease at the shortest distances before the nanocrystals come into contact. However, unlike the block copolymer brush, the increased extension of the swollen component in the mixed brush prevents the free energy from going below zero at contact.

Solvent D behaves nearly identically to solvent D with the block copolymer brush. When the polymers first come into contact, the free energy decreases due to the attractive interactions. However, as the nanocrystals come into closer contact, the high polymer density causes the free energy to rise sharply until the nanocrystals come into contact. Unlike for the block

copolymer brush, solvent D for the mixed brush is the only solvent that produces a distinct minimum in the free energy curve at an intermediate distance of nanocrystal separation.

Figure 4.8 displays free energy curves for the block copolymer brush (**a**) and the mixed brush (**b**) grafted onto the narrower cellulose nanocrystal. Qualitatively, the free energy curves follow the same patterns as those of the wider cellulose nanocrystal. The brush and solvent combinations that lead to collapsed components coming into contact first have an attractive intermediate region and a highly repulsive region at close contact, while the opposite effect is present when swollen components come into contact first. Slight differences between the narrow and wide cellulose nanocrystal types are present in the magnitude of these energetic effects. Specifically, the repulsive effects for solvents BI, BO, CO, and D in the block copolymer brush (B, C, and D for the mixed brush) are more subdued on the narrow nanocrystal relative to the wider nanocrystal; the free energy at the most repulsive point is less relative to the most attracive point than it is in the wider nanocrystal. This result is likely due to the swollen polymer components having more freedom to move around on the narrow nanocrystal due to the increased curvature. When the nanocrystals come into close contact, the swollen components are able to bend away from the point of contact and allow the collapsed components to come into contact, while on the wider nanocrystals, the swollen components become pinned between the nanocrystals due to the relatively low curvature.

4.4.5 Orientation Dependence

Although separation distance between polymer-grafted cellulose nanocrystals is expected to play the most prominent role in interactions, relative orientation is also important as it dictates how cellulose nanocrystals prefer to align near each other, and can have enormous consequences on how they behave in the bulk.

Free energy as a function of relative orientation between cellulose nanocrystals is shown for both brush types and all solvent conditions in Figure 4.9 for the wider cellulose nanocrys-

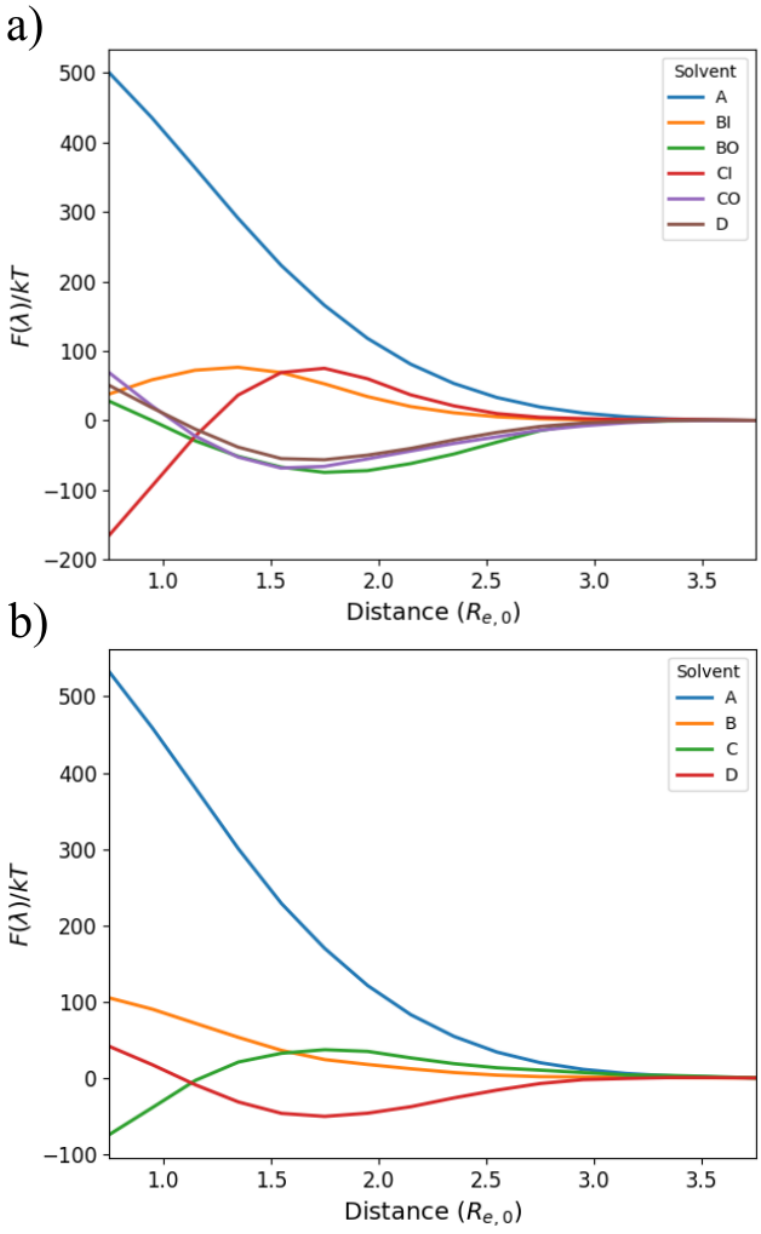

Figure 4.8: Free energy curves for the thinner (5 nm diameter) nanorod system for both **a)** block copolymer brush and **b)** mixed brush. Even though it contains a different nanorod radius and grafting density, this system shows similar qualitative free energy behavior to the wider nanorod free energy curves shown in Figures 4.2 and 4.4.

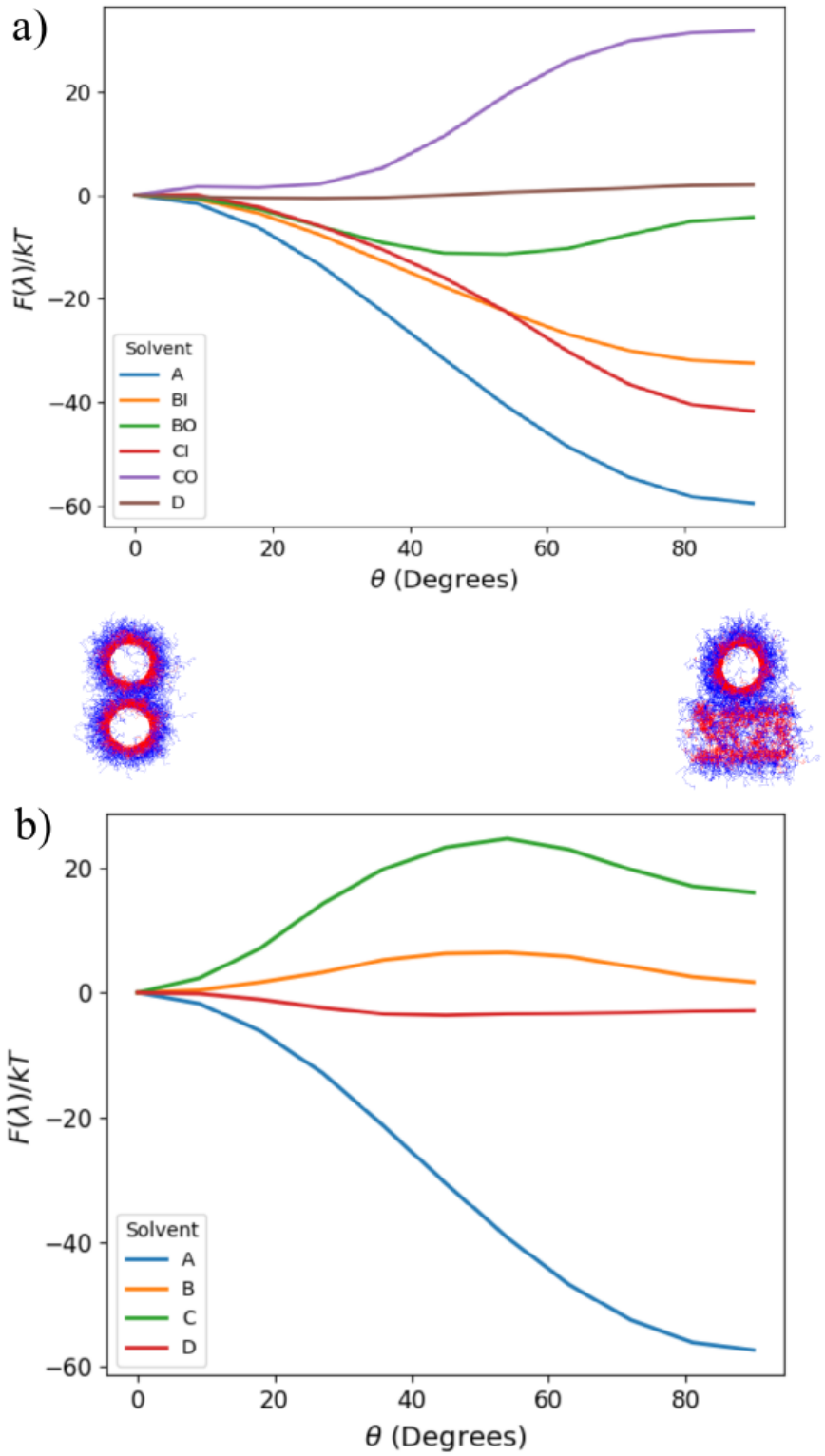

Figure 4.9: Free energies as a function of rotation angle for the different solvent conditions. **a)** displays free energies for the block copolymer brush while **b)** shows them for the mixed brush.

tal. The separation distance for these free energy curves is set at 3.3 R_e. At this distance, all cellulose nanocrystals under all solvent conditions are interacting in some way, which allows for a rich diversity of orientation dependencies.

From Figure 4.9a, it can be seen that the for several of the solvent conditions, free energy change as a function of rotation angle largely depends on how much of the nanocrystals are overlapping, particularly for solvents A, BI, and CI. Only the swollen components of the block copolymer brush are in contact in these solvents, while the collapsed domains are entirely unaffected by the rotation. Since the swollen component does not adapt its shape substantially based on the amount of contact, the free energy curve takes on a smooth sinusoidal profile in these solvents. Additionally, these three solvent types can be seen to have a positive free energy at 3.3 R_e, which explains why the free energy decreases as θ approaches 90 degrees. In contrast, the collapsed components of the cellulose nanocrystals are in contact in solvents BO, CO, and D. Unlike the swollen components, the collapsed components can deform quite substantially as the cellulose nanocrystal is rotated in order to maximize contact. The effect of this deformation is remarkably prominent in solvent BO which does not follow the simple sinusoidal pattern. Instead, the pattern is more complex, displaying local minima at approximately 50 and 130 degrees, while displaying a local maximum at 90 degrees. This unusual pattern is the result of how the collapsed domain restructures itself so as to maximize contact across cellulose nanocrystals. Near the minima, the outer block is able to increase its contact, while near the maximum the amount of contact rapidly decreases as the cellulose nanocrystals become perpendicular. These results are likely exaggerated due to the short cellulose nanocrystals used for these simulations. The free energy curves for solvents CO and D are simpler and smoother, as the morphological changes are less drastic; the collapsed components vary more smoothly because they are denser than in solvent BO.

Figure 4.9b displays the free energy as a function of rotation for the mixed brush in the different solvent conditions. While the mixed brush behaves identically to the block copolymer brush under solvent A and similarly under solvent D, there are substantial differences

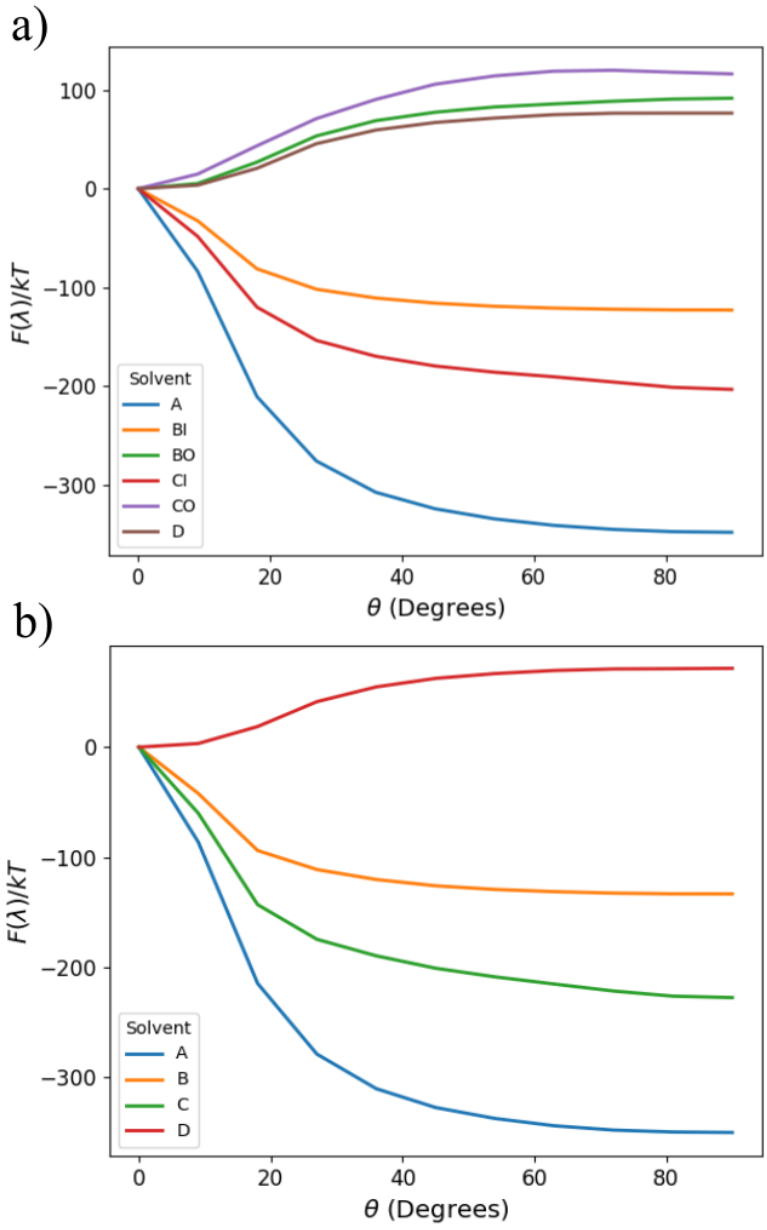

Figure 4.10: Free energy curves for the thinner (5 nm diameter) nanorod system for both **a)** block copolymer brush and **b)** mixed brush. Even though it contains a different nanorod radius and grafting density, this system shows similar qualitative free energy behavior to the wider nanorod free energy curves shown in Figures 4.9a and 4.9b

with the other solvents. In particular, the collapsed components in solvents B and C are in contact across both cellulose nanocrystals, which leads to large morphological rearrangements throughout the rotation. This effect is pronounced in solvent C, where the free energy increases as the cellulose nanocrystal moves to an orthogonal configuration, even though the free energy is greater than zero according to Figure 4.7. As the nanocrystal rotates, the connection between the collapsed components begins to break off, leading to an increase in the free energy. As the rotation angle approaches 90 degrees, the morphology begins to stabilize as the polymers are less stretched, leading to a very slight decrease in the free energy. A similar pattern also emerges in solvent B, although without as large of a free energy change.

Figure 4.10 displays the free energy of rotation for the block copolymer brush (**a**) and the mixed brush (**b**) grafted onto the narrower cellulose nanocrystal, all at a separation distance of 1.95 R_e. There are several pronounced differences between the wider and narrower cellulose nanocrystal free energy curves. The narrower nanocrystal has a much higher aspect ratio than the wider one, so the free energy changes more rapidly under rotation. This can be seen in the sudden increase or decrease in the energy as the angle increases before quickly leveling out at around 40 degrees. The free energy value at which the curve levels off depends entirely on the energy at that separation distance; repulsive interactions lead to a lower free energy as the nanocrystals twist away while attractive interactions lead to a higher free energy. Additionally, there is less disparity in the qualitative behavior of the free energy curves. All the curves follow the exact same trend, and there does not appear to be the minima or maxima at intermediate values as occurs in the wider nanocrystals due to the effect of the smaller surace area. Since the narrow nanocrystal has such a high aspect ratio, any possible local maxima or minima would be constrained to very small regions.

In order to further examine the orientation dependence in some of the more complicated solvent conditions, additional free energy calculations were performed at different separation distances for the wider cellulose nanocrystal. Figure 4.11 displays free energy curves for solvents BO, CO, and D at several separation distances to capture their behavior in the

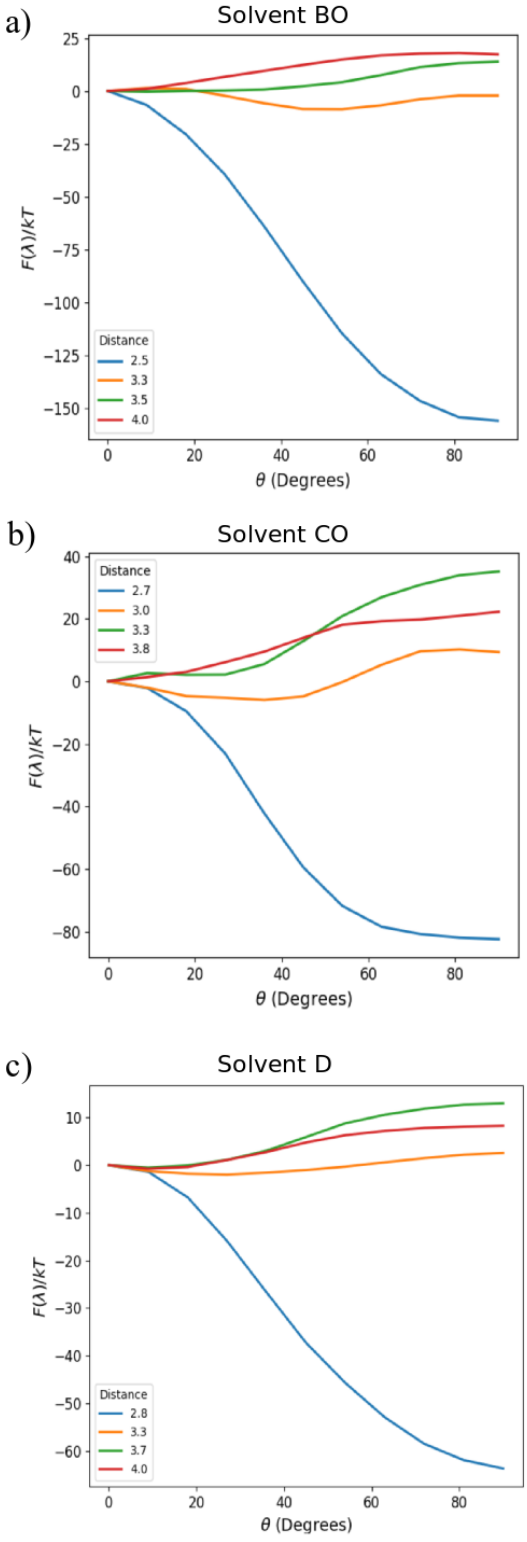

Figure 4.11: Free energies as a function of rotation angle at different cellulose nanocrystal separation distances for block copoymer brushes. **a)** displays free energies under solvent BO, **b)** is under solvent CO, and **c)** is under solvent D.

close-range repulsive regime as well as the long-range attractive regime. The simplest result that can be taken from these free energy curves is that at close-range in the repulsive regime, the orientation dependence is nearly identical to the behavior under solvent A in that it takes on a nearly sinusoidal shape. The interactions are slightly more complex within the attractive regime and depend more on the solvent type under consideration. For example, for solvent BO (shown in Figure 4.11a), there is a minimum free energy at around 50 degrees when the separation distance is 3.3 R_e. However, when this separation distance increases slightly to 3.5 and 4.0 R_e, this local minimum disappears, leaving the global minimum energy at 0 degrees. Similarly, for solvent CO (Figure 4.11b), a minimum free energy appears at around 45 degrees at a distance of 3.0 R_e before disappearing at greater distances. These shifts in minima can likely be attributed to the morphology changes that the collapsed outer component undergoes at different separation distances and orientations. When in closer contact, the collapsed domains can form greater bridges across nanocrystals which yields more complex orientational behavior than when the nanocrystals are further apart and the swollen domains are primarily in contact. In comparison to solvents BO and CO, solvent D (Figure 4.11c) is more homogeneous as both domains are collapsed. As a result, the orientation dependence at all separation distances are smoother and less complex for solvent D than the others, and similar to the repulsive regimes, these curves appear to be simple sinusoids with amplitudes dependent on the free energy at the given separation distance, as depicted in Figure 4.6.

4.4.6 Volume Effects at Contact

For some applications, such as water uptake in a hydrophobic polymer matrix, water must travel along the hydrophilic cellulose nanocrystals.[16, 27] Under such conditions, it is important that the cellulose nanocrystals are in contact with one another and form a percolating network throughout the polymer matrix. To enhance this process, block copolymers may be grafted onto cellulose nanocrystals, where the inner polymer component is hydrophilic as

well and would thus become swollen. The free energy curves calculated in the previous sections would have a strong effect on how the nanocrystals would orient relative to one another and their percolative behavior. Furthermore, how the swollen component behaves when two nanocrystals come into close contact would also dictate how easily water could move between adjacent nanocrystals. This section examines how grafted swollen polymer chains behave upon contact of cellulose nanocrystals in order to further characterize how they behave in the bulk. Specifically, the two block copolymer solvent types leading to swollen inner components (solvents BO and CO) are examined to determine how the volume of the swollen component changes as a function of separation distance for the narrow cellulose nanocrystal type. Additionally, the number of contacts between polymers of adjacent nanocrystals were determined.

Figure 4.12 displays both the volume and the number of contacts as a function of separation distance. Volumes were calculated by representing each bead as a sphere of 0.16 R_e radius. Polymer-occupied volume was calculated from the union of these spheres by using random Monte Carlo sampling. Similarly, contacts were calculated by the number of swollen polymer beads that were within 0.16 R_e of a swollen polymer bead from the opposite cellulose nanocrystal. As indicated by Figure 4.12, the volume taken up by the swollen polymer component decreases as the two cellulose nanocrystals come into contact, while the number of contacts between polymers on opposite cellulose nanocrystals increases. For solvent CO, there appears to be a very slight increase to the volume when the cellulose nanocrystals first come into contact. This effect is likely due to the attractive interactions in the outer collapsed components which first come into contact, and then cause the inner component to stretch slightly in order to increase the contact.

4.4.7 Large-Scale Nanocrystal Suspension Simulations

Continuing on from the previous section's discussion of percolating pathways, this section examines bulk systems of cellulose nanocrystals. Simulations of a highly coarse-grained model

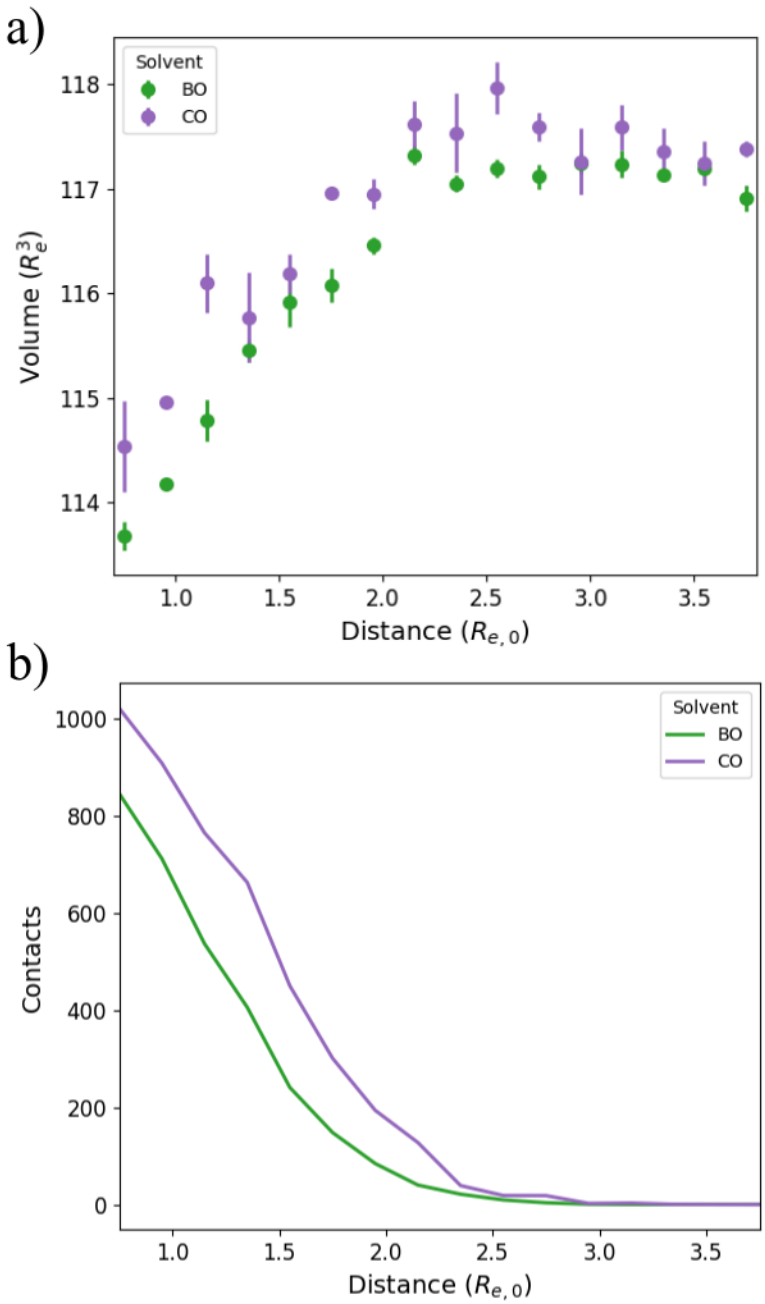

Figure 4.12: Plots of **a)** the volume occupied by the swollen component of the polymer and **b)** the number polymer components in contact with polymers of the adjacent cellulose nanocrystal as a function of the separation distance between cellulose nanocrystals. Both plots follow the same trends as the volume appears to decrease immediately as soon as the contacts between the cellulose nanocrystals begin to increase.

of cellulose nanocrystal suspensions were performed to understand their collective behavior under the different solvent conditions described previously. Using a highly coarsened perspective, all of the different cellulose nanocrystal conditions were lumped into three groups representing their overall interaction. These interactions were designed to roughly reproduce the qualitative effects of the different solvents by making the nanocrystals either purely repulsive (as in Solvent A), making them have a minimum energy in a parallel aligned configuration (as in Solvent D), or making them have a minimum energy in a crossed configuration (as in Solvent BO).

Suspensions of 5000 cellulose nanocrystals were prepared by annealing the system at high temperature and then cooling down to a temperature of zero to resemble a non-thermalized kinetically trapped state. Figure 4.13 displays morphologies for the three interactions types. In all cases, simulations were performed in both constant pressure (left panels) and constant volume (right panels) boxes. The constant pressure simulation provides a configuration that locally mininimizes the system energy without providing any void regions, while the constant volume simulation introduces void regions.

Figures 4.13a and 4.13b (red) display morphologies for the parallel-aligning cellulose nanocrystals. As can be seen, in both cases a strongly semicrystalline state forms. The nanocrystals not only align together in the same direction, but also stack together by matching endpoints. Local clusters of aligned and stacked nanocrystals form and produce different regions which meet at grain boundaries. The differences between the constant volume and constant pressure simulations are not great. Even though void regions form in the constant volume simulation, the semicrystalline behavior is still present, while there is more room for the clusters to align.

Figures 4.13c and 4.13d (blue) display morphologies for the purely repulsive cellulose nanocrystals. Unlike the parallel-aligning cellulose nanocrystals, these depend on whether the simulation is constant volume or constant pressure. For the constant volume simulation, the nanocrystals can be seen to fill the box and are heavily disordered. They have no propen-

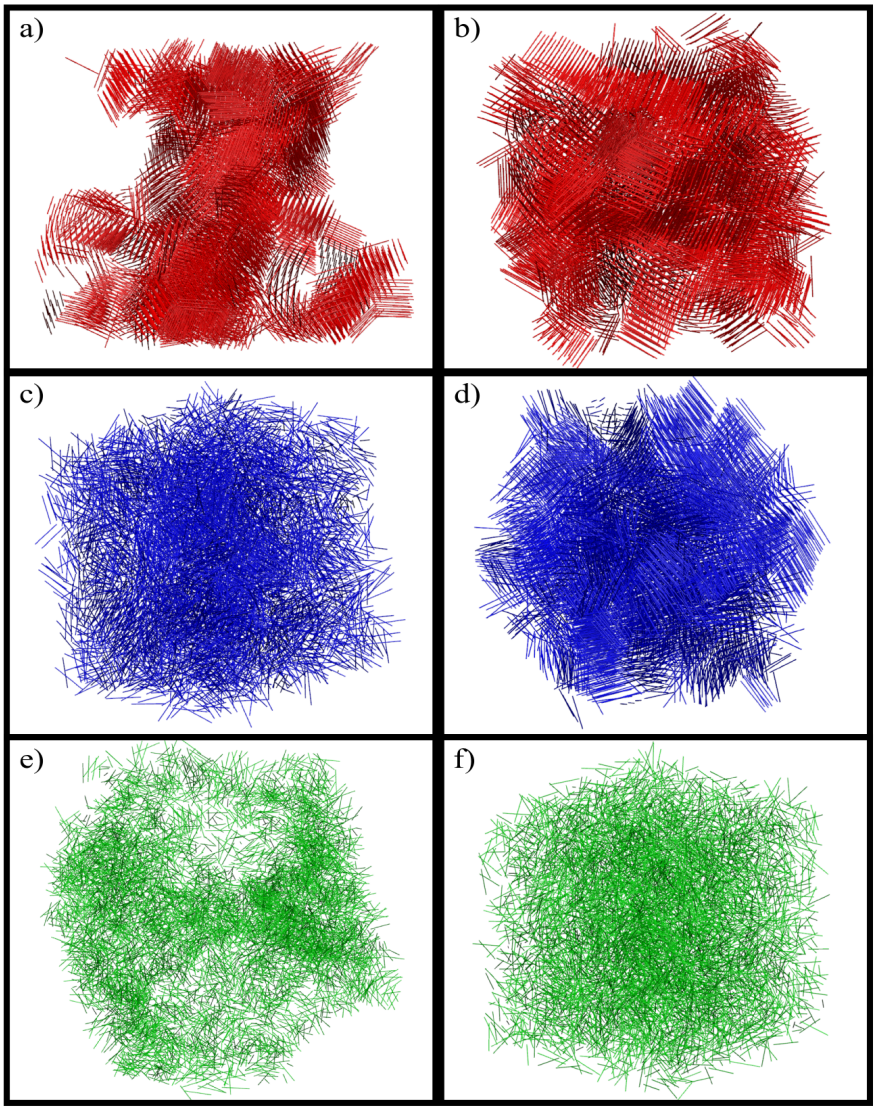

Figure 4.13: Morphologies of cellulose nanocrystal suspensions. Red denotes nanocrystals with a tendency to align parallel to one another. Blue denotes nanocrystals that are purely repulsive, and do not have any innate tendency to condense. Green denotes nanocrystals with a tendency to form a crossed "X-shaped" configuration. **a**, **c**, and **e** were cooled in a box of constant volume, allowing void regions to form. **b**, **d**, and **f** were cooled in a box of constant pressure, providing a configuration that locally minimizes the energy.

sity to align in any fashion and there is a general lack of order, which is to be expected from a system with no attractive interactions. The constant pressure simulation, however, is more similar to the parallel-aligning cellulose nanocrystals. The excluded volume interactions force the nanocrystals into an aligned and stacked state, similar to the semicrystalline state seen in the parallel-aligned nanocrystals. However, the grain boundaries between the individual clusters do not appear to be as sharp, likely due to the lack of attractive interactions holding them in place.

Figures 4.13e and 4.13f (green) display morphologies for the cross-forming cellulose nanocrystals. As can be seen, the tendency to avoid aligning disrupts the formation of any sort of crystalline or semicrystalline phase leading to entirely disordered morphologies under both constant volume and constant pressure simulations. Superficially, the morphology resulting from the constant pressure simulation looks similar to the morphology of the fully repulsive nanocrystal following a constant volume simulation. However, upon inspecting the trajectories, the cross-forming nanocrystals are far more kinetically stuck due to their attractive interactions. The constant volume simulation is similar to the constant pressure in that a disordered morphology forms. However, there are significant void regions that form surrounding the frozen disordered structures.

Clustering analysis was performed on constant pressure parallel-aligning and purely repulsive CNCs. Results are displayed in Figure 4.14. As can be seen in Figure 4.14b, the individual clusters tend to stack up into layers of closely connected nanocrysals which then meet at sharp grain boundaries. On average, the purely repulsive cellulose nanocrystals tend to form a greater number of clusters than the aligning cellulose nanocrystals: 98 clusters for the aligning nanocrystals and 184 for the purely repulsive. This result is expected, as the repulsive nanocrystals are more loosely held in the system, creating more disorder in the morphology and preventing large clusters from forming. In addition, the distribution of nanocrystals belonging to a cluster of a given size is shown in Figure 4.14c. In general, the repulsive nanocrystals provide a smoother distribution, with a greater concentration at the

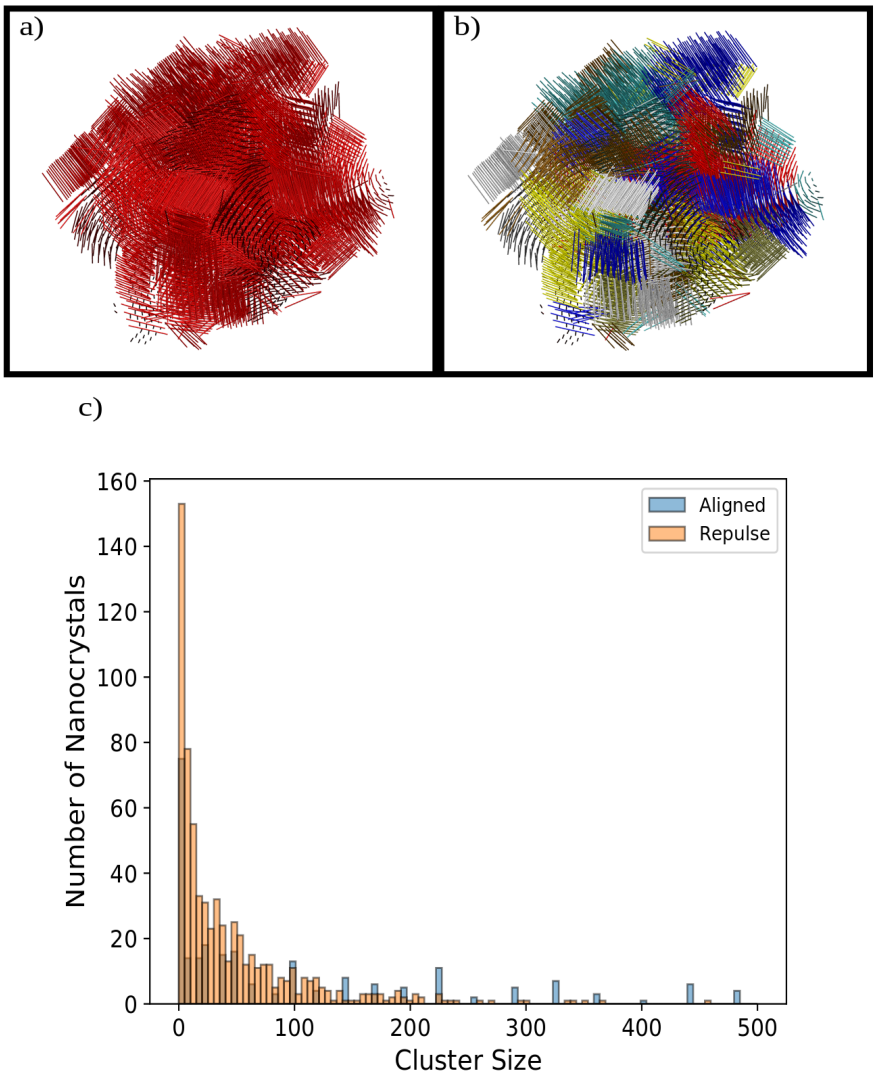

Figure 4.14: Clustering analysis of the aligning and repulsive cellulose nanocrystal suspensions. **a)** displays the bare morphology before clustering, while **b)** color-codes each nanocrystal by its corresponding cluster. **c)** provides a distribution showing the likelihood of a cellulose nanocrystal belonging to a cluster of a given size. In general, the aligning cellulose nanocrystals tend to form larger clusters with a distribution that is more spread out. In comparison, the repulsive cellulose nanocrystals are more concentrated toward smaller cluster sizes. These distributions reflect the average number of clusters for each type: 98 for the aligning and 184 for the repulsive.

smaller cluster sizes that smoothly drops down as the cluster sizes get larger. In contrast, the aligning nanocrystals has a distribution that is more evenly spread. Even at large cluster sizes, up to around 500, there are a substantial number of nanocrystals. The aligning nanocrystals hold clusters in place more easily, so it is again expected to have clusters that reach large sizes.

4.5 Conclusion

In this work we have simulated block copolymer and mixed brushes grafted onto cylindrical cellulose nanocrystals under different implicit solvent conditions. We have found that using solvents with different preferences for the polymer components can cause dramatic changes in the resultant brush morphology. For example, a solvent that is good for both components can lead to a highly extended polymer brush, while a solvent that is strongly preferential to one polymer component can cause distinct nanoclustered domains to form.

We have examined the effective free energies between pairs of polymer-grafted nanocrystals under the different solvent conditions in order to gain insight into how collections of nanocrystals would interact. As with the morphology, it was found that the free energy curves take on different qualitative behavior depending on the solvent conditions. Collapsed and well mixed components lead to attractive free energy interactions, while swollen block copolymers lead to highly repulsive free energy interactions.

In addition, we have examined a coarse-grained model of cellulose nanocrystal suspensions with pair interactions derived from free energy behaviors. We have found that cellulose nanocrystals with a propensity to align parallel to one another form strongly semi-crystalline structures, while those that are largely repulsive form more disordered morphologies. Finally, cellulose nanocrystals that have a tendency to cross one another form highly disordered morphologies even with strong attractive interactions present.

4.6 Appendix

4.6.1 Solvent Parameters

Table 4.1: Parameters for the virial model equation of state

Solvent	A	B	C	D
ν_{AA}	0.325275	-2.79721	-11.0412	-11.0412
ν_{BB}	0.325275	0.173237	4.62845	-11.0412
ν_{AB}	2.07856	0.638477	-2.33879	-8.52973
w_{AAA}	0.03	0.06	0.3	0.6
w_{BBB}	0.03	0.03	0.0	0.6
w_{AAB}	0.03	0.03	0.0	0.6
w_{ABB}	0.03	0.03	0.0	0.6

4.6.2 Nanocrystal Suspension Model Parameters

All nanocrystal suspension simulations were performed using Lennard-Jones units in LAMMPS. Individual nanocrystals were modeled as 7 beads spaced one distance unit apart and treated as a single rigid body. For the parallel-aligning nanocrystal, the standard Lennard-Jones potential was used for all beads, with $\sigma = 1$ and $\epsilon = 1$. For the repulsive nanocrystals, the Lennard-Jones potential was truncated at its minimum ($\sigma = 2^{1/6}$) and shifted by 1 energy unit for the energy to be zero beyond this cutoff, producing a purely repulsive potential. For the cross-forming cellulose nanocrystals, Lennard-Jones beads of different σ were used to frustrate alignment and promote an "X-shaped" minimum energy configuration. The center bead was given $\sigma = 1$ while the adjacent beads moving outwards were given $\sigma = 1.3$, 1.6, and 1.9. $\epsilon = 1$ for all beads.

Constant pressure and constant volume simulations were performed with 5000 nanocrystals by reducing the system temperature (in reduced units) from 5.0 down to 0.0 over 5000 time units at a time step of 0.0001. Constant pressure simulations were all performed at a reduced pressure of 1.0, while constant volume simulations were performed in a cubic box

of side length 40.0, 40.0, and 58.0 reduced units for the parallel-aligning, repulsive, and cross-forming cellulose nanocrystals, respectively.

CHAPTER 5

SELF-ASSEMBLY IN BOTTLEBRUSH POLYMERS

5.1 Abstract

Bottlebrush polymers are a class of molecule consisting of a single backbone chain with a high density of polymeric side chains which have gained interest due to their unique physical properties. In this work, we use a simple coarse-grained model to examine the behavior of single and multi-component bottlebrush polymers in the bulk. Specifically, we study the effects that molecular architecture has on single molecule properties and phase separation behavior in multicomponent systems of diblock and Janus bottlebrush polymers. Screening effects are shown to play a large role in determining flexibility in bottlebrush polymers. At high polymer densities, bottlebrush polymers become more flexible and less stretched. Additionally, the relative size of the intermonomer spacing along the backbone compared to the side chain length dictates the range over which intramolecular interactions occur and controls properties such as persistence length. Phase separation behavior was found to differ substantially between diblock and Janus bottlebrushes. In diblocks, the backbone length was found to play a role analogous to that of polymer length in linear polymer systems. Phase separation behavior in Janus bottlebrushes, however, was found to be nearly decoupled from backbone length, while side chain size relative to monomer spacing was found to play a more prominent role.

5.2 Introduction

Bottlebrush polymers are a class of macromolecule whose unique molecular properties have attracted great interest. They consist of a single backbone polymer with a high grafting density of polymeric side chains.[67, 83, 148] The steric hindrance caused by the high density near the backbone can force the side chains to become extended and reduce the flexibility

of the backbone.[106, 105] Several theoretical scaling relationships have been derived for the effect of both side chain length and side chain grafting density on the persistence length of the bottlebrush backbone in both solvent and the melt.[108]

When more than one type of side chain is used, bottlebrush copolymers can be formed. If arranged into more than one block, these bottlebrush copolymers share many features in common with the familiar linear block copolymers, including their ability to self-assemble into well-organized nanostructures. Some of these nanostructures can take on domain spacings in excess of 100 nm.[148] In addition, bottlebrush polymers have been shown to exhibit useful properties in blends with linear polymers. For example, bottlebrush polymers tend to aggregate at surfaces, allowing the conformational entropy of linear chains to increase in the bulk region.[110, 130] Furthermore, they are a useful additive in blends with linear diblocks, and can be used for morphological control of domain sizes.[87]

Theoretical studies have been performed of bottlebrush copolymer melts. One such study used strong segregation theory along with lattice-based Monte Carlo simulations and experiments to examine lamellar pitch dependence on backbone length.[52] Another study examined lamellar pitch dependence on backbone length for many different side chain lengths using experiments and mean field theory.[28] However, the mean field theory methods that were employed required specification of the backbone persistence length and the extent of side chain stretching, both of which should already be specified by other parameters in a full polymer theory. Still further studies have, for example, examined the potential for forming different phases using polymers of very short side chain lengths.[21]

In addition to the diblock copolymer architecture, so-called "Janus" polymers have also been developed as a form of phase separating bottlebrush polymer.[82, 72] Janus bottlebrushes differ from diblock bottlebrushes in that each monomer is doubly grafted with two separate types of polymer. During the self-assembly process, the backbone of the polymer serves as the interface between the two self-segregating side-chain components. In contrast to block bottlebrush polymers, Janus bottlebrushes lack many of the direct analogies to linear

diblocks. For example, the length of the diblock bottlebrush backbone can be considered roughly analogous to the length of a linear block copolymer, whereas the backbone length of a Janus bottlebrush cannot. The ability to form lamella in a direction perpendicular to the orientation of the backbone polymer provides Janus bottlebrushes with many of their unique properties.

The unique molecular characteristics of multicomponent bottlebrush polymers can affect their phase separation properties. In particular, the steric hindrance of the stretched side chains cause bottlebrush polymers to be semiflexible, rather than highly flexible. Semiflexible block copolymers have been shown to have order-disorder transitions at lower temperatures and an increased lamella region of the phase diagram.[89] In addition to semiflexibility, bottlebrush polymer aspect ratios are much lower than linear polymers due to the spreading of the side chains over finite regions. This density smearing has been shown to decrease the order-disorder transition temperature.[140, 29] Lastly, it is believed that the steric hindrance caused by side chains near the backbone can prevent entanglement, which can drastically increase the rate at which self-assembly occurs.[52]

In this work, we perform a study of single and multi-component bottlebrush polymers of various architectures to examine their bulk properties. The dependence of polymer size and persistence length on system polymer density is examined in detail in the first section. In the second section, phase separation properties of diblock and Janus bottlebrushes are examined, particularly in how they differ from each other and linear diblocks, as well as which parameters of the molecule dictate where the order-disorder transition occurs.

5.3 Model and Methods

5.3.1 Model Description

The model of bottlebrush polymers used in this work is an extension of the "canonical" model commonly used to describe linear block copolymer systems.[43, 34, 42] In the linear

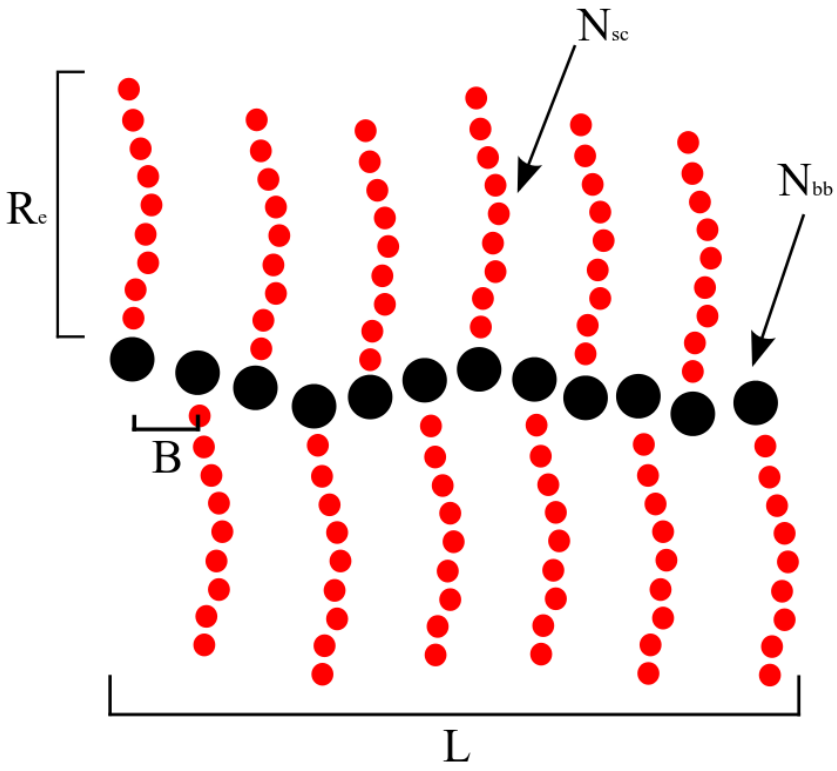

Figure 5.1: Schematic for the bottlebrush polymers studied in this work. Backbone beads are depicted in black, while side chain beads are depicted in red. The parameters examined in this study are the following: N_{sc} is the number of beads making up a single side chain. N_{bb} is the number of beads making up the backbone. R_e is the root-mean-square end to end distance of the side chain. L is the root-mean-square end to end distance of the backbone. B is the distance between two adjacent backbone beads. All distances reported in this work are in units of $R_{e,0}$, the root-mean-square end to end distance of an ideal unperturbed side chain polymer.

polymer model, individual molecules are described as Gaussian chains, which act as good approximations to real polymers so long as the polymer is sufficiently flexible or, in other words, can be considered Gaussian at all length scales of interest. The side chains of the bottlebrush polymer are treated as Gaussian in this model, while the backbone is treated as a freely jointed chain. Since the crowding of side chains near the backbone can be substantial, the freely jointed chain prevents the backbone from becoming stretched to an unphysical extent, while still allowing the chain to bend freely. One important aspect to consider when using this model is that most of the molecule's semiflexibility does not come from the backbone. The semiflexbility is due instead to interactions between sidechains at different points along the backbone, a feature that will be further detailed in the section on semiflexbility.

The bottlebrush model makes use of the following non-bonded interaction potential, which is identical to the one commonly used for systems of linear polymers:[42]

$$\frac{H_{nb}}{k_B T} = \rho_0 \int \chi \phi_A \phi_B + \frac{\kappa}{2}(\phi_A + \phi_B)^2 d\mathbf{r} \tag{5.1}$$

Where χ is a Flory-Huggins parameter and κ is associated with the compressibility of the melt, ρ_0 is the monomer density of the melt, and ϕ_A and ϕ_B are local normalized monomer densities of components A and B, respectively ($\phi_A = \rho_A/\rho_0$).

The model is implemented using Theoretically Informed Coarse-Grained (TICG) simulations.[30, 31, 111] In TICG, continuous Gaussian chains are discretized into discrete Gaussian chains, and a finite interaction distance is introduced to make the model amenable to standard Monte Carlo and Molecular Dynamics simulations. The choice of discretization parameter and interaction distance is, in a sense, arbitrary. However, the general rule has been to discretize the chain enough and choose an interaction distance sufficiently small so that the finest length scales of interest are resolved. As the discretization level gets infinitely fine and the interaction distance becomes infinitely small, the exact Hamiltonian is reproduced.

The non-bonded interaction in the case of a system discretized into N_{sc} side chain beads can be re-written into the following form, which reflects that the choice of N_{sc} is arbitrary.

$$\frac{H_{nb}}{k_B T} = \frac{\rho_0}{N_{sc}} \int \chi N_{sc} \phi_A \phi_B + \frac{\kappa N_{sc}}{2} (\phi_A + \phi_B)^2 d\mathbf{r} \tag{5.2}$$

From the above equation, it can be seen that ρ_0/N_{sc}, the side chain polymer density, as well as χN_{sc} and N_{sc}, the chain interaction parameters, are the true coarse-grained parameters of interest. The energy function is calculated using a zeroth order particle-to-mesh technique that has been described extensively in the literature.[30, 32, 112]

In addition to the energetic and density parameters, several physical parameters are examined for bottlebrush polymers. These parameters are shown in Figure 5.1. All distances are reported in units of $R_{e,0}$, the end-to-end distance of an ideal Gaussian polymer of length N_{sc}. N_{bb} is the number of backbone monomers along the bottlebrush, while L is the root mean square end-to-end distance of the backbone polymer. Finally, B is the distance between two adjacent monomers along the backbone. As B is a parameter that is not easy to control experimentally, it is easier to think of as the term that controls the side chain length. Low B corresponds to larger side chains, as the ratio $B/R_{e,0}$ is small.

5.3.2 Structure Factor Calculations

Structure factors were calculated by treating beads of component A as point scattering centers, yielding the following equation:[120]

$$S(\mathbf{q}) = \left(\sum_i \delta_A \cos(\mathbf{q} \cdot \mathbf{r}_i) \right)^2 + \left(\sum_i \delta_A \sin(\mathbf{q} \cdot \mathbf{r}_i) \right)^2 \tag{5.3}$$

This structure factor was sampled from the simulation every 100 Monte Carlo moves, and averaged to provide the final result.

5.4 Results

5.4.1 Side-Chain Extension and Semiflexibility

One main source of contrast between flexible polymers and bottlebrushes is the crowding of side chains near the backbone, which can cause the side chains to become extended as well as decrease the flexibility of the backbone. These effects are most pronounced in dilute solutions of bottlebrush polymers; in the melt, they are screened to an extent. The exact magnitude of the screening will depend heavily on the polymer density. At low density, the steric repulsion will be strong and cause the backbone to straighten out. At high density, screening effects from surrounding molecules will reduce side chain extension and allow the backbone to be more flexible.

In order to quantify these effects within our model, several simulations were performed for different values of κN_{sc} and different polymer densities, ρ_0/N_{sc}. For all cases, the extent of side chain stretching was determined by calculating root mean square end-to-end distance, R_e, of the side chains, relative to that expected from an unperturbed Gaussian chain: $R_{e,0} = N_{sc}^{1/2} b$, where b refers to the statistical segment length. While side chain stretching is straightforward to quantify, characterizing backbone semiflexbility comes with challenges. The backbone on its own is not semiflexible. Rather, it is the interactions among the side chains which cause the semiflexibility. For these reasons, bottlebrushes cannot be described by a single persistence length in the manner of a wormlike chain. Instead, there are multiple length scales over which different persistence lengths can be defined. Between single monomers, the backbone is highly flexible in that it can make sharp bends quite easily. Over larger length scales, however, the high density of the side chains prevent the polymer from bending back on itself while also forcing the backbone to straighten. The overall effect creates increased orientation correlations over larger length scales. In order to account for the multiple length scales at play in this type of molecule, the orientation correlation function was fit to a function of the following form:

$$c(s) = (1 - M)e^{-s/l_s} + Me^{-s/l_p} \tag{5.4}$$

Where we impose that $l_s \leq l_p$. In the above function, l_s is the small length scale persistence length, which we can assume to be on the order of a single monomer. l_p is the large length scale persistence length, which more directly corresponds to persistence lengths used in the definition of a wormlike chain. M and $1 - M$ refer to the magnitude of the large length scale correlations and small length scale correlations, respectively. In order to provide a comprehensive picture of the dependence of bottlebrush semiflexibility on polymer density, R_e, M, and l_p are plotted as a function of ρ_0/N_{sc} in Figure 5.2. The end-to-end distance of the backbone itself, L, which encodes how much the entire molecule has become stretched, is also plotted.

Remarkably, the persistence length is not strongly correlated with ρ_0/N_{sc} for most of the values studied. While there is a sharp increase in l_p at the lowest densities, for most of the density range l_p stays around 8 backbone monomer units. In fact, the magnitude of the long range correlations, M, and the end-to-end distance of the backbone, L, are better indicators of the density. At low density, M, L, and R_e all take on values consistent with an extended chain: extended side chains, a stretched backbone, and a large magnitude of large length scale correlations. As ρ_0/N_{sc} is decreased, these properties gradually and consistently decrease to the values that would be expected of a highly screened and flexible chain. An interesting result of these calculations is that they appear to indicate that l_p is an intrinsic property of the bottlebrush polymer, and not dependent on the environment that the polymer is immersed within. We believe that the numerical value that l_p takes is dependent on the the size of the side chains relative to the spacing between backbone monomers. A side chain essentially acts as a region of excluded volume around its associated backbone monomer. As indicated by Figure 5.2a, the size of the side chain does not change substantially for much of

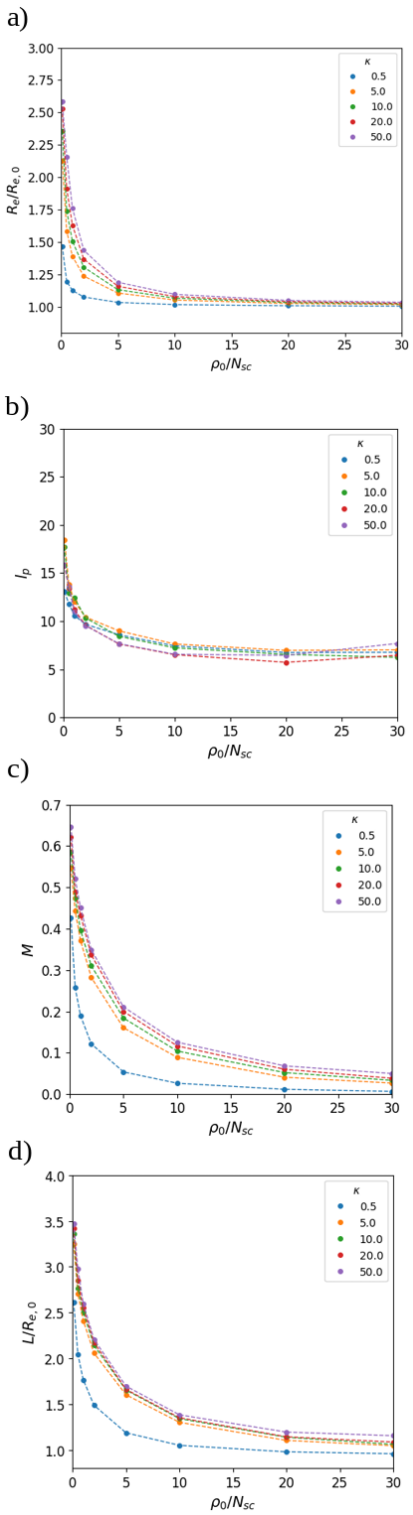

Figure 5.2: Plots of various bottlebrush polymer properties as a function of polymer density: **a)** side chain root mean square end-to-end distance, **b)** backbone long length scale persistence length, **c)** magnitude of long length scale persistence length, **d)** backbone root mean square end-to-end distance. The polymers range from highly rigid and extended at low density, to heavily screened at high density.

the studied ρ_0/N_{sc} range. The side chain must be able to reach a distant backbone monomer in order to interact with it, and the distance over which it can interact is dictated by the size of the side chains. The screening effects associated with increasing ρ_0/N_{sc} does not change this distance, only the strength of the interaction. This effect manifests in the strong M dependence on ρ_0/N_{sc} compared to l_p.

In order to examine these effects further, simulations were run across different values of the intermonomer spacing distance, B, in order to determine if it had a stronger effect on the numerical value of l_p than the polymer density. The results for l_p and the other parameters are presented in Figure 5.3.

There are several details worth indicating. First, side chain extension grows as B decreases (Figure 5.3a). This result aligns well with the idea that decreasing B forces the side chains to be in closer proximity, further increasing the crowding near the backbone and thus causing the side chains to become extended. Second, unlike ρ_0/N_{sc}, changing $B/R_{e,0}$ does consistently change the numerical value of l_p. As the backbone monomer spacing becomes larger, l_p drops. M also drops with increasing ρ_0/N_{sc}, but to a lesser extent. These trends are in agreement with side chain size being the determining factor for orientation correlations.

In addition to ρ_0/N_{sc} and $B/R_{e,0}$, the parameters studied in Figures 5.2 and 5.3 also depend on the repulsive interactive parameter κN_{sc}. As a general trend, increasing κN_{sc} causes the stretching and elongation effects in bottlebrushes to become greater. However, these effects seem to be prominent only for low densities ($\rho_0/N_{sc} < 1.0$). For $\rho_0/N_{sc} \geq 1.0$ and $\kappa N_{sc} \geq 5.0$, the curves overlap each other. Our interpretation of these results is that the value of κN_{sc} is only important when void regions are present. At the lowest densities, the extension of the side chains and backbone is predominantly controlled by the balance between the repulsion of side chains from one another and the spring-like bonded interactions. At higher densities, the bottlebrush molecules more uniformly fill up space, and the exact value of κN_{sc} matters less as the repulsion from surrounding molecules cancels out the

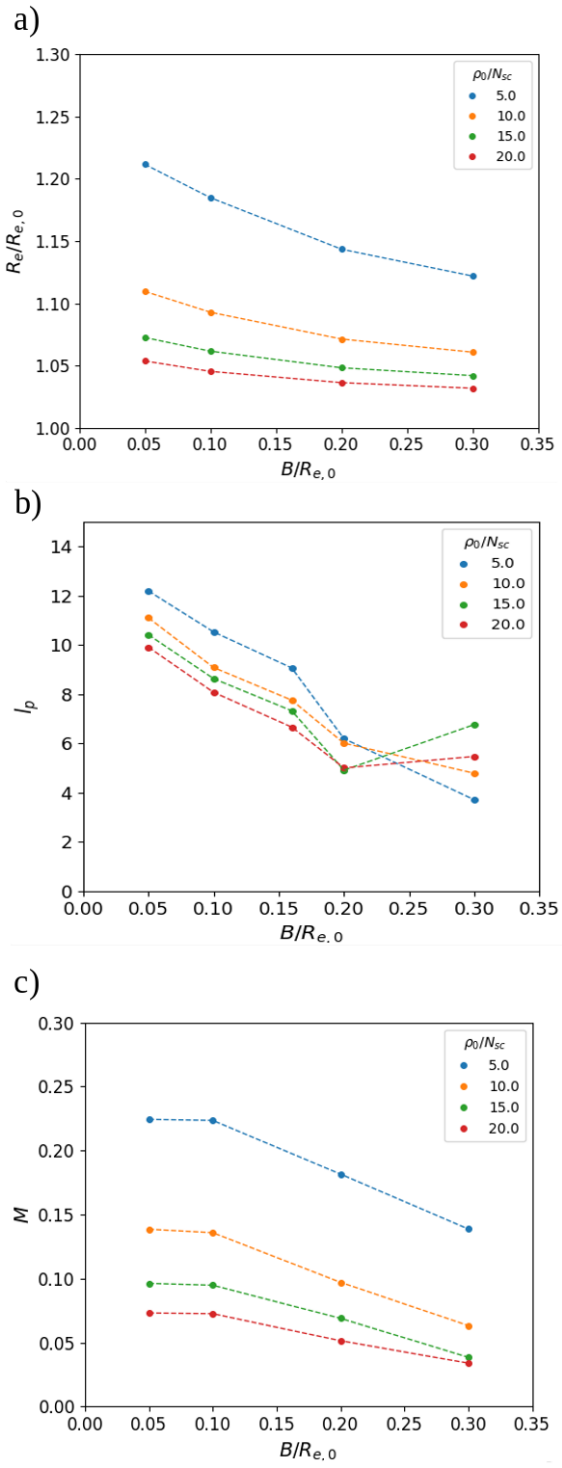

Figure 5.3: Plots of various quantities as a function of backbone monomer spacing, $B/R_{e,0}$: **a)** side chain root mean square end-to-end distance, **b)** backbone long length scale persistence length, **c)** magnitude of long length scale persistence length.

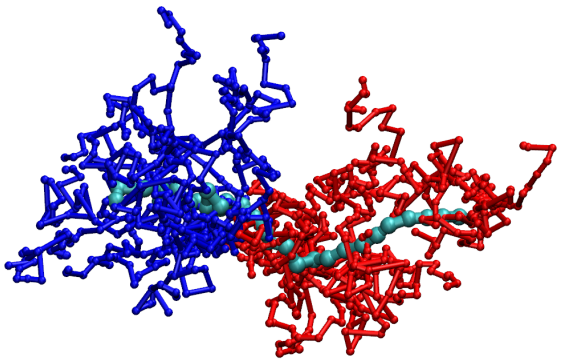

Figure 5.4: Image of a diblock bottlebrush polymer. Green beads represent the backbone monomers of the polymer, while red and blue beads are side chain monomers of monomers type A and B, respectively.

intramolecular repulsion. So long as κN_{sc} is sufficiently high that the particles are able to interact, its exact value is not important.

5.4.2 Microphase Separation in Bottlebrush Polymers

The unique physical properties of bottlebrush polymers, as described in the previous section, can have an effect on their microphase separation behavior in multicomponent systems. In this section, we consider bottlebrush polymers of two immiscible side chain groups arranged into two architectures: diblock bottlebrushes and Janus bottlebrushes. Illustrations of the diblock and Janus bottlebrush architectures are shown in Figures 5.4 and 5.5, respectively.

For simple linear diblock copolymer systems, only three parameters are traditionally considered when examining large scale phase separation behavior: the volume fraction of component A (f), the Flory-Huggins interaction parameter multiplied by the chain length (χN), and the invariant degree of polymerization ($\rho_0 R_e^3/N$).[42] The invariant degree of polymerization is often treated as a "Ginzburg parameter," meaning that it dictates the extent of fluctuations and their effect on the system. In the mean-field limit, the invariant degree of polymerization is taken to be infinite and is no longer considered as a parameter, which can then lead to the well-known mean field phase diagram for block copolymers.[92]

For bottlebrush polymers, the situation is different and more parameters must be consid-

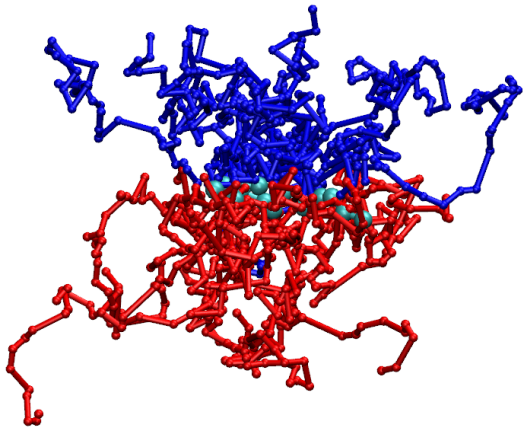

Figure 5.5: Image of a Janus bottlebrush polymer. Green beads represent the backbone monomers of the polymer, while red and blue beads are side chain monomers of monomers type A and B, respectively.

ered in order to accurately describe the molecular structure. Consider, for example, the effect of density on bottlebrush polymers. At experimentally relevant densities, ρ_0/N_{sc} is important because it dictates many of the morphological properties of the polymer, including how extended and stretched it becomes, so it cannot be neglected. In addition to polymer density, we also consider the following molecular parameters. χN_{sc} is treated as the fundamental interaction parameter, akin to χN for linear polymers, as N_{sc} is an arbitrary discretization parameter for the Gaussian chain. N_{bb} is the number of backbone monomers, and f is the volume fraction of type A side chains. In addition, the size of the intermonomer spacing relative to the side chain size, B/R_e, is studied.

In this section, we consider the effect that these parameters have on properties of the phase-separated state, including the natural lamellar periodicity as well as the location of the order disorder transition. For example, in linear diblocks, it is well-known that χN is the parameter that controls whether phase separation occurs. When comparing polymers of length N and $2N$, the polymer of length $2N$ will experience the order-disorder transition at half the value of χ as the one of length N. Depending on the architecture, we can expect different dependencies of the order disorder transition on the bottlebrush parameters. As a simple example, for diblock bottlebrushes, N_{bb} is roughly analogous to N of a linear polymer.

We can expect that for a constant value of χN_{sc} the order disorder transition should occur at roughly constant $\chi N_{sc} N_{bb}$. It is far less clear, however, if this relationship is the same or exists at all for Janus bottlebrushes where the correspondence between N_{bb} and N of the linear polymer is not the same.

Simulations were performed at various values of N_{bb}, B/R_e, ρ_0/N_{sc}, and χN_{sc} with the chain discretization set at a constant value of $N_{sc} = 32$. In all cases, the volume fraction of A was held constant at $f = 0.5$.

Structure factors were calculated in order to quantitatively characterize the morphology, as well as determine when the order-disorder transition was reached. Representative plots of these structure factor calculations for diblock bottlebrushes are shown in Figure 5.6 at different values of N_{bb} (Figure 5.6a) and $B/R_{e,0}$ (Figure 5.6b), while representative plots at varying χN_{sc} and ρ_0/N_{sc} are provided in Figure 5.7. The main feature of interest in these scattering profiles is the lamellar peak location, which is where the structure factor spikes up roughly between $0.15 \leq q \leq 0.6$. The peak location, q_p, is related to the natural periodicity by $L_0 = 1/q_p$.

Figure 5.6a shows q_p decreasing as N_{bb} increases, indicating that the lamellar spacing increases as well. This result is expected because of the increasing polymer length, which is consistent with linear diblocks as well. These results also agree well with experimental studies which have examined lamellar spacing as a function of chain length.[28] The backbone monomer spacing, $B/R_{e,0}$, also affects the spacing. As one would expect, the backbone spacing increases with $B/R_{e,0}$, but not as much as with N_{bb} likely due to the increased flexibility at high $B/R_{e,0}$.

The structure factor trend for different χN_{sc} in Figure 5.7a provides a clear example of the order-disorder transition between χN_{sc} values of 2.0 and 3.0. For χN_{sc} below the order-disorder transition, the structure factor is smooth without any noticeable sharp peaks. At and above the order-disorder transition, the structure factor exhibits a peak corresponding to the natural periodicity of the lamellar phase. The value of χN_{sc} above which the structure

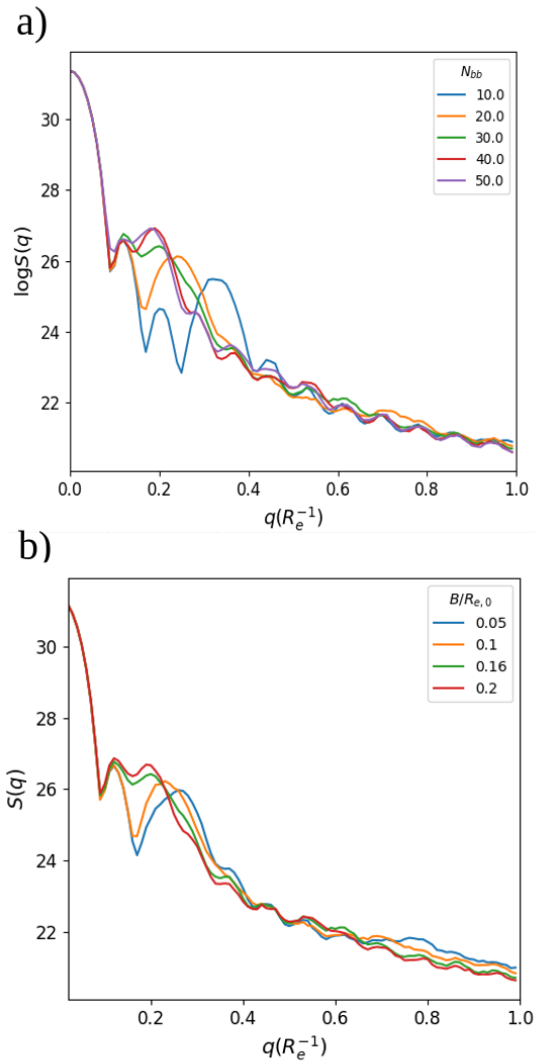

Figure 5.6: Plots of calculated structure factors for a diblock bottlebrush polymer at varying N_{bb} and B. Unless being varied, parameters for all plots shown here were held constant at $\chi N_{sc} = 6.0$, $N_{bb} = 30$, $\rho_0/N_{sc} = 10.0$, and $B/R_{e,0} = 0.16$.

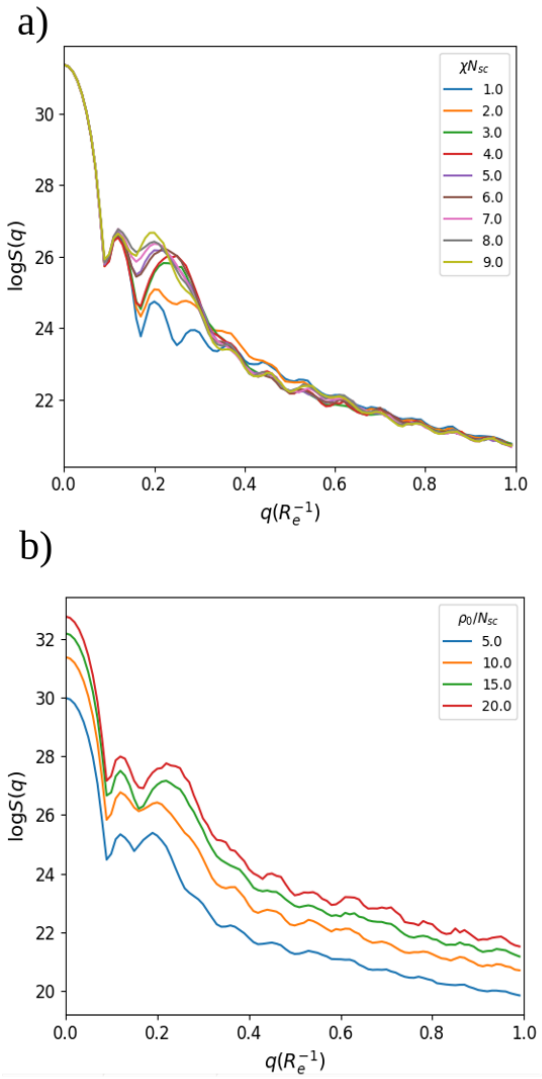

Figure 5.7: Plots of calculated structure factors for a diblock bottlebrush polymer. Unless being varied, parameters for all plots shown here were held constant at $\chi N_{sc} = 6.0$, $N_{bb} = 30$, $\rho_0/N_{sc} = 10.0$, and $B/R_{e,0} = 0.16$.

factor no longer changes appreciably is a good indicator of the order-disorder transition location. There appears to be far less dependence of the lamellar spacing on polymer density, ρ_0/N_{sc}. Only at the lowest density studied ($\rho_0/N_{sc} = 5.0$) does the lamellar spacing increase noticeably. This result is likely due to the increased extension at lower densities, where the backbone mean square end-to-end distance, L, becomes larger due to decreased screening effects. The increased extension of the backbone would then contribute to the increased lamellar spacing.

The Janus bottlebrush structure factors for the same parameters are shown in Figure 5.8 and Figure 5.9, and they differ from the diblock substantially. While the structure factor dependence on χN_{sc} is similar to that of the diblock bottlebrush, the N_{bb}, ρ_0/N_{sc}, and $B/R_{e,0}$ dependence differ considerably. As is evident from Figure 5.8a, the domain spacing of Janus bottlebrush polymers shows almost no dependence on the length of the backbone. This result is not unexpected, as it is the length of the side chains which should dictate the domain spacing for the Janus architecture because there are no "blocks" like in the diblock architecture. As a result of these molecular features, one might consider the Janus bottlebrush spacing as effectively "decoupled" from the backbone polymer length. Another difference is in the effect of ρ_0/N_{sc}. Unlike in the diblock architecture, where domain spacing had only slight dependence on polymer density, in the Janus architecture, the domain spacing increases consistently as the polymer density is decreased. Similar to the homopolymer bottlebrush, the side chain extension can be expected to increase as the polymer density decreases, a result of the decreased screening effects from surrounding molecules. The lamellar spacing in the Janus bottlebrush is dictated by the size of the side chains, so the increased chain extension directly increases the domain spacing as individual side chains take up more volume.

The backbone monomer spacing, $B/R_{e,0}$ affects the domain spacing in a manner similar to the density. As B is decreased, the side chains are forced into closer proximity to one another, causing them to experience greater tension from the repulsive effects. The end result

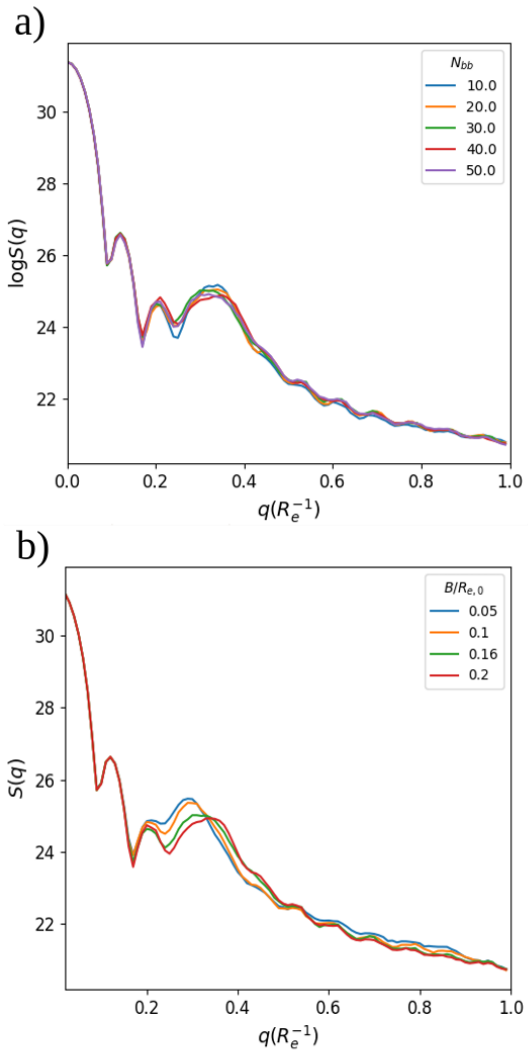

Figure 5.8: Plots of calculated structure factors for a Janus bottlebrush polymer at varying N_{bb} and B. Unless being varied, parameters for all plots shown here were held constant at $\chi N_{sc} = 30.0$, $N_{bb} = 30$, $\rho_0/N_{sc} = 10.0$, and $B/R_{e,0} = 0.16$.

is that the side chains become further extended, as in the case of the homopolymer, which in turn increases the lamellar spacing. An interesting result is that the Janus bottlebrush lamellar spacing dependence on $B/R_{e,0}$ is the opposite of the diblock bottlebrush.

The approximate location of the order-disorder transition was determined by examining structure factor peak dependence on χN_{sc} as well as by inspecting the simulation trajectories directly. Ordered phases are those wherein persistent structures form. Directly below the order-disorder transition, transient structures do form, but they are unstable and do not last over long simulation runs. The order-disorder transition value of χN_{sc} is plotted as a function of both N_{bb} and B for various ρ_0/N_{sc} for both diblock bottlebrush polymers and Janus bottlebrush polymers in Figure 5.10.

The results show, as suggested earlier, that N_{bb} in the diblock plays a role analogous to N in a linear polymer and that the order-disorder transition occurs for values of nearly constant $\chi N_{sc} N_{bb}$. As with linear polymers, we can attribute this feature to a trade-off between the energy associated with a given monomeric unit and the translational entropy associated with a polymer. Entropy is lost as the backbone polymer becomes longer, pushing the system toward an ordered state at lower values of χN_{sc}.

$B/R_{e,0}$ in diblock bottlebrushes has a weaker effect on the order-disorder transition. While there does appear to be a slight downward trend in $(\chi N_{sc})_{ODT}$ as $B/R_{e,0}$ is increased, it is not nearly as strong as the effect from N_{bb}. We suspect that the cause of this small trend comes from polymers with larger B being able to come into contact with more molecules, which then facilitates phase separation.

Janus bottlebrushes have different order-disorder transition behavior compared to diblock bottlebrushes. Of particular note, there is almost no dependence on N_{bb}, especially for $\rho_0/N_{sc} \geq 10$. Phase separation occurs on a much more local scale in Janus bottlebrushes than in diblock bottlebrushes; it occurs at the polymer backbone rather than the interface between large blocks. For any side chain in a Janus bottlebrush, there will be a number of side chains of opposite type in close proximity that are a part of the same molecule.

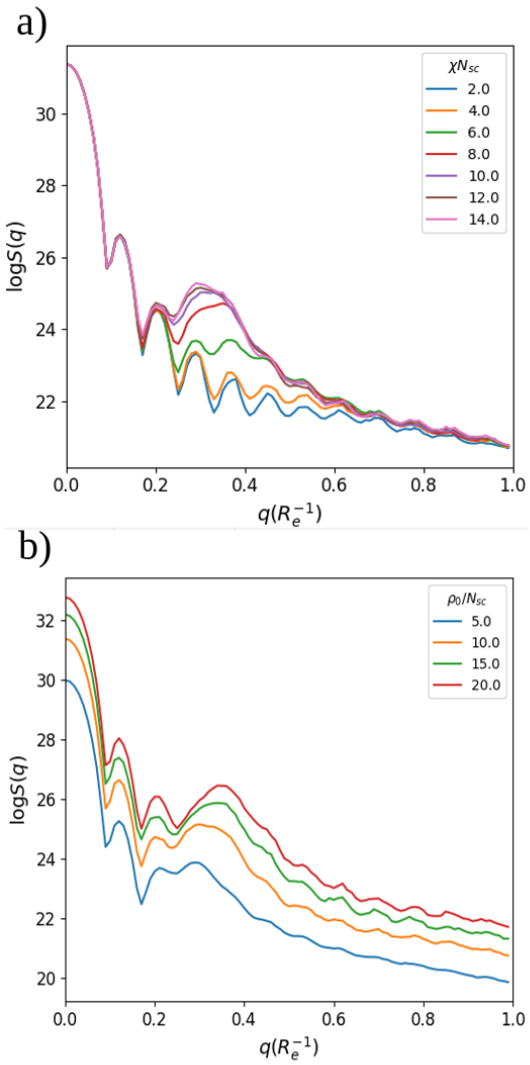

Figure 5.9: Plots of calculated structure factors for a Janus bottlebrush polymer. Unless being varied, parameters for all plots shown here were held constant at $\chi N_{sc} = 30.0$, $N_{bb} = 30$, $\rho_0/N_{sc} = 10.0$, and $B/R_{e,0} = 0.16$.

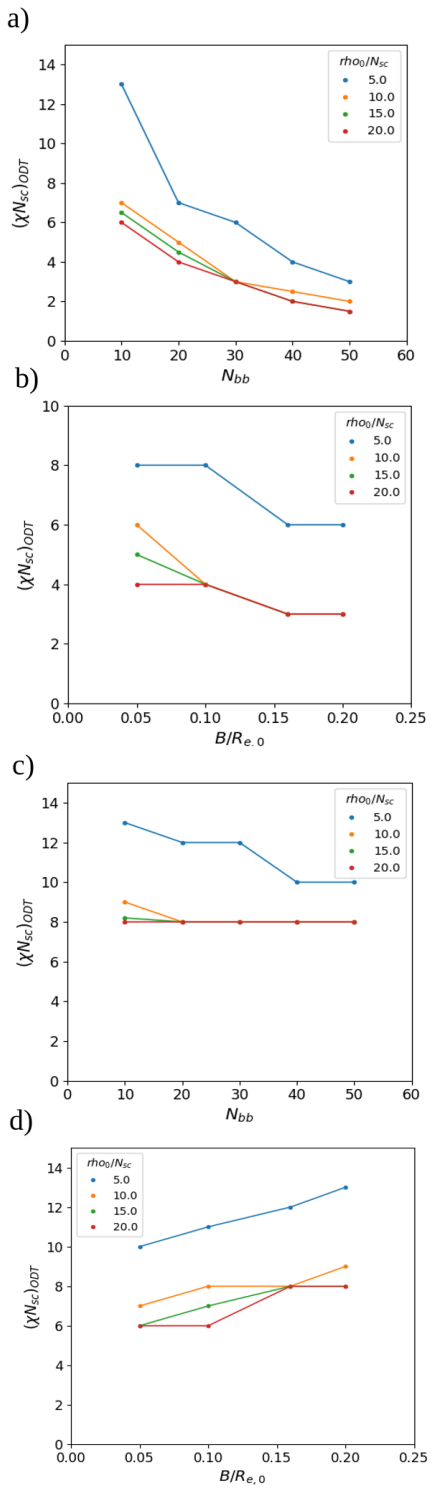

Figure 5.10: Plots of χN_{sc} at the order-disorder transition (ODT) as a function of several parameters for diblock and Janus bottlebrush polymers. **a)** is the diblock bottlebrush with varying backbone length. **b)** is the diblock bottlebrush with varying backbone monomer spacing. **c)** is the Janus bottlebrush with varying backbone length. **d)** is the Janus bottlebrush with varying backbone monomer spacing.

Side chains on remote ends of the molecule will have little effect on one another due to the stiffness of the bottlebrush, so the driving force for phase separation is independent of backbone length. This local form of phase separation is in contrast to diblocks where nearby side chains are of the same type, and in which phase separation must come from interactions of side chains that are not close neighbors on the same molecule.

Of further interest is the Janus bottlebrush order-disorder transition dependence on $B/R_{e,0}$. The value of $(\chi N_{sc})_{ODT}$ increases consistently with $B/R_{e,0}$. We believe that this trend is associated with the backbone chain entropy. At lower values of $B/R_{e,0}$ the side chains are forced into closer proximity which causes the backbone to straighten out. As stated above, phase separation occurs at a local scale in Janus bottlebrushes. When the backbone is rigid and straight, It is easier for the side chains of a single molecule to align and find side chains of like type on other molecules. Additionally, having a rigid bottlebrush makes it easier for the backbone to restrict itself to the effectively two-dimensional interface between domains. When $B/R_{e,0}$ is large, the backbone is more flexible and can more easily contort into a variety of random coil-like shapes, which makes it more difficult for the side chains to align with one another consistently and for the backbone to restrict itself to the interface.

5.5 Conclusion

In this study, various architectures of bottlebrush polymers were examined and compared to corresponding linear polymers. First, homopolymer bottlebrushes consisting only of a single type of side chain were studied at different densities to examine molecular screening in the melt. It was found that at low polymer density, crowding of side chains near the backbone caused the molecule to expand and increased the rigidity of the backbone as well as the magnitude of long length scale orientation correlations. At high polymer density, the molecule becomes more flexible and behaves more like an ideal polymer, albeit one with a low aspect ratio.

Second, microphase separation of diblock and Janus bottlebrush polymers were examined and compared to linear diblocks. In the diblock bottlebrushes, the length of the backbone was found to play a role roughly analogous to N in linear polymers, while the length of the backbone was unrelated to phase separation in Janus bottlebrushes. In Janus bottlebrushes, it was found that placing the monomers of the backbone more closely together rigidified the molecule and thus facilitated phase separation.

CHAPTER 6

CONCLUSIONS

In conclusion, this dissertation has shown a variety of coarse-grained models designed specifically to tackle large, anisotropic, and semiflexible molecules and systems. Specifically, we have developed four new models to study conjugated materials, nematic polymer brushes, polymer-grafted cellulose nanocrystals, and bottlbrush polymers. Each of these models has been used to perform a study and derive new results for their respective materials.

In Chapter 2, we used an anisotropic pair potential to coarse-grain the large, twisted, and rigid regions that are commonly found in disk-like conjugated materials. This model was then used to characterize perylene diimide based materials arranged in different architectures. Specifically, we found that the most twisted molecules were more effective in generating percolative charge transfer networks. In Chapter 3, we developed a coarse-grained polymer model that combined the semiflexbility of the wormlike chain with the nematic interactions of the Maier-Saupe liquid crystal model. This model was then used to quantify the different phases that can be formed by a liquid crystalline polymer brush, including the different types of nematically collapsed states. We found that at low grafting densities, many small nematic clusters formed near the substrate surface that do not affect one another. As the grafting density was increased, these clusters combined together to form one single nematic domain. We also found that these clusters form more easily for polymers of shorter length. As the polymer length was increased, configurational entropy played a more prominent role, leading to isotropic states. In Chapter 4, we developed a model to examine solvent effects on polymers grafted onto cellulose nanocrystals. We adapted a virial equation of state-based model to study multicomponent brushes in solvents that act as good and poor solvents for the separate components. We found that a distinct variety of morphologies can form in the presence of different solvents which can have a large effect on the pair interactions between entire cellulose nanocrystals, making them alternately attractive or repulsive to each other. Finally, in Chapter 5, we examined a class of molecule called bottlebrush polymers

which consist of a single backbone chain with sidechains which are themselves polymeric. We examined both single component and multi-component bottlebrush polymers arranged into different architectures. Of particular interest were diblock and Janus bottlebrushes. We found that diblock bottlebrushes exhibited phase separation behavior similar to linear diblock copolymers, albeit with the added complexity that comes from the stretching of side chains close to the backbone. Janus bottlebrushes showed substantially different behavior, in that the phase separation behavior was effectively decoupled from the length of the backbone. Instead, its phase separation behavior was more dependent on the amount of side chain extension.

REFERENCES

[1] Riccardo Alessandri, Jaakko J Uusitalo, Alex H de Vries, Remco WA Havenith, and Siewert J Marrink. Bulk heterojunction morphologies with atomistic resolution from coarse-grain solvent evaporation simulations. *Journal of the American Chemical Society*, 139(10):3697–3705, 2017.

[2] S Alexander. Adsorption of chain molecules with a polar head a scaling description. *Journal De Physique*, 38(8):983–987, 1977.

[3] Michael P Allen and Guido Germano. Expressions for forces and torques in molecular simulations using rigid bodies. *Molecular Physics*, 104(20-21):3225–3235, 2006.

[4] P Auroy, L Auvray, and L Leger. Characterization of the brush regime for grafted polymer layers at the solid-liquid interface. *Physical review letters*, 66(6):719, 1991.

[5] M Babadi, R Everaers, and MR Ejtehadi. Coarse-grained interaction potentials for anisotropic molecules. *The Journal of chemical physics*, 124(17):174708, 2006.

[6] Christopher M. Baker and Guy H. Grant. The structure of liquid benzene. *Journal of Chemical Theory and Computation*, 2(4):947–955, 2006.

[7] Heinz Bässler. Charge transport in disordered organic photoconductors a monte carlo simulation study. *physica status solidi (b)*, 175(1):15–56, 1993.

[8] Martin A Bates and Claudio Zannoni. A molecular dynamics simulation study of the nematic–isotropic interface of a gay–berne liquid crystal. *Chemical physics letters*, 280(1):40–45, 1997.

[9] Bjorn Baumeier, James Kirkpatrick, and Denis Andrienko. Density-functional based determination of intermolecular charge transfer properties for large-scale morphologies. *The Journal of chemical physics*, 12(36):11103–11113, 2010.

[10] Roberto Berardi, Carlo Fava, and Claudio Zannoni. A gay–berne potential for dissimilar biaxial particles. *Chemical physics letters*, 297(1):8–14, 1998.

[11] Roberto Berardi, Silvia Orlandi, and Claudio Zannoni. Monte carlo simulation of discotic gay–berne mesogenswith axial dipole. *Journal of the Chemical Society, Faraday Transactions*, 93(8):1493–1496, 1997.

[12] Markus Biesalski and Jürgen Rühe. Scaling laws for the swelling of neutral and charged polymer brushes in good solvents. *Macromolecules*, 35(2):499–507, 2002.

[13] Joel H Bombile, Michael J Janik, and Scott T Milner. Tight binding model of conformational disorder effects on the optical absorption spectrum of polythiophenes. *Physical Chemistry Chemical Physics*, 18(18):12521–12533, 2016.

[14] Xiaodong Cao, Hua Dong, and Chang Ming Li. New nanocomposite materials reinforced with flax cellulose nanocrystals in waterborne polyurethane. *Biomacromolecules*, 8(3):899–904, 2007.

[15] Xiaodong Cao, Youssef Habibi, and Lucian A Lucia. One-pot polymerization, surface grafting, and processing of waterborne polyurethane-cellulose nanocrystal nanocomposites. *Journal of Materials Chemistry*, 19(38):7137–7145, 2009.

[16] Jeffrey R Capadona, Kadhiravan Shanmuganathan, Dustin J Tyler, Stuart J Rowan, and Christoph Weder. Stimuli-responsive polymer nanocomposites inspired by the sea cucumber dermis. *science*, 319(5868):1370–1374, 2008.

[17] Tanya L Chantawansri, August W Bosse, Alexander Hexemer, Hector D Ceniceros, Carlos J García-Cervera, Edward J Kramer, and Glenn H Fredrickson. Self-consistent field theory simulations of block copolymer assembly on a sphere. *Physical Review E*, 75(3):031802, 2007.

[18] Shenfu Chen, Lingyan Li, Chao Zhao, and Jie Zheng. Surface hydration: principles and applications toward low-fouling/nonfouling biomaterials. *Polymer*, 51(23):5283–5293, 2010.

[19] Wangqiao Chen and Qichun Zhang. Recent progress in non-fullerene small molecule acceptors in organic solar cells (oscs). *Journal of Materials Chemistry C*, 5(6):1275–1302, 2017.

[20] Wei-Liang Chen, Roselynn Cordero, Hai Tran, and Christopher K Ober. 50th anniversary perspective: Polymer brushes: Novel surfaces for future materials. *Macromolecules*, 50(11):4089–4113, 2017.

[21] Alexandros Chremos and Panagiotis E Theodorakis. Morphologies of bottle-brush block copolymers. *ACS Macro Letters*, 3(10):1096–1100, 2014.

[22] Douglas J Cleaver, Christopher M Care, Michael P Allen, and Maureen P Neal. Extension and generalization of the gay-berne potential. *Physical Review E*, 54(1):559, 1996.

[23] Elvis Cudjoe, Katie M Herbert, and Stuart J Rowan. Strong, rebondable, dynamic cross-linked cellulose nanocrystal polymer nanocomposite adhesives. *ACS applied materials & interfaces*, 10(36):30723–30731, 2018.

[24] Elvis Cudjoe, Mo Hunsen, Zhaojun Xue, Amanda E Way, Elizabeth Barrios, Rebecca A Olson, Michael JA Hore, and Stuart J Rowan. Miscanthus giganteus: A commercially viable sustainable source of cellulose nanocrystals. *Carbohydrate polymers*, 155:230–241, 2017.

[25] Elvis Cudjoe, Shaghayegh Khani, Amanda E Way, Michael JA Hore, Joao Maia, and Stuart J Rowan. Biomimetic reversible heat-stiffening polymer nanocomposites. *ACS central science*, 3(8):886–894, 2017.

[26] Elvis Cudjoe, Mousa Younesi, Edward Cudjoe, Ozan Akkus, and Stuart J Rowan. Synthesis and fabrication of nanocomposite fibers of collagen-cellulose nanocrystals by coelectrocompaction. *Biomacromolecules*, 18(4):1259–1267, 2017.

[27] Koffi L Dagnon, Kadhiravan Shanmuganathan, Christoph Weder, and Stuart J Rowan. Water-triggered modulus changes of cellulose nanofiber nanocomposites with hydrophobic polymer matrices. *Macromolecules*, 45(11):4707–4715, 2012.

[28] Samuel J Dalsin, Thomas G Rions-Maehren, Marissa D Beam, Frank S Bates, Marc A Hillmyer, and Mark W Matsen. Bottlebrush block polymers: Quantitative theory and experiments. *ACS nano*, 9(12):12233–12245, 2015.

[29] Kris T Delaney and Glenn H Fredrickson. Recent developments in fully fluctuating field-theoretic simulations of polymer melts and solutions. *The Journal of Physical Chemistry B*, 120(31):7615–7634, 2016.

[30] Fran A Detcheverry, Huiman Kang, Kostas Ch Daoulas, Marcus Müller, Paul F Nealey, and Juan J de Pablo. Monte Carlo simulations of a coarse grain model for block copolymers and nanocomposites. *Macromolecules*, 41(13):4989–5001, 2008.

[31] Francois A Detcheverry, Darin Q Pike, Paul F Nealey, Marcus Müller, and Juan J de Pablo. Monte carlo simulation of coarse grain polymeric systems. *Physical Review Letters*, 102(19):197801, 2009.

[32] François A Detcheverry, Darin Q Pike, Paul F Nealey, Marcus Müller, and Juan J de Pablo. Monte carlo simulation of coarse grain polymeric systems. *Physical review letters*, 102(19):197801, 2009.

[33] Khanh Do, Mahesh Kumar Ravva, Tonghui Wang, and Jean-Luc Bredas. Computational methodologies for developing structure–morphology–performance relationships in organic solar cells: A protocol review. *Chemistry of Materials*, 29(1):346–354, 2016.

[34] Masao Doi and Samuel Frederick Edwards. *The theory of polymer dynamics*, volume 73. oxford university press, 1988.

[35] John Draper, Igor Luzinov, Sergiy Minko, Igor Tokarev, and Manfred Stamm. Mixed polymer brushes by sequential polymer addition: Anchoring layer effect. *Langmuir*, 20(10):4064–4075, 2004.

[36] Chunmiao Du, Yujin Ji, Junwei Xue, Tingjun Hou, Jianxin Tang, Shuit-Tong Lee, and Youyong Li. Morphology and performance of polymer solar cell characterized by dpd simulation and graph theory. *Scientific reports*, 5:16854, 2015.

[37] Emmanuel LP Dumont, Herve Belmas, and Henry Hess. Observing the mushroom-to-brush transition for kinesin proteins. *Langmuir*, 29(49):15142–15145, 2013.

[38] Erik W Edwards, Martha F Montague, Harun H Solak, Craig J Hawker, and Paul F Nealey. Precise control over molecular dimensions of block-copolymer domains using the interfacial energy of chemically nanopatterned substrates. *Advanced Materials*, 16(15):1315–1319, 2004.

[39] Stephen J Eichhorn, A Dufresne, M Aranguren, NE Marcovich, JR Capadona, SJ Rowan, Christoph Weder, Wim Thielemans, M Roman, W Renneckar, S Gindl, S. Veigel, J. Keckes, H. Yano, K. Abe, M. Nogi, A. N. Nakagaito, A. Mangalam, J. Simonsen, A. S. Benight, A. Bismarck, L. A. Berglund, and T. Peijs. current international research into cellulose nanofibres and nanocomposites. *Journal of materials science*, 45(1):1, 2010.

[40] Samira Elazzouzi-Hafraoui, Yoshiharu Nishiyama, Jean-Luc Putaux, Laurent Heux, Frédéric Dubreuil, and Cyrille Rochas. The shape and size distribution of crystalline nanoparticles prepared by acid hydrolysis of native cellulose. *Biomacromolecules*, 9(1):57–65, 2007.

[41] APJ Emerson, S Faetti, and C Zannoni. Monte carlo simulation of the nematic-vapour interface for a gay-berne liquid crystal. *Chemical physics letters*, 271(4-6):241–246, 1997.

[42] Glenn Fredrickson. *The equilibrium theory of inhomogeneous polymers*. Oxford University Press, USA, 2006.

[43] Karl F Freed. Functional integrals and polymer statistics. *Advances in Chemical Physics*, pages 1–128, 1972.

[44] Daan Frenkel and Berend Smit. *Understanding molecular simulation: from algorithms to applications*, volume 1. Elsevier, 2001.

[45] Andrew Gelman, John B Carlin, Hal S Stern, David B Dunson, Aki Vehtari, and Donald B Rubin. *Bayesian data analysis*. Chapman and Hall/CRC, 2013.

[46] Patrick Gemünden, Carl Poelking, Kurt Kremer, Denis Andrienko, and Kostas Ch Daoulas. Nematic ordering, conjugation, and density of states of soluble polymeric semiconductors. *Macromolecules*, 46(14):5762–5774, 2013.

[47] Patrick Gemünden, Carl Poelking, Kurt Kremer, Kostas Daoulas, and Denis Andrienko. Effect of mesoscale ordering on the density of states of polymeric semiconductors. *Macromolecular rapid communications*, 36(11):1047–1053, 2015.

[48] Valeriy V Ginzburg. Modeling the morphology and phase behavior of one-component polymer-grafted nanoparticle systems. *Macromolecules*, 50(23):9445–9455, 2017.

[49] Pavel A Golubkov and Pengyu Ren. Generalized coarse-grained model based on point multipole and gay-berne potentials. *The Journal of chemical physics*, 125(6):064103, 2006.

[50] Jonathan Gross, Momchil Ivanov, and Wolfhard Janke. Comparing atomistic and coarse-grained simulations of p3ht. In *Journal of Physics: Conference Series*, volume 750, page 012009. IOP Publishing, 2016.

[51] Ferdinand C Grozema, Piet Th Van Duijnen, Yuri A Berlin, Mark A Ratner, and Laurens DA Siebbeles. Intramolecular charge transport along isolated chains of conjugated polymers: effect of torsional disorder and polymerization defects. *The Journal of Physical Chemistry B*, 106(32):7791–7795, 2002.

[52] Weiyin Gu, June Huh, Sung Woo Hong, Benjamin R Sveinbjornsson, Cheolmin Park, Robert Howard Grubbs, and Thomas P Russell. Self-assembly of symmetric brush diblock copolymers. *ACS nano*, 7(3):2551–2558, 2013.

[53] David Guzonas, Daniele Boils, and Michael L Hair. Surface force measurements of polystyrene-block-poly (ethylene oxide) adsorbed from a nonselective solvent on mica. *Macromolecules*, 24(11):3383–3387, 1991.

[54] Youssef Habibi, Lucian A Lucia, and Orlando J Rojas. Cellulose nanocrystals: chemistry, self-assembly, and applications. *Chemical reviews*, 110(6):3479–3500, 2010.

[55] A Halperin, M Tirrell, and TP Lodge. Tethered chains in polymer microstructures. In *Macromolecules: Synthesis, Order and Advanced Properties*, pages 31–71. Springer, 1992.

[56] Thomas F Harrelson, Adam J Moulé, and Roland Faller. Modeling organic electronic materials: bridging length and time scales. *Molecular Simulation*, 43(10-11):730–742, 2017.

[57] Patrick E. Hartnett, Eric A. Margulies, H.S.S. Ramakrishna Matte, Mark C. Hersam, Tobin J. Marks, and Michael R. Wasielewski. Effects of crystalline perylenediimide acceptor morphology on optoelectronic properties and device performance. *Chemistry of Materials*, 28(11):3928–3936, 2016.

[58] Patrick E Hartnett, HSS Ramakrishna Matte, Nicholas D Eastham, Nicholas E Jackson, Yilei Wu, Lin X Chen, Mark A Ratner, Robert PH Chang, Mark C Hersam, Michael R Wasielewski, and Tobin J Marks. Ring-fusion as a perylenediimide dimer design concept for high-performance non-fullerene organic photovoltaic acceptors. *Chemical Science*, 7(6):3543–3555, 2016.

[59] Michael M Henry, Matthew L Jones, Stefan D Oosterhout, Wade A Braunecker, Travis W Kemper, Ross E Larsen, Nikos Kopidakis, Michael F Toney, Dana C Olson, and Eric Jankowski. Simplified models for accelerated structural prediction of conjugated semiconducting polymers. *The Journal of Physical Chemistry C*, 121(47):26528–26538, 2017.

[60] J Hernández-Rojas, F Calvo, S Niblett, and DJ Wales. Dynamics and thermodynamics of the coronene octamer described by coarse-grained potentials. *Physical Chemistry Chemical Physics*, 19(3):1884–1895, 2017.

[61] David M Huang, Roland Faller, Khanh Do, and Adam J Moulé. Coarse-grained computer simulations of polymer/fullerene bulk heterojunctions for organic photovoltaic applications. *Journal of chemical theory and computation*, 6(2):526–537, 2009.

[62] Sergei Izvekov and Gregory A Voth. A multiscale coarse-graining method for biomolecular systems. *The Journal of Physical Chemistry B*, 109(7):2469–2473, 2005.

[63] Nicholas E Jackson, Kevin L Kohlstedt, Lin X Chen, and Mark A Ratner. A n-vector model for charge transport in molecular semiconductors. *The Journal of chemical physics*, 145(20):204102, 2016.

[64] Nicholas E Jackson, Brett M Savoie, Lin X Chen, and Mark A Ratner. A simple index for characterizing charge transport in molecular materials. *The journal of physical chemistry letters*, 6(6):1018–1021, 2015.

[65] Eric Jankowski, Hilary S Marsh, and Arthi Jayaraman. Computationally linking molecular features of conjugated polymers and fullerene derivatives to bulk heterojunction morphology. *Macromolecules*, 46(14):5775–5785, 2013.

[66] SI Jeon, JH Lee, JD Andrade, and PrG De Gennes. Proteinsurface interactions in the presence of polyethylene oxide: I. simplified theory. *Journal of colloid and interface science*, 142(1):149–158, 1991.

[67] Sheuli Jha, Samrat Dutta, and Ned B Bowden. Synthesis of ultralarge molecular weight bottlebrush polymers using grubbs' catalysts. *Macromolecules*, 37(12):4365–4374, 2004.

[68] Steven G. Johnson. The nlopt nonlinear-optimization package. http://ab-initio.mit.edu/nlopt.

[69] William L. Jorgensen, David S. Maxwell, and J. Tirado-Rives. Development and testing of the opls all-atom force field on conformational energetics and properties of organic liquids. *Journal of the American Chemical Society*, 118(45):11225–11236, 1996.

[70] H Kamberaj, RJ Low, and MP Neal. Time reversible and symplectic integrators for molecular dynamics simulations of rigid molecules. *The Journal of chemical physics*, 122(22):224114, 2005.

[71] Hanieh Kargarzadeh, Marcos Mariano, Jin Huang, Ning Lin, Ishak Ahmad, Alain Dufresne, and Sabu Thomas. Recent developments on nanocellulose reinforced polymer nanocomposites: A review. *Polymer*, 132:368–393, 2017.

[72] Ken Kawamoto, Mingjiang Zhong, Karim R Gadelrab, Li-Chen Cheng, Caroline A Ross, Alfredo Alexander-Katz, and Jeremiah A Johnson. Graft-through synthesis and assembly of janus bottlebrush polymers from a-branch-b diblock macromonomers. *Journal of the American Chemical Society*, 138(36):11501–11504, 2016.

[73] Nicola Kleppmann and Sabine HL Klapp. A scale-bridging modeling approach for anisotropic organic molecules at patterned semiconductor surfaces. *The Journal of Chemical Physics*, 142(6):064701, 2015.

[74] Elena F Koslover and Andrew J Spakowitz. Discretizing elastic chains for coarse-grained polymer models. *Soft Matter*, 9(29):7016–7027, 2013.

[75] Joseph Kushick and Bruce J Berne. Computer simulation of anisotropic molecular fluids. *The Journal of Chemical Physics*, 64(4):1362–1367, 1976.

[76] Dmitri V Kuznetsov and Zheng Yu Chen. Semiflexible polymer brushes: a scaling theory. *The Journal of chemical physics*, 109(16):7017–7027, 1998.

[77] Cheng K Lee, Chi C Hua, and Show A Chen. Hybrid solvents incubated π- π stacking in quenched conjugated polymer resolved by multiscale computation. *Macromolecules*, 44(2):320–324, 2010.

[78] Cheng K Lee, Chi C Hua, and Show A Chen. Parametrization of the gay–berne potential for conjugated oligomer with a high aspect ratio. *The Journal of chemical physics*, 133(6):064902, 2010.

[79] Cheng K Lee, Chi C Hua, and Show A Chen. An ellipsoid-chain model for conjugated polymer solutions. *The Journal of chemical physics*, 136(8):084901, 2012.

[80] Cheng-Kuang Lee and Chun-Wei Pao. Nanomorphology evolution of p3ht/pcbm blends during solution-processing from coarse-grained molecular simulations. *The Journal of Physical Chemistry C*, 118(21):11224–11233, 2014.

[81] Joshua P. Lequieu. *Self Assembly with DNA: From Materials Design to Chromatin*. PhD thesis, 2017.

[82] Yukun Li, Efrosyni Themistou, Jiong Zou, Biswa P Das, Marina Tsianou, and Chong Cheng. Facile synthesis and visualization of janus double-brush copolymers. *ACS Macro Letters*, 1(1):52–56, 2011.

[83] Zhou Li, Ke Zhang, Jun Ma, Chong Cheng, and Karen L Wooley. Facile syntheses of cylindrical molecular brushes by a sequential raft and romp grafting-through methodology. *Journal of Polymer Science Part A: Polymer Chemistry*, 47(20):5557–5563, 2009.

[84] Juho S Lintuvuori and Mark R Wilson. A new anisotropic soft-core model for the simulation of liquid crystal mesophases. *The Journal of chemical physics*, 128(4):044906, 2008.

[85] Sheng-Gao. Liu, G. Sui, Russel A. Cormier, Roger M. Leblanc, and Brian A. Gregg. Self-organizing liquid crystal perylene diimide thin films: Spectroscopy, crystallinity, and molecular orientation. *Journal of Physical Chemistry B*, 106(6):1307–1315, 2002.

[86] Alexey V Lyulin, Muataz S Al-Barwani, Michael P Allen, Mark R Wilson, Igor Neelov, and Nicholas K Allsopp. Molecular dynamics simulation of main chain liquid crystalline polymers. *Macromolecules*, 31(14):4626–4634, 1998.

[87] Adeline Huizhen Mah, Pantea Afzali, Luqing Qi, Stacy Pesek, Rafael Verduzco, and Gila E Stein. Bottlebrush copolymer additives for immiscible polymer blends. *Macromolecules*, 51(15):5665–5675, 2018.

[88] P Mansky, Y Liu, E Huang, TP Russell, and C Hawker. Controlling polymer-surface interactions with random copolymer brushes. *Science*, 275(5305):1458–1460, 1997.

[89] Shifan Mao, Quinn MacPherson, and Andrew J Spakowitz. Polymer semiflexibility induces nonuniversal phase transitions in diblock copolymers. *Physical review letters*, 120(6):067802, 2018.

[90] Sergiy Markutsya, Rodney O Fox, and Shankar Subramaniam. Coarse-graining approach to infer mesoscale interaction potentials from atomistic interactions for aggregating systems. *Industrial & Engineering Chemistry Research*, 51(49):16116–16134, 2012.

[91] Hilary S Marsh, Eric Jankowski, and Arthi Jayaraman. Controlling the morphology of model conjugated thiophene oligomers through alkyl side chain length, placement, and interactions. *Macromolecules*, 47(8):2736–2747, 2014.

[92] Mark William Matsen. Fast and accurate scft calculations for periodic block-copolymer morphologies using the spectral method with anderson mixing. *The European Physical Journal E*, 30(4):361, 2009.

[93] Dong Meng, Huiting Fu, Chengyi Xiao, Xiangyi Meng, Thorsten Winands, Wei Ma, Wei Wei, Bingbing Fan, Lijun Huo, Yan Doltsinis, Nikos L Li, Yanming Sun, and Zhaohui Wang. Three-bladed rylene propellers with three-dimensional network assembly for organic electronics. *Journal of the American Chemical Society*, 138(32):10184–10190, 2016.

[94] Lionel CH Moh, Mark D Losego, and Paul V Braun. Solvent quality effects on scaling behavior of poly (methyl methacrylate) brushes in the moderate-and high-density regimes. *Langmuir*, 27(7):3698–3702, 2011.

[95] Robert J Moon, Ashlie Martini, John Nairn, John Simonsen, and Jeff Youngblood. Cellulose nanomaterials review: structure, properties and nanocomposites. *Chemical Society Reviews*, 40(7):3941–3994, 2011.

[96] Mikhail Motornov, Ro Sheparovych, Robert Lupitskyy, Emily MacWilliams, Olha Hoy, Igor Luzinov, and Sergiy Minko. Stimuli-responsive colloidal systems from mixed brush-coated nanoparticles. *Advanced functional materials*, 17(14):2307–2314, 2007.

[97] Biswaroop Mukherjee, Luigi Delle Site, Kurt Kremer, and Christine Peter. Derivation of coarse grained models for multiscale simulation of liquid crystalline phase transitions. *The Journal of Physical Chemistry B*, 116(29):8474–8484, 2012.

[98] Florian Müller-Plathe. Coarse-graining in polymer simulation: from the atomistic to the mesoscopic scale and back. *ChemPhysChem*, 3(9):754–769, 2002.

[99] Kevin P Murphy. *Machine learning: a probabilistic perspective*. MIT press, 2012.

[100] Baochau N Nguyen, Elvis Cudjoe, Anna Douglas, Daniel Scheiman, Linda McCorkle, Mary Ann B Meador, and Stuart J Rowan. Polyimide cellulose nanocrystal composite aerogels. *Macromolecules*, 49(5):1692–1703, 2016.

[101] WG Noid, Jhih-Wei Chu, Gary S Ayton, Vinod Krishna, Sergei Izvekov, Gregory A Voth, Avisek Das, and Hans C Andersen. The multiscale coarse-graining method. i. a rigorous bridge between atomistic and coarse-grained models. *The Journal of chemical physics*, 128(24):244114, 2008.

[102] WG Noid, Pu Liu, Yanting Wang, Jhih-Wei Chu, Gary S Ayton, Sergei Izvekov, Hans C Andersen, and Gregory A Voth. The multiscale coarse-graining method. ii. numerical implementation for coarse-grained molecular models. *The Journal of chemical physics*, 128(24):244115, 2008.

[103] Rodrigo Noriega, Jonathan Rivnay, Koen Vandewal, Felix PV Koch, Natalie Stingelin, Paul Smith, Michael F Toney, and Alberto Salleo. A general relationship between disorder, aggregation and charge transport in conjugated polymers. *Nature materials*, 12(11):1038, 2013.

[104] Hisashi Okumura, Satoru G Itoh, and Yuko Okamoto. Explicit symplectic integrators of molecular dynamics algorithms for rigid-body molecules in the canonical, isobaric-isothermal, and related ensembles. *The Journal of chemical physics*, 126(8):084103, 2007.

[105] Sergey Panyukov, Ekaterina B Zhulina, Sergei S Sheiko, Greg C Randall, James Brock, and Michael Rubinstein. Tension amplification in molecular brushes in solutions and on substrates. *The Journal of Physical Chemistry B*, 113(12):3750–3768, 2009.

[106] Sergey V Panyukov, Sergei S Sheiko, and Michael Rubinstein. Amplification of tension in branched macromolecules. *Physical review letters*, 102(14):148301, 2009.

[107] Leonid Paramonov and Sophia N Yaliraki. The directional contact distance of two ellipsoids: Coarse-grained potentials for anisotropic interactions. *The Journal of chemical physics*, 123(19):194111, 2005.

[108] Jarosław Paturej, Sergei S Sheiko, Sergey Panyukov, and Michael Rubinstein. Molecular structure of bottlebrush polymers in melts. *Science advances*, 2(11):e1601478, 2016.

[109] Fabian Pedregosa, Gaël Varoquaux, Alexandre Gramfort, Vincent Michel, Bertrand Thirion, Olivier Grisel, Mathieu Blondel, Peter Prettenhofer, Ron Weiss, Vincent Dubourg, Jake Vanderplas, Alexandre Passos, David Cournapeau, Matthieu Brucher, Matthieu Perrot, and Edouard Duchesnay. Scikit-learn: Machine learning in python. *Journal of machine learning research*, 12(Oct):2825–2830, 2011.

[110] Stacy L Pesek, Yen-Hao Lin, Hui Zhen Mah, Will Kasper, Bo Chen, Brian J Rohde, Megan L Robertson, Gila E Stein, and Rafael Verduzco. Synthesis of bottlebrush copolymers based on poly (dimethylsiloxane) for surface active additives. *Polymer*, 98:495–504, 2016.

[111] Darin Q Pike, François A Detcheverry, Marcus Müller, and Juan J de Pablo. Theoretically informed coarse grain simulations of polymeric systems. *The Journal of chemical physics*, 131(8):084903, 2009.

[112] Darin Q. Pike, Marcus Müller, and Juan J. de Pablo. Monte-carlo simulation of ternary blends of block copolymers and homopolymers. *The Journal of Chemical Physics*, 135(11):114904, 2011.

[113] TJ Prosa, MJ Winokur, Jeff Moulton, Paul Smith, and AJ Heeger. X-ray structural studies of poly (3-alkylthiophenes): an example of an inverse comb. *Macromolecules*, 25(17):4364–4372, 1992.

[114] Abelardo Ramírez-Hernández, Su-Mi Hur, Julio C Armas-Pérez, Monica Olvera de la Cruz, and Juan J de Pablo. Demixing by a nematic mean field: Coarse-grained simulations of liquid crystalline polymers. *Polymers*, 9(3):88, 2017.

[115] T. Rowan. *Functional Stability Analysis of Numerical Algorithms*. PhD thesis, University of Texas at Austin, 1990.

[116] Anandi Roy, Thomas L Bougher, Rugang Geng, Yutian Ke, Jason Locklin, and Baratunde A Cola. Thermal conductance of poly (3-methylthiophene) brushes. *ACS applied materials & interfaces*, 8(38):25578–25585, 2016.

[117] Victor Rühle, Christoph Junghans, Alexander Lukyanov, Kurt Kremer, and Denis Andrienko. Versatile object-oriented toolkit for coarse-graining applications. *Journal of Chemical Theory and Computation*, 5(12):3211–3223, 2009.

[118] Brett M Savoie, Kevin L Kohlstedt, Nicholas E Jackson, Lin X Chen, Monica Olvera De La Cruz, George C Schatz, Tobin J Marks, and Mark A Ratner. Mesoscale molecular network formation in amorphous organic materials. *Proceedings of the National Academy of Sciences*, 111(28):10055–10060, 2014.

[119] Christoph Scherer and Denis Andrienko. Comparison of systematic coarse-graining strategies for soluble conjugated polymers. *The European Physical Journal Special Topics*, 225(8-9):1441–1461, 2016.

[120] Andrew J Schultz, Carol K Hall, and Jan Genzer. Obtaining concentration profiles from computer simulation structure factors. *Macromolecules*, 40(8):2629–2632, 2007.

[121] Kadhiravan Shanmuganathan, Jeffrey R Capadona, Stuart J Rowan, and Christoph Weder. Stimuli-responsive mechanically adaptive polymer nanocomposites. *ACS applied materials & interfaces*, 2(1):165–174, 2009.

[122] M Scott Shell. The relative entropy is fundamental to multiscale and inverse thermodynamic problems. *The Journal of chemical physics*, 129(14):144108, 2008.

[123] Jörn Ilja Siepmann and Daan Frenkel. Configurational bias monte carlo: a new sampling scheme for flexible chains. *Molecular Physics*, 75(1):59–70, 1992.

[124] Mutasem Omar Sinnokrot and C David Sherrill. Highly accurate coupled cluster potential energy curves for the benzene dimer: sandwich, t-shaped, and parallel-displaced configurations. *The Journal of Physical Chemistry A*, 108(46):10200–10207, 2004.

[125] Thomas J Sisto, Yu Zhong, Boyuan Zhang, M Tuan Trinh, Kiyoshi Miyata, Xinjue Zhong, X-Y Zhu, Michael L Steigerwald, Fay Ng, and Colin Nuckolls. Long, atomically precise donor–acceptor cove-edge nanoribbons as electron acceptors. *Journal of the American Chemical Society*, 139(16):5648–5651, 2017.

[126] Andrew J Spakowitz and Zhen-Gang Wang. End-to-end distance vector distribution with fixed end orientations for the wormlike chain model. *Physical Review E*, 72(4):041802, 2005.

[127] Semjon Stepanow and Gunter M Schütz. The distribution function of a semiflexible polymer and random walks with constraints. *EPL (Europhysics Letters)*, 60(4):546, 2002.

[128] AJ Stone. The description of bimolecular potentials, forces and torques: the s and v function expansions. *Molecular Physics*, 36(1):241–256, 1978.

[129] Martien A Cohen Stuart, Wilhelm TS Huck, Jan Genzer, Marcus Müller, Christopher Ober, Manfred Stamm, Gleb B Sukhorukov, Igal Szleifer, Vladimir V Tsukruk, Marek Urban, Francois Winnik, Stefan Zauscher, Igor Luzinov, and Sergiy Minko. Emerging applications of stimuli-responsive polymer materials. *Nature materials*, 9(2):101, 2010.

[130] Daniel F Sunday, Alice B Chang, Christopher D Liman, Eliot Gann, Dean M Delongchamp, Lars Thomsen, Mark W Matsen, Robert H Grubbs, and Christopher L Soles. Self-assembly of abc bottlebrush triblock terpolymers with evidence for looped backbone conformations. *Macromolecules*, 2018.

[131] Juntao Tang, Jared Sisler, Nathan Grishkewich, and Kam Chiu Tam. Functionalization of cellulose nanocrystals for advanced applications. *Journal of colloid and interface science*, 494:397–409, 2017.

[132] K Tashiro, K Ono, Y Minagawa, K Kobayashi, T Kawai, and K Yoshino. Structural changes in the thermochromic solid-state phase transition of poly (3-alkylthiophene. *Synthetic Metals*, 41(1-2):571–574, 1991.

[133] Kohji Tashiro, Keiko Ono, Yasuhisa Minagawa, Masamichi Kobayashi, Tsuyoshi Kawai, and Katsumi Yoshino. Structure and thermochromic solid-state phase transition of poly (3-alkylthiophene). *Journal of Polymer Science Part B: Polymer Physics*, 29(10):1223–1233, 1991.

[134] Karl J. Thorley and Chad Risko. Mapping the configuration dependence of electronic coupling in organic semiconductors. *Journal of Materials Chemistry C*, 4:3825–3832, 2016.

[135] Andreas F Tillack, Lewis E Johnson, Bruce E Eichinger, and Bruce H Robinson. Systematic generation of anisotropic coarse-grained lennard-jones potentials and their application to ordered soft matter. *Journal of chemical theory and computation*, 12(9):4362–4374, 2016.

[136] Thorsten Vehoff, Bjorn Baumeier, Alessandro Troisi, and Denis Andrienko. Charge transport in organic crystals: role of disorder and topological connectivity. *Journal of the American Chemical Society*, 132(33):11702–11708, 2010.

[137] Ian A VonWald, Mark Martin Moog, Travis William LaJoie, Joshua David Yablonski, Dean M DeLongchamp, Jason Locklin, Frank Tsui, and Wei You. Morphology, structure, and enhanced intramolecular conduction in ultralong conjugated polymer brushes. *The Journal of Physical Chemistry C*, 2018.

[138] Jiafang Wang and Marcus Muller. Microphase separation of diblock copolymer brushes in selective solvents: Single-chain-in-mean-field simulations and integral geometry analysis. *Macromolecules*, 42(6):2251–2264, 2009.

[139] Jiafang Wang and Marcus Muller. Microphase separation of mixed polymer brushes: dependence of the morphology on grafting density, composition, chain-length asymmetry, solvent quality, and selectivity. *The Journal of Physical Chemistry B*, 113(33):11384–11402, 2009.

[140] Qiang Wang. Effects of interaction range and compressibility on the microphase separation of diblock copolymers: Mean-field analysis. *The Journal of chemical physics*, 129(5):054904, 2008.

[141] Amanda E Way, Lorraine Hsu, Kadhiravan Shanmuganathan, Christoph Weder, and Stuart J Rowan. ph-responsive cellulose nanocrystal gels and nanocomposites. *ACS Macro Letters*, 1(8):1001–1006, 2012.

[142] Stephen Whitelam and Phillip L Geissler. Avoiding unphysical kinetic traps in monte carlo simulations of strongly attractive particles. *The Journal of chemical physics*, 127(15):154101, 2007.

[143] Monika Williams, Naga Rajesh Tummala, Saadullah G Aziz, Chad Risko, and Jean-Luc Brédas. Influence of molecular shape on solid-state packing in disordered pc61bm and pc71bm fullerenes. *The journal of physical chemistry letters*, 5(19):3427–3433, 2014.

[144] Mark R Wilson. Molecular dynamics simulations of flexible liquid crystal molecules using a gay-berne/lennard-jones model. *The Journal of chemical physics*, 107(20):8654–8663, 1997.

[145] Jay R. Winkler and Harry B. Gray. Electron flow through metalloproteins. *Chemical Reviews*, 114(7):3369–3380, 2014.

[146] Qinghe Wu, Donglin Zhao, Jinghui Yang, Valerii Sharapov, Zhengxu Cai, Lianwei Li, Na Zhang, Andriy Neshchadin, Wei Chen, and Luping Yu. Propeller-shaped acceptors for high-performance non-fullerene solar cells: Importance of the rigidity of molecular geometry. *Chemistry of Materials*, 29(3):1127–1133, 2017.

[147] Tao Wu, Kirill Efimenko, Petr Vlcek, Vladimír Šubr, and Jan Genzer. Formation and properties of anchored polymers with a gradual variation of grafting densities on flat substrates. *Macromolecules*, 36(7):2448–2453, 2003.

[148] Yan Xia, Bradley D Olsen, Julia A Kornfield, and Robert H Grubbs. Efficient synthesis of narrowly dispersed brush copolymers and study of their assemblies: the importance of side chain arrangement. *Journal of the American Chemical Society*, 131(51):18525–18532, 2009.

[149] Chang Xu, Tao Wu, Charles Michael Drain, James D Batteas, Michael J Fasolka, and Kathryn L Beers. Effect of block length on solvent response of block copolymer brushes: Combinatorial study with block copolymer brush gradients. *Macromolecules*, 39(9):3359–3364, 2006.

[150] Sophia N Yaliraki and Robert J Silbey. Conformational disorder of conjugated polymers: Implications for optical properties. *The Journal of chemical physics*, 104(4):1245–1253, 1996.

[151] Shinpei Yamamoto, Muhammad Ejaz, Yoshinobu Tsujii, and Takeshi Fukuda. Surface interaction forces of well-defined, high-density polymer brushes studied by atomic force microscopy. 2. effect of graft density. *Macromolecules*, 33(15):5608–5612, 2000.

[152] Jie Yi, Qunxing Xu, Xuefei Zhang, and Hailiang Zhang. Chiral-nematic self-ordering of rodlike cellulose nanocrystals grafted with poly (styrene) in both thermotropic and lyotropic states. *Polymer*, 49(20):4406–4412, 2008.

[153] Joseph X Zheng, Huiming Xiong, William Y Chen, Kyungmin Lee, Ryan M Van Horn, Roderic P Quirk, Bernard Lotz, Edwin L Thomas, An-Chang Shi, and Stephen ZD Cheng. Onsets of tethered chain overcrowding and highly stretched brush regime via crystalline- amorphous diblock copolymers. *Macromolecules*, 39(2):641–650, 2006.

[154] Yu Zhong, Thomas J Sisto, Boyuan Zhang, Kiyoshi Miyata, X-Y Zhu, Michael L Steigerwald, Fay Ng, and Colin Nuckolls. Helical nanoribbons for ultra-narrowband photodetectors. *Journal of the American Chemical Society*, 139(16):5644–5647, 2017.

[155] Yu Zhong, M Tuan Trinh, Rongsheng Chen, Geoffrey E Purdum, Petr P Khlyabich, Melda Sezen, Seokjoon Oh, Haiming Zhu, Brandon Fowler, Boyuan Zhang, Wei Wang, Chang-Yong Nam, Matthew Y Sfeir, Charles T Black, Michael L Steigerwald, Yueh-Lin Loo, Fay Ng, X-Y Zhu, and Colin Nuckolls. Molecular helices as electron acceptors in high-performance bulk heterojunction solar cells. *Nature communications*, 6:8242, 2015.

[156] Yu Zhong, M Tuan Trinh, Rongsheng Chen, Wei Wang, Petr P Khlyabich, Bharat Kumar, Qizhi Xu, Chang-Yong Nam, Matthew Y Sfeir, Charles Black, Michael L Steigerwald, Yueh-Lin Loo, Shengxiong Xiao, Fay Ng, X-Y Zhu, and Colin Nuckolls. Efficient organic solar cells with helical perylene diimide electron acceptors. *Journal of the American Chemical Society*, 136(43):15215–15221, 2014.